Hot-carrier extraction in nanowires

Fast, Jonatan

2022

Document Version:
Publisher's PDF, also known as Version of record

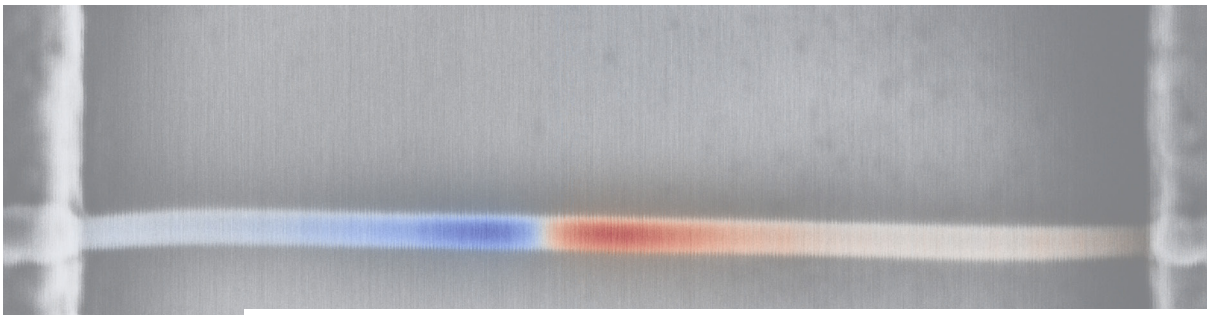

Hot-carrier extraction in nanowires

JONATAN FAST
DEPARTMENT OF PHYSICS | FACULTY OF ENGINEERING | LUND UNIVERSITY

Hot-carrier extraction in nanowires

Hot-carrier extraction in nanowires

by Jonatan Fast

LUND
UNIVERSITY

DOCTORAL THESIS
To be publicly defended, with the permission of the Faculty of Engineering, Lund University, on Friday the 20th of January 2023, 13:15 in the Rydberg lecture hall (Rydbergsalen) at the Department of Physics

Thesis advisors
Professor Heiner Linke, Associate Professor Adam Burke

Faculty opponent
Professor Gregor Koblmüller
Technical University Munich, Germany

Organization
LUND UNIVERSITY

Department of Physics
Box 118
SE–221 00 LUND
Sweden

Document name
DOCTORAL DISSERTATION

Date of disputation
2023-01-20

Sponsoring organization

Author(s)
Jonatan Fast

Title and subtitle
Hot-carrier extraction in nanowires

Abstract
A hot-carrier solar cell aims to generate power from energetic, photoexcited, charge carriers, so called hot carriers, in order to reach higher conversion efficiencies than current solar cell technology. Creating a hot-carrier solar cell has proven challenging for two main reasons: hot carriers lose their energy very quickly, and they need to be extracted over distances of a few hundred nanometers via energy selective filters. Semiconducting III-V nanowires offer high flexibility and control in heterostructure growth, enabling the realisation of numerous types of energy filters, in combination with promising properties such as reduced thermal conductivity, increased hot-carrier temperatures, and various possibilities to tune optical absorption.

This thesis aims to expand current knowledge of how to optimally design devices for hot-carrier extraction in practice. Specifically, three experimental papers (I-III) study the generation of electrical power by extracting charge carriers across energy selective filters within single semiconducting nanowires. The fourth paper (IV) reviews current literature relating to hot carriers in nanowires. The experiments are based on InAs nanowires with epitaxially defined heterostructures of InP or $InAs_xP_{1-x}$ that form energy filters. Charge carrier extraction is studied by three different means: excitation of a non-equilibrium distribution by optical or electron-beam exposure, or the generation of an equilibrium distribution by heat.

In Papers I and II, hot-carrier extraction is spatially resolved over a rectangular InP barrier. Paper I uses the high spatial resolution of an electron beam, while Paper II studies the operation of a similar devices under highly focused optical excitation. Both papers observe hot-carrier extraction around the barrier. The mechanism for extraction is better understood and valuable input for the future design of hot-carrier photovoltaic devices is extracted, such as hot-electron diffusion lengths on the order of a few hundred nanometers.

Paper III studies thermoelectric power generation in a nonlinear transport regime of a ramp-shaped potential barrier, realised by gradually changing x in $InAs_xP_{1-x}$. It is observed that fill factor, and thus maximum output power, can be tuned beyond the linear response limits. This opens up a new door of possibility for tuning the performance of both thermoelectric and hot-carrier photovoltaic systems.

Key words
nanowire, hot carrier, photovoltaic, thermoelectric

Classification system and/or index terms (if any)

Supplementary bibliographical information

Language
English

ISSN and key title

ISBN
978-91-8039-500-7 (print)
978-91-8039-501-4 (pdf)

Recipient's notes

Number of pages
177

Price

Security classification

Signature 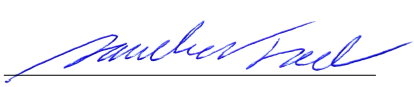

Date 2022-12-20

Hot-carrier extraction in nanowires

by Jonatan Fast

LUND
UNIVERSITY

Division of Solid State Physics
Department of Physics
Faculty of Engineering
Lund University

Cover illustration front: Optical beam induced current measurement of a single nanowire, red and blue regions indicate hot-carrier extraction in opposite driections. Experimental details are given in paper III.

Cover illustration back: In case you cannot understand anything in this thesis, if you think it contains no novelty, or really if you struggle in any way...

Faculty of Engineering, Department of Physics
Lund University, Lund, Sweden

ISBN: 978-91-8039-500-7 (print)
ISBN: 978-91-8039-501-4 (pdf)

Printed in Sweden by Media-Tryck, Lund University, Lund 2022

Media-Tryck is a Nordic Swan Ecolabel certified provider of printed material. Read more about our environmental work at www.mediatryck.lu.se

MADE IN SWEDEN

The story so far:
In the beginning the Universe was created.
This has made a lot of people very angry
and been widely regarded as a bad move.

— Douglas Adams, The Restaurant at the End of the Universe

Devoted to my mother and father.

Contents

List of publications

This thesis is based on the following publications, referred to in Roman numerals:

I **Hot-carrier Separation in Heterostructure Nanowires Observed by Electron-Beam Induced Current**
Jonatan Fast, Enrique Barrigon, Mukesh Kumar, Yang Chen, Lars Samuelson, Magnus Borgström, Anders Gustafsson, Steven Limpert, Adam M. Burke, Heiner Linke
Nanotechnology **31** (2020) 394004
I fabricated the experimental devices, performed the experiment together with E. Barrigon, analyzed the data, carried out theoretical calculations with help from Y. Chen, and wrote all sections of the paper with help from co-authors.

II **Optical-Beam-Induced Current in InAs/InP Nanowires for Hot-Carrier Photovoltaics**
Jonatan Fast*, Yen-Po Liu*, Yang Chen, Lars Samuelson, Adam M. Burke, Heiner Linke, Anders Mikkelsen
ACS Applied Energy Materials **5** (2022) 7728-7734
I fabricated the experimental devices, assisted Y-P. Liu in performing the experiment, analyzed the data, carried out theoretical calculations with help from Y. Chen. I wrote all the sections of the paper with help from co-authors.
*authors contributed equally to this work

III **Thermoelectric, Nonlinear Performance of an Asymmetric Energy Barrier**
Jonatan Fast, Hanna Lundström, Sven Dorsch, Lars Samuelson, Adam M. Burke, Peter Samuelsson, Heiner Linke
In manuscript
Sample fabrication and experiment was done by H. Lundström under my supervision and contribution. I analyzed the data with help from H. Lundström, contributed to theoretical calculations by P. Samuelsson. I wrote all the sections of the paper with help from co-authors.

IV **Hot-Carrier Optoelectronic Devices Based on Semiconductor Nanowires**
Jonatan Fast, Urs Aeberhard, Stephen P. Bremner, Heiner Linke
Applied Physics Reviews **8** (2021) 021309
I carried out the literature study, made the figures, planned, coordinated, and did a majority of the writing with contributions from all authors. Theoretical calculations were done by U. Aeberhard

Abstract

A hot-carrier solar cell aims to generate power from energetic, photoexcited, charge carriers, so called hot carriers, in order to reach higher conversion efficiencies than current solar cell technology. Creating a hot-carrier solar cell has proven challenging for two main reasons: hot carriers lose their energy very quickly, and they need to be extracted over distances of a few hundred nanometers via energy selective filters. Semiconducting III-V nanowires offer high flexibility and control in heterostructure growth, enabling the realisation of numerous types of energy filters, in combination with promising properties such as reduced thermal conductivity, increased hot-carrier temperatures, and various possibilities to tune optical absorption.

This thesis aims to expand current knowledge of how to optimally design devices for hot-carrier extraction in practice. Specifically, three experimental papers (I-III) study the generation of electrical power by extracting charge carriers across energy selective filters within single semiconducting nanowires. The fourth paper (IV) reviews current literature relating to hot carriers in nanowires. The experiments are based on InAs nanowires with epitaxially defined heterostructures of InP or $InAs_xP_{1-x}$ that form energy filters. Charge carrier extraction is studied by three different means: excitation of a non-equilibrium distribution by optical or electron-beam exposure, or the generation of an equilibrium distribution by heat.

In Papers I and II, hot-carrier extraction is spatially resolved over a rectangular InP barrier. Paper I uses the high spatial resolution of an electron beam, while Paper II studies the operation of a similar devices under highly focused optical excitation. Both papers observe hot-carrier extraction around the barrier. The mechanism for extraction is better understood and valuable input for the future design of hot-carrier photovoltaic devices is extracted, such as hot-electron diffusion lengths on the order of a few hundred nanometers.

Paper III studies thermoelectric power generation in a nonlinear transport regime of a ramp-shaped potential barrier, realised by gradually changing x in $InAs_xP_{1-x}$. It is observed that fill factor, and thus maximum output power, can be tuned beyond the linear response limits. This opens up a new door of possibility for tuning the performance of both thermoelectric and hot-carrier photovoltaic systems.

Popular science summary

How do we ensure reliable and predictable energy production that can last for all foreseeable future? In contrast to gas, coal, or nuclear power, which rely on limited natural resources, a renewable energy source is one that, per definition, does not consume finite resources. However, even renewable energy sources are limited in the amount of electricity they can generate. Sunlight is, in fact, the only energy source that on its own contains enough energy to support the demands of the whole planet. It is therefore of great interest to have efficient and cheap ways to convert solar energy into electricity.

Solar cells convert sunlight into electricity using electronic materials known as semiconductors and the so-called photovoltaic effect. A solar cell requires no moving parts, in contrast to most methods of generating electricity that rely on the movements of electromagnets in an electrical generator (such as wind, hydro, and nuclear power). Via the photovoltaic effect, electrons absorb energy directly from the sunlight. The energy causes the electrons to move through an electrical circuit. The flow of electrons leads to a current, and in this way current is generated from sunlight! Since their invention in the 1950s, solar cells have significantly improved in performance and gotten much cheaper, but they are still operating along the exact same principle. Unfortunately, this principle comes with a severe limitation on how efficiently these

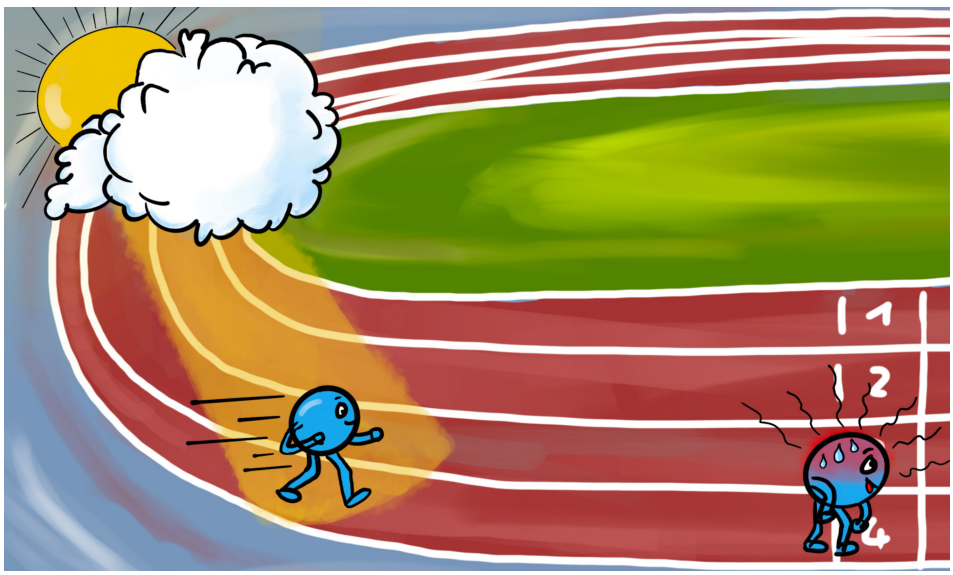

Figure 1: An electron sprinter gets energy from the sun, but is bad at conserving it. The artistic interpretations in this section were generously provided by Dr. Sven Dorsch.

can convert energy, a limitation which the work of this thesis addresses.

To help us grasp the problem, we can imagine the electrons that make up the electrical current as running athletes. When the electrons absorb light, they gain a boost in energy, and start to run very fast. This means that an electrical current is flowing. Unfortunately, the electrons are short-distance runners, and not very good at conserving their energy. They very quickly exhaust and overheat themselves, losing a large part of the energy they absorbed as heat. This severely limits the amount of current that can be produced, and since solar cells made today do not address this energy loss, even the most perfectly made device can still not convert more than about a third of the energy contained in the sunlight into electricity.

So, how can this limitation be addressed? The fundamental idea is to make use of the energy contained in these energetic electrons before they have time to lose it as heat. This idea has been around almost as long as solar cells have existed, but, in practice, it has proven very challenging. As of today, a solar cell operating along these principles does not exist.

The challenge can be broken down into two parts. For one part, researchers are trying to think of clever ways to make the electrons better at conserving their energy. Although this is part of the solution, it is not in the nature of electrons to be conservative, and there is only so much you can do about this. This leaves us with the challenge of catching and using their energy very quickly, before they complete their short energetic sprint. Here, we are talking of sprint distances of roughly 100 nanometers, 1000 times shorter than the width of a hair.

In this thesis, I address this problem by creating tiny race tracks for energetic electrons where they have to use their energy to overcome obstacles. When an obstacle is too large for a single electron to overcome, it can sacrifice some of its energy in order

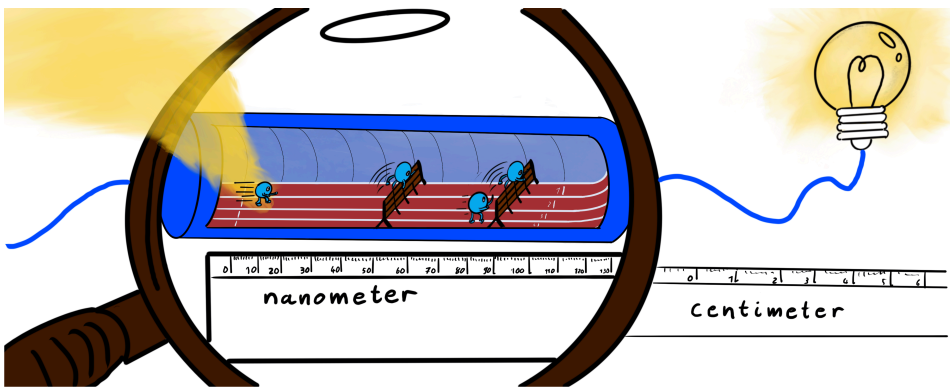

Figure 2: A 100 nanometer obstacle race for electron sprinters generates a current.

to help another one come over. While overcoming the obstacles, their energy can be turned into electricity instead of heat. The unique aspect of my research is that I build these race tracks using structures referred to as nanowires: long, thin semiconductor structures with a diameter smaller than 100 nanometers. In these nanowires, obstacles for the electrons can be created by manipulating the atomic composition of the nanowire.

In this work, I apply various methods to provide the electrons with energy to make them sprint. I then study the current generated as they run along the track and overcome the obstacles. Thus, I address relevant questions, such as how far they can run, if they still have enough energy to overcome the obstacles, or how the shape of the obstacles affect their ability to overcome them.

The energetic electrons are referred to, by researchers, as hot carriers, because they contain so much energy. The information from this thesis will be valuable to the future development of hot-carrier solar cells, so that we can maximise the energy converted from sunligt into electricity.

Populärvetenskaplig sammanfattning

Att säkerställa en tillförlitlig och förutsägbar energiproduktion som kan räcka under den överskådliga framtiden är en utmaning kanske mer aktuell idag än någonsin. Till skillnad från gas, kol eller kärnkraft, som är beroende av begränsade naturresurser, är en förnybar energikälla en som per definition inte förbrukar ändliga resurser. Även förnybara energikällor är dock begränsade i den mängd el som de kan generera. Solljus är faktiskt den enda energikälla som för sig själv innehåller tillräckligt med energi för att tillgodose hela planetens behov (med stor marginal). Det är därför av stort intresse att utveckla effektiva och billiga sätt att omvandla solenergi till elektricitet.

Solceller omvandlar solljus till elektricitet med hjälp av elektroniska material, så kallade halvledare, och den fotovoltaiska effekten. En solcell kräver inga rörliga delar, till skillnad från de flesta metoder för att generera en elektrisk ström som bygger på rörelse av elektromagneter i en generator (såsom vind-, vatten-, och kärnkraft). Genom den fotovoltaiska effekten absorberar elektronerna i halvledaren energi direkt från solljuset. Energin driver elektronerna genom en elektrisk krets. Flödet av elektroner bildar en elektrisk ström, och på så vis genereras elektricitet från solljus. Sedan solceller uppfanns på 1950-talet har de förbättrats avsevärt i prestanda och blivit mycket billigare, men de fungerar fortfarande enligt exakt samma princip. Tyvärr har denna princip en stor begränsning i hur effektivt energi kan omvandlas från solljust till elektricitet.

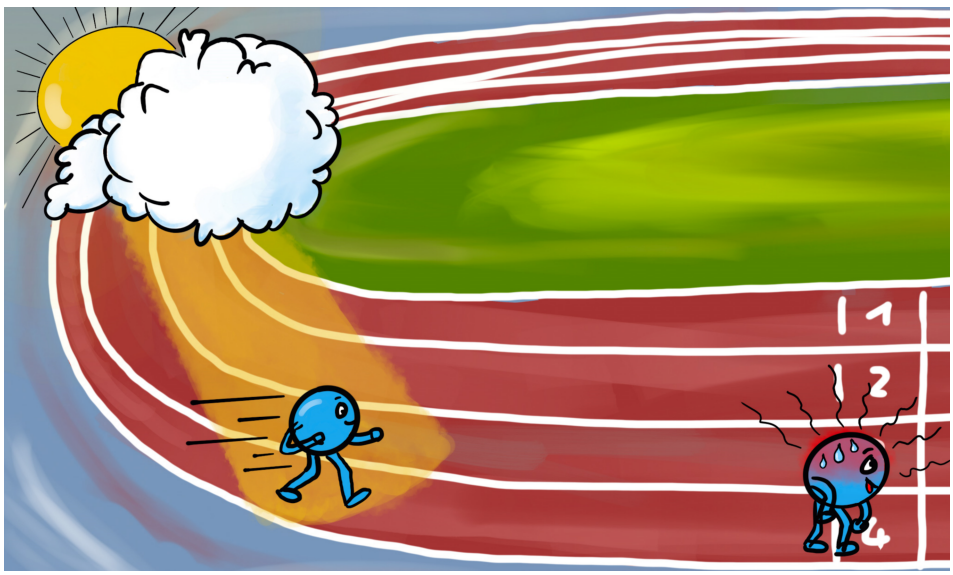

Figur 3: En elektronlöpare får energi av solen men är dålig på att spara den. De konstnärliga tolkningarna i denna del har skänkts av den generöse Dr. Sven Dorsch.

Arbetet i denna avhandling handlar om hur denna begränsning ska kunna undvikas.

För att hjälpa oss att förstå problemet kan vi föreställa oss elektronerna som utgör den elektriska strömmen som löpare. När elektronerna absorberar ljus får de en energikick och börjar springa mycket snabbt. Detta innebär att strömmen ökar. Tyvärr är elektronerna kortdistanslöpare och inte särskilt bra på att spara sin energi. De blir mycket snabbt utmattade, överhettade och förlorar en stor del av den energi de absorberat genom att generera värme. Detta begränsar kraftigt mängden ström som kan produceras. Eftersom solceller som tillverkas idag inte tar hänsyn till denna energiförlust, kan inte ens den mest optimerade solcellen omvandla mer än ungefär en tredjedel av den energi som finns i solljuset till elektricitet.

Hur kan man då åtgärda denna begränsning? Den grundläggande idén är att utnyttja den energi som finns i de energirika elektronerna innan de hinner förlora den som värme. Denna idé har funnits nästan lika länge som solceller har funnits, men det har visat sig vara mycket svårt att uppnå i praktiken. Än i dag finns det ingen fullt fungerande solcell som har lyckats med det.

Utmaningen kan delas upp i två delar. Å ena sidan försöker forskare komma på smarta sätt att göra elektronerna bättre på att bevara sin energi. Även om detta är en del av lösningen ligger det inte i elektronernas natur att vara återhållsamma, och det verkar inte finnas så mycket vi kan göra åt detta. Detta lämnar oss med utmaningen att fånga upp och använda deras energi mycket snabbt. Energin måste användas innan elektronerna springer färdigt sitt korta sprintlopp, och då vi talar om sprintsträckor på ungefär 100 nanometer, 1000 gånger kortare än bredden på ett hårstrå.

I den här avhandlingen tar jag itu med detta problem genom att skapa små tävlingsbanor för energirika elektroner där de måste använda sin energi för att övervinna hinder. När ett hinder är för stort för en enskild elektron att övervinna kan den offra en del av

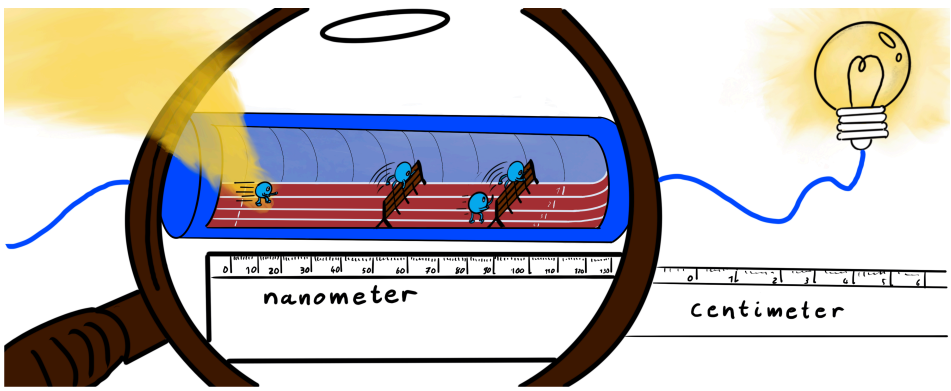

Figur 4: En 100-nanometers häcklöpningsbana för elektronlöpare genererar en ström.

sin energi för att hjälpa en annan elektron att komma över. När de övervinner hindren kan deras energi omvandlas till elektricitet i stället för värme. Den unika aspekten av min forskning är att jag bygger dessa tävlingsbanor med hjälp av strukturer som kallas nanotrådar: långa, tunna halvledarstrukturer med en diameter som är mindre än 100 nanometer. I dessa nanotrådar kan man skapa hinder för elektronerna genom att manipulera nanotrådens atomära sammansättning.

I mitt arbete tillämpar jag olika metoder för att förse elektronerna med energi, till exempel från ljus och från värme. Jag studerar sedan den ström som genereras när de tar sig igenom hinderbanan. På så vis undersöker jag frågor såsom hur långt de kan springa, om de fortfarande har tillräckligt med energi för att övervinna hindren, och hur formen på hindren påverkar deras förmåga att övervinna dem.

Forskare kallar de energirika elektronerna för heta bärare, på engelska hot carriers, eftersom de innehåller så mycket energi. Informationen i denna avhandling kommer att vara värdefull i den fortsatta utvecklingen av solceller som utnyttjar heta bärare, så att vi i framtiden kan maximera energiutviningen från solljus.

Acknowledgements

Never have I in my life been so aware of how little I know. Never have I been more sure of how important the people that surround me are. None of this would exist without the support from a great number of people.

My supervisor, Heiner Linke, thank you for taking me in, putting your trust in me, challenging me, and giving me room to grow. I especially admire your ability to always get to the core of a problem, is a skill I will try to replicate for the rest of my career. Thank you also for all the cool places around the world you have sent me to!

My co-supervisor, Adam M. Burke, having you around has been invaluable to this work. From your high expertise in the labs to your approachable way. Thank you for all the good wine throughout the years, and more to come!

A big thank you to the people in the transport group throghout the years. Artis Svilans, I-Ju Chen, Steven Limpert, Yang Chen, Hanna Lundström, and Sven Dorsch. My work is standing on your shoulders.

I have had the luxury to collaborate with many professional and friendly people throughout the years. Enrique Barrigon, Yen-Po Liu, Anders Mikkelsen, Mukesh Kumar, Lars Samuelson, Anders Gustafsson, Peter Samuelsson, Daniel Madsen thank you for all your contributions! A special thank you to Stephen P. Bremner and Urs Aeberhard, working on our review was one of the highlights of my PhD.

None of the work here would be possible without the talented and helpful technical and administrative staff at the division, the NanoLab, and within NanoLund. Thank you for everything you do! A special thank you also to Carina Fasth for always taking time for my fundamental physics questions, and ”reteaching” me solid state physics.

More than anything what has made this time special for me is the wonderful people I have gotten to know. The atmosphere at the division is really something quite special, and it has felt like my second home. The borders of research groups are blurred and collaborations are encouraged in all directions. Everyday I am blessed with friendly and intriguing encounters at the lunch tables, during fika, running through the corridors, and even outside of work. A special thank you to our friendly head of division, Dan Hessman, for making me feel I will be accepted no matter who I am.

There are so many people that brighten my day at the division that I will not be able to list everyone, but let’s give it a try: Alexander, Anastasiia Anette, Anders K, Anneli, Antti, Asmita, Bao, Bengt, Calle, Claes Damiano, David, Elke, Esra, Florinda, Frida, Gerda, Harald, Hossein, Ivan M, Ivan U, Jason, Johanna, Kristi, Kushagr, Luke, Maria, Mariia, Markus S, Markus T, Matteo, Max, Mirja, Mohammad, Mokhtar,

Namsoon, Neimantas, Patrik, Pau, Rong Sun, Roman, Ruben, Ruby, Sara, Sebastian, Simon, Sudhar, Thanos, Therese... All right this can go on forever, if you feel we have had a moment but you are not on the list, we have! Thank you Batman (aka Linnéa) for letting me be your sidekick, it has been a pleasure. Thank you Julia for being such an amazing office mate during my last time here, I only wish you had moved in sooner.

An extra warm thank you to the people in the extended H (all the way to B) corridor: Lukas, David, Oskar, Irene, Sven. Whenever I had a bad day it was always brightened by having you around, it has been a real treat being with you from the beginning to the end.

Sven, I am also very grateful for all the professional help you've given me throughout the years in the lab, during scientific discussions, and with your ruler. I seriously think you might be the person who has taught me the most during my PhD. Professional things aside, you have been a great friend, and all of our nonsense in the office has really been helping me stay sane.

I would have struggled to stay focused at work without all the physical and social activities in my free time with my lovely dance friends, all the people I've met climbing (special shout-out to my climbing-bro Martin!), and the people at work who have accompanied me through runs in all sorts of weather (Marie, Stephanie, Linnéa, Markus) and of course at the innebandy-court!

Lastly, none of this would have been possible without the unconditional love I receive from everyone in my family. Having you behind me, I can safely step outside of my comfort zone and take the risk of failing.

1. Introduction

I'd put my money on the sun and solar energy.
What a source of power!
I hope we don't have to wait till oil and
coal run out before we tackle that.
– Thomas Edison

Sunlight is the only energy source, not based on finite resources, that could feasibly produce enough energy to support the consumption of the whole planet [1]. Unfortunately, in the conventional solar cell, converting energy from the sun directly into electricity, a majority of the energy absorbed from the sunlight is lost in the form of heat. If this energy could instead be used to generate electricity, solar cells would be able to produce more power per unit area they cover.

A solar, or photovoltaic, cell operates by the photovoltaic effect, depicted in fig. 1.1: an electron in a semiconductor material absorbs the energy, E, of a photon and uses it to overcome the band gap energy, E_g, after which it can contribute to generate electrical power. Because sunlight contains photons with a broad range (spectra) of energies, it

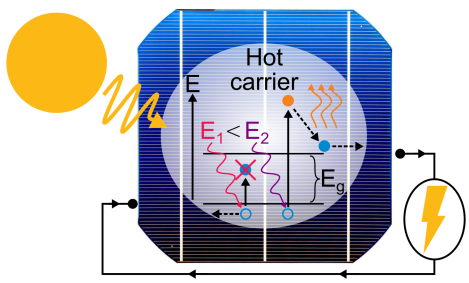

Figure 1.1: In a solar cell, no energy is absorbed when the photon energy is smaller than the band gap. If the energy is larger than the band gap, any excess energy goes to the hot carrier and is subsequently lost as heat. Solar cell adapted from Ref. [2].

is challenging to construct a solar cell able to efficiently convert energy from photons both at the high- and low-energy end of the spectra. At its core, there are two reasons for this: (i) A photon with energy If $E_1 < E_\mathrm{g}$ photon will not be absorbed, and the energy is lost. (ii) A photon with energy If $E_2 > E_\mathrm{g}$, lifts electrons to energies above E_g, so that they contain excess energy $E_2 - E_\mathrm{g}$. This energetic electron is referred to as a *hot carrier*, and it will typically lose its excess energy in the form of heat in a matter of picoseconds (10^{-12} s) [3]. Factor (i) can be addressed by choosing a smaller value for E_g, but that would mean more energy lost as heat via factor (ii). Vice versa, addressing factor (ii) by increasing E_g means more energy lost via factor (i). Ideally, factor (ii) could be addressed in a different way so that E_g can remain small, and both losses minimised.

The concept of such a hot-carrier solar cell, utilising the full energy $E_\mathrm{photon} - E_\mathrm{g}$, has been theoretically described almost as long as solar cells have been around (~ 70 years) [4, 5]. Realising a hot-carrier solar cell in practice, which is still not fully demonstrated as of today, has proven challenging for two main reasons; hot carriers lose their excess energy very quickly, and they need to be extracted over distances of a few hundred nanometers (nm), via energy selective filters that only transmit hot carriers.

The advancement of nanofabrication techniques during the 21st century [6] have ushered in some hope of addressing both of these challenges in practice [7]. Many studies indicate that energy loss rates of hot carriers could be decreased in low-dimensional structures such as quantum wells and quantum dots [8]. At the same time, energy selective filters are easily realised in nanostructures because their synthesis allows for variations in the chemical composition with a high degree of control [9].

A platform that has recently emerged as promising in this context are semiconducting, III-V material, nanowires [10, 11]. Nanowires allow for excellent control and precision in variations of chemical composition [12, 13], control of optical properties [14–17], and reduced rates of hot-carrier energy loss [18–20]. Proof-of-principle hot-carrier photovoltaic devices have been demonstrated in InAs nanowires containing a short segment of InP, however with light-to-electricity conversion efficiencies below 1% [21, 22].

This thesis studies the generation of electrical power by extracting electrons across energy selective filters epitaxially defined within single semiconducting nanowires. The electrons contain energy either in the form of heat or non-equilibrium distributions (hot carriers). Two types of structures are studied: a rectangular, and a ramp-shaped potential barrier. By using three different ways of providing the carriers with energy, a number of questions that all relate to how a hot-carrier photovoltaic device should be optimally designed are addressed.

1.1 Papers

Paper I aims to remove any doubts as to whether a hot-carrier energy filter can be realised within a nanowire, as well as to better understand the mechanism of extraction, and gain input for the improvement of future device design. Previous experiments were unable to pinpoint if observations of hot-carrier extraction in nanowires originated from the introduced heterostructure [21, 22]. Those experiments were done under global illumination of the device. Therefore, other features such as a Schottky-barrier at the semiconductor-metal interface, plasmonic resonance effects, or unintentional variations in crystal quality could be responsible for the observations. By performing electron-beam induced current (EBIC) measurements, hot carriers are excited with a high degree of spatial control. It is observed that the position of excitation within the nanowire has great impact on the current generated. Only when excited roughly within 100 nm of the energy filter, hot-electrons can be extracted and a current generated. This confirms the role of the heterostructure in hot-carrier extraction. Estimated hot-electron diffusion length gives input towards the design of future devices. A beam of energetic electrons does however differ from sunlight as an excitation source. In the end it is necessary to evaluate the performance of these devices under conditions more realistic for the operation of a solar cell.

Consequently, in Paper II we ask ourselves whether a similar level of control in hot-carrier excitation can be attained under optical excitation, and if the same mechanisms still are present? So that the performance of hot-carrier extraction in various nanowire devices can be evaluated and compared under more realistic conditions. The optical beam induced current (OBIC) of similar nanowires as in Paper I are studied by employing a laser beam focused close to the diffraction limit, and a high precision piezomechanic stage to move the sample. Optically induced current generation from hot-carrier extraction is observed to vary with excitation location in a similar way as in Paper I, and optoelectronic performance parameters such as open-circuit voltage, short-circuit current, and power are extracted. It is demonstrated that this can be done while varying the location, energy, and intensity of the optical excitation. Estimates for hot-electron diffusion lengths on the order of 300 nm are extracted. OBIC, with the supporting information from EBIC, is demonstrated as a valuable tool to use in the future evaluation and comparison of candidate systems for hot-carrier photovoltaics.

By using nanoscale energy filters, thermoelectric devices can be operated in regions of nonlinear transport where novel properties such as thermal rectification can be observed [23, 24]. The linear shape of conventional thermoelectric devices limits the maximum power they can generate, as their fill factor is always 0.25. This can be compared to conventional photovoltaic devices, which operate in a nonlinear region,

where the fill factor can approaches 1. Paper III demonstrates how the fill factor, and thus output power, in a thermoelectric system can be tuned by altering the shape of the energy filter operating in a nonlinear region. This is done by thermally and electrically biasing a single nanowire device containing a ramp-shaped potential barrier. The device promotes thermoelectric currents when thermally biased in one direction, and demotes it in the other direction, acting as a thremoelectric rectifier. These result introduce a path towards optimising the performance of any device that generates power by extracting charge carriers across heterostructure-defined energy filters, such as thermoelectrics and hot-carrier photovoltaics.

Paper IV is a review on the current literature relating to hot carriers in nanowires. It highlights the various modifications of hot-carrier dynamics possible due to the quantum confinement and increased boundary scattering in nanowires due to their geometry. It showcases how nanowires have been used to demonstrate power production from charge carriers energised both by heat and optically excited hot carriers. Several questions that still need to be answered in order to fully evaluate the performance that can be achieved in nanowire-based hot-carrier photovoltaic devices.

One question in particular is highlighted in Paper IV, as well as in this thesis: Can nanowires be used to experimentally identify the type of energy filtering design that optimises the performance of a hot-carrier photovoltaic device in terms of both output power and efficiency? Here, the synthesis of nanowires allow for the realisation of many different types fo energy filters. Sesign variations to consider are, for example, variations in barrier shape, filters with serial quantum dots that create box-shaped transmission functions, and designs with two filters that extract hot electrons and holes in opposite directions. Theory, due to the complexity of the system, struggles to consistently describe and predict the effect of such variations on the performance of hot-carrier photovoltaic devices [8]. Instead, it is possible they could be addressed by applying the experimental techniques used in this thesis to compare the performance of the different energy filter designs.

1.2 Outline

Before the Papers, a more thorough introduction to the field and the questions that need to be answered are found. It is structured as follows: Chapter 2 briefly introduces the concepts of electronic band structure, optical excitation, the fundamental challenges to reaching high conversion efficiencies in solar cells, and potential solutions to the problem (so called third-generation photovoltaics). Chapter 3 describes how energy is distributed amongst electrons in a solid in both equilibrium and non-equilibrium situations, the processes by which hot carriers lose their energy, and what

to consider in order to prevent it. Building on this, Chapter 4 starts by evaluating two conventional ways of extracting energy contained in charge carriers, thermoelectrics and photovoltaics. Aspects from both of these approaches are used to describe the design of a hot-carrier photovoltaic device, and various types of energy filters for hot-carrier extraction are compared. Once the reader is familiar with all of these concepts, the nanowire-platform is properly introduced in Chapter 5. Its various benefits for hot-carrier devices are here briefly reviewed based on existing literature, and more extensively in Paper IV. The chapter also describes the specific experimental system studied in this thesis and how it is synthesised. The experimental work of Papers I-III is summarised in Chapter 6. Finally, Chapter 7 presents an outlook identifying experimental systems for future investigation.

2. Background

This chapter introduces basic concepts which the reader needs to be familiar with in order to understand the work presented in this thesis. This includes a brief introduction to the electronic band structure of solids, and the optical excitation processes in a semiconductor. The fundamental limitations to the conversion efficiency of a conventional photovoltaic device are established. Some of the existing ideas for more efficient, so called "third generation", photovoltaic devices are introduced, out of which particular focus is on the hot-carrier approach, and the challenges it entails.

2.1 Electronic band structure

At the core of quantum physics is the strange notion that what we typically call a particle can, in fact, behave both as a wave and as a physical particle. In 1926 Erwin Schrödinger introduced a theory containing the mathematical tools for describing this so called wave-particle duality [25]. In it, any particle is described by a complex wave function

$$\phi(\vec{r}) = e^{i\vec{k}\cdot\vec{r}}, \tag{2.1}$$

where $\vec{r} = (x, y, z)$ is the three-dimensional particle coordinate, and $\vec{k}$ is the wave vector (analogous to its momentum). All information regarding a particles movement and energy in a certain system can be found by solving the Schrödinger equation in the a certain potential landscape, $V(\vec{r})$,

$$\boldsymbol{H}\phi(\vec{r}) = \Big(\underbrace{-\frac{\hbar^2}{2m}\nabla^2}_{E_{\text{kin}}} + \underbrace{V(\vec{r})}_{E_{\text{pot}}} \Big)\phi(\vec{r}) = E\phi(\vec{r}). \tag{2.2}$$

where $\hbar$ is the Planck constant, m is the particle mass, and $\nabla = \left(\frac{\partial}{\partial x}, \frac{\partial}{\partial y}, \frac{\partial}{\partial z}\right)$. Eq. (2.2) is an eigenvalue equation where the Hamiltonian operator, $\boldsymbol{H}$, returns the total energy, E, of a particle described by $\phi(\vec{r})$. The two parts contained in $\boldsymbol{H}$ represent potential energy, E_{pot}, and kinetic energy, E_{kin}.

Solutions to the Schrödinger equation for a free electron is now considered. For a free electron no potential energy is present, so that $V(\vec{r}) = 0$. This leaves us with

$$\nabla^2\phi(\vec{r}) = -\frac{2m_e E}{\hbar^2}\phi(\vec{r}), \tag{2.3}$$

with the solution

$$E = \frac{\hbar^2 k^2}{2m_e}, \tag{2.4}$$

where m_e is the electron mass, and $k = |\vec{k}|$. A typical energy dispersion based on eq. (2.4) is shown in fig. 2.1(a). The free electron is able to take on any energy value along this "free electron parabola". If one replaces k with the classical momentum $p = \hbar k$, we see that we are left with the classical equation for kinetic energy $E_{\text{kin}} = p^2/2m_e$.

In a solid, where electrons are bound to a nuclei, they can only take on certain energy values. The valence electrons, electrons in the outmost shells, are able to jump in between atoms, and can therefore be referred to as nearly-free electrons. To solve which energies they can occupy, the underlying periodic structure of the nuclei building up the crystal lattice needs to be considered. In the nearly free electron model, this is done by assuming that the potential introduced by the nuclei can be completely described by a periodic potential, $V(\vec{r}) = V(\vec{r} + \vec{a})$, where the lattice vector $\vec{a}$ describes the distance between atoms in the crystal lattice. It should be noted that both the free- and the nearly free electron model assume electron-electron interaction is negligible, which simplifies the problem. The corresponding wave function also takes on a periodic form (known as a Bloch wave function [26])

$$\phi(\vec{r}) = e^{i\vec{k}\cdot\vec{r}}u(\vec{r}), \tag{2.5}$$

where $u(\vec{r}) = u(\vec{r} + \vec{a})$.

As a result of solving the Schroedinger equation we get the so called band structure. The band structure indicates which energy states are possible to possess for an electron in a crystal lattice. Fully solving eq. (2.2) for an electron in lattice is complicated by the fact that several periodicities can be identified, in different directions. This means there will be several solutions, for different $\vec{a}$, that all need to be brought together. An example of a full solution is seen for InAs in fig. 2.1(b). Here, W, X, Γ, L, U all indicate different directions of periodicity in k-space. Numerous bands are available, and they cross each other in a complex matter.

The band structure indicated which energy states that can be occupied by an electron. How many states that are available at a certain energy is described by the so called density of states, $Z(E)$. The density of states will depend on the band structure

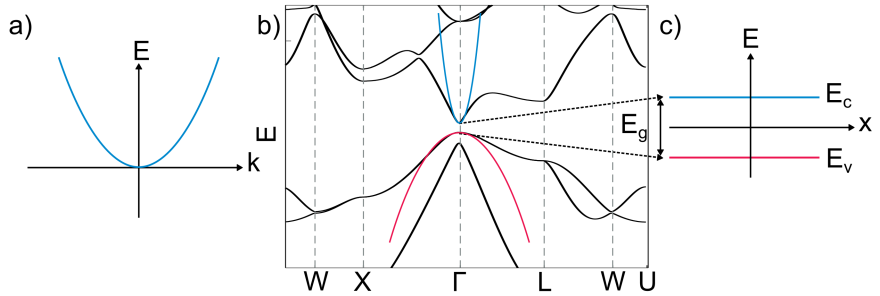

Figure 2.1: Allowed energies as a function k for a) a free electron and b) an electron bound in an InAs crystal. At the band extremes, the diagram can be approximated by a free electron parabola with an altered effective mass, m_e^*. W, X, G, L, U represent various crystal-plane directions in k-space. c) It is common to draw the conduction (valence) band edges, E_c (E_v) as a function of position, highlighting the band gap E_g. Band diagram calculated with Quantum ESPRESSO [27], Matlab script courtesy of P. Hadley [28].

and the dimensionality of the systems, but it can generally be stated that in three dimensions the density of states per unit volume is

$$Z(E) = \frac{4\pi(2m)^{3/2}}{h^3}\sqrt{E}. \tag{2.6}$$

Note that $Z(E)$ only indicate energies which an electron may posses, i.e., available states, not whether an electron is occupying the state. The population (distribution) of electrons across the available states will be discussed in more detail in Ch. (3).

Looking at the band structure in fig. 2.1(b), there is an energy known as the band gap, E_g, within which no allowed energy states exist. The band gap is defined by two band edges, the lower energy is defined by the maximum, E_v, of valence band and the top of E_g is defined by the minimum, E_c, of the conduction band.

A semiconductor material is defined by the fact that at $T = 0$ K (without doping), all bands beneath the conduction band are fully occupied by electrons, while the conduction band and all bands above are fully unoccupied. Most of the unique properties of semiconductor materials are related to the band gap. For example, optical excitation of electrons typically happens around the band gap since it requires an available electron, found abundantly in the valence band, and an empty state at a similar k but higher energy, found abundantly in the conduction band.

The description of the bands can be simplified around points where $\partial E/\partial\vec{k}=0$ using the effective mass approximation. Around these points, the bands can be approximated as free electron parabolas (see fig. 2.1(b)), as in eq. (2.4), if m_e is replaced by the so called effective mass m_e^*. Mathematically, it means that a Taylor expansion can be

done around the band edges to obtain

$$E(k) = E_{\mathrm{i}} + \frac{1}{2}\frac{\partial^2 E}{\partial k^2} = E_{\mathrm{i}} + \frac{\hbar^2 k^2}{2m_{\mathrm{e}}^*}, \tag{2.7}$$

where E_{i} denotes the position of the band edge, e.g. E_{v} and E_{c}. The effective mass is defined as

$$\frac{1}{m_{\mathrm{e}}^*} = \frac{1}{\hbar^2}\frac{\partial^2 E}{\partial k^2}. \tag{2.8}$$

We see that a larger m_{e}^* is the same as a "smoother" parabola. Physically, this means that the electron moving through the solid is disturbed by interactions with electrons and nuclei so that it moves as if it had a different mass. Tabulated values for m_{e}^* are usually given as the ratio $m_{\mathrm{e}}^*/m_{\mathrm{e}}$. The importance of m_{e}^* in the design of a hot-carrier photovoltaic devices is further discussed in section (5.4.1).

It is common to draw a simplified version of the band structure where only the edges of the two bands are considered, as a function of position along a single dimension, as for shown for x-direction in fig. 2.1(c). This way of drawing is very useful since it is simple and most of the physics in a semiconductor happens around E_{v}, E_{g}, and E_{c}.

2.2 Optical excitation

During optical excitation, a photon is absorbed by an electron, using the energy to transition to a higher lying energy band. At the same time, a *hole*, h^+, is left where the electron used to be. We say an electron-hole pair has been generated. The hole is a quasiparticle that indicates an available state to which a neighbouring electron can jump to. Mathematically, however, it can be treated just as if it was an electron with a positive charge. Collectively, electrons and holes are referred to as *charge carriers*, as they both can contribute to electrical current.

During the absorption of a photon there are two laws of conservation that must be followed. The conservation of energy

$$E_{\mathrm{e,f}} = E_{\mathrm{e,i}} + h\nu, \tag{2.9}$$

and the conservation of crystal momentum

$$\vec{k}_{\mathrm{e,f}} = \vec{k}_{\mathrm{e,i}} \pm \vec{k}_{\mathrm{photon}}. \tag{2.10}$$

where $E_{\mathrm{e,i}}$, $E_{\mathrm{e,f}}$, $\vec{k}_{\mathrm{e,i}}$, $\vec{k}_{\mathrm{e,f}}$ are the initial and final energy and crystal momentum of the electron. The incoming photon with frequency ν, and wave vector $\vec{k}_{\mathrm{photon}}$, has the

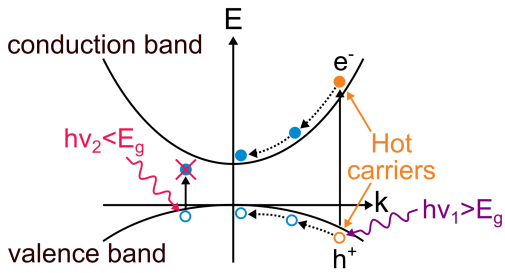

Figure 2.2: Simplified band structure depicting the process of optically exciting a hot carrier.

energy $h\nu$. In most situations, $\vec{k}_{\text{photon}} \ll \vec{k}_{\text{e}}$ such that $\vec{k}_{\text{e,f}} \approx \vec{k}_{\text{e,i}}$. In a band structure picture (fig. 2.2), this means that the electron transitions more or less vertically after absorption. Because of energy conservation, the transition must happen at a $\vec{k}$ where the energy difference between two bands match that of the photon.

When $h\nu > E_{\text{g}}$, $h\nu - E_{\text{g}}$ will be distributed as E_{kin} between the electron and the hole such that the total energy is distributed as

$$\underbrace{h\nu}_{E_{\text{total}}} = \underbrace{E_{\text{g}}}_{E_{\text{pot}}} + \underbrace{E_{\text{kin,e}} + E_{\text{kin,h}}}_{E_{\text{kin}}}. \tag{2.11}$$

The carriers with a non-zero E_{kin} are referred to as *hot carriers*, indicated as orange in fig. 2.2. The difference in shape of the conduction and valence band means that typically $E_{\text{kin,e}} \neq E_{\text{kin,h}}$. In most III-V materials, the conduction band is "sharper", so that $E_{\text{kin,e}} > E_{\text{kin,h}}$ at any specific k.

In a conventional solar cell, all of the E_{kin} is lost, and the portion of E_{total} converted to electrical work can never be larger than E_{pot}. This is because hot carriers lose their excess energy via various forms of inelastic scattering events. These processes (covered in more detail in Ch. (3)), are referred to as *hot-carrier relaxation*, and typically occur on timescales in the range between picoseconds to nanoseconds [3]. The quick relaxation of hot carriers introduces a difficult challenge if one wants to convert the kinetic energy to electrical power.

In an ideal situation, the energy of the hot carriers would not be lost so that 100% of E_{total} could be converted into a photovoltage and used to produce electrical power. One should however always keep in mind that when a researcher uses the wording, "in an ideal situation", this will likely never be the case in reality.

2.3 Energy loss in a photovoltaic device

No matter how well you construct a photovoltaic device, there are some fundamental limitations to how efficiently it can convert the incoming solar energy into electrical power. When speaking of sunlight, it refers to the whole spectrum of photon energies (wavelengths) emitted by the sun. Already in 1961, Shockley and Queisser [29] presented their famous detailed-balance calculations, predicting that at best roughly 30% of the incoming energy in from the spectrum of sunlight can be converted to electrical work. This limit is known in the field of photovoltaics as the *Shockley-Queisser limit*. The remaining $\sim$ 70% of the energy is lost via a variety of mechanisms. These loss mechanism are summarised in fig. 2.3, showing the relative impact of each loss as a function of E_{g}. These calculations, by Hirst and Ekins-Daukes [30], are based on the operational principles of a conventional solar cell (detailed in section (4.1.1)). The two major sources of energy loss that can be identified are:

- *Sub-band gap losses.* A photon with energy $h\nu < E_{\mathrm{g}}$ cannot be absorbed. Thus, such photons in the solar spectrum will not contribute towards generating electrical power, and their energy is lost. To remedy this, the obvious solution is of course to use a semiconductor with a smaller E_{g}, but this comes with a new challenge.
- *Carrier relaxation losses.* The smaller the band gap, the larger part of the absorbed energy turns into E_{kin} of the carriers, in other words more hot carriers are generated. All of this E_{kin} is lost during the hot-carrier relaxation process. The smaller E_{g}, the larger E_{kin}, and the larger the loss via hot-carrier relaxation.

Beside these two, other losses include:

- *Carnot losses.* In any process that can be likened to a heat engine (energy transferred between two reservoirs at different temperatures), the efficiency is bounded above by the Carnot efficiency (see section (4.1.2)). For a solar cell this is set by the temperature of the sun, $T_{\mathrm{sun}} \approx 6000K$, and the temperature of the cell which is roughly at room temperature, $T_{\mathrm{cell}} \approx 300K$. This results in an efficiency limited to $(T_{\mathrm{sun}} - T_{\mathrm{cell}})/T_{\mathrm{sun}} \approx 95\%$.
- *Boltzmann losses.* The incoming photons from the sun arrive more or less as parallel beams, but any light emitted by the solar cell can be spread out over a very large angle. In other words, the emitted light is less ordered than the incoming light, which means it has a higher entropy, and thus energy has been lost.

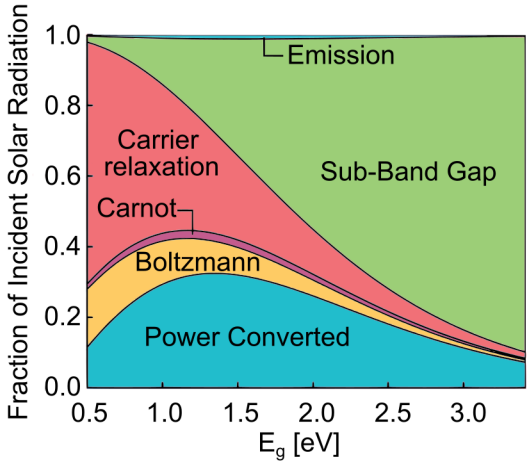

Figure 2.3: The relative distribution between fundamental sources of loss in a conventional, single pn-junction, solar cell, and the energy available for conversion into power. Figure adapted from [30] with permission.

- *Emission losses.* After an electron-hole pair has been excited, they will eventually recombine. This means that the electron falls back from the conduction band to an available state (hole) in the valence band, and typically a photon is emitted. If this recombination happens before the electron-hole pair has contributed to the photovoltage, the energy is lost.

All these losses vary as a function of the semiconductor band gap. The E_g that minimises the combined total loss, roughly 1.4 eV, is the value that is used to calculate the Shockley-Queisser limit [29].

2.4 Third-generation photovoltaics

The Shockley-Quiesser limit does not tell us that all hope is lost if we want to make a more efficient solar cell. What it tells us is that a solar cell will need to be designed in a matter that addresses at least one of the losses in fig. 2.3 in order to reach an efficiency larger than $\sim$ 30%. On this point, a number of approaches have been suggested and attempted, all classified as "third-generation" photovoltaics [31].

2.4.1 Tandem

The only photovoltaic technique that has managed to surpass the Shockley-Queisser limit as of today are so called tandem-solar cells. In a tandem device, several semicon-

ductor materials with different band gaps are stacked on top of each other, each one designed to absorb a different portion of the sun's energy spectrum. In this way, carrier relaxation losses and sub-band gap losses can both be reduced. Such a device can thereby reach efficiencies significantly larger than the Shockley-Queisser limit [32]. Record efficiencies above 47% have been experimentally demonstrated by combining six different band gaps [33, 34]. Because these devices are composed of various semiconductor materials that can be rare and expensive, on top of high costs for growth substrates and fabrication facilities, they are so far are unable to compete with today's conventional Si solar cells when it comes to the price in dollars per kWh [35]. Because of their high efficiencies they are however considered for extreme applications where price is not the main issue, such as on satellites [36].

2.4.2 Multiple-exciton generation

In this technique, the goal is to use hot carriers with an energy at least two times larger than the band gap, $E_{\text{kin}} > 2E_{\text{g}}$. Such hot carriers can undergo impact ionization (see section (3.3)) to excite one or more additional electron-hole pairs across the band gap. In this way, the energy of one incoming photon may be used to generate more than one electron-hole pair. The existence of multiple exciton generation under optical excitation has been experimentally demonstrated mainly in quantum dot systems [37–40]. So far no devices operating at efficiencies or voltages above the Shockley-Queisser limit have been presented [41]. This approach entails a trade off:A $E_{\text{g}} \gg h\nu$ can yield a high current because many multiple electron-hole pairs can be generated, but the small E_{g} may limit the voltage (see section (3.3)). A larger E_{g} on the other hand means the photon energy will not be sufficient to generate multiple electron-hole pairs. For this reason it seems unlikely to by itself be the solution to a future high-efficiency photovoltaic device. While not to be dismissed, the technique is not addressed further in this thesis, and the reader is referred to existing reviews [41, 42].

2.4.3 Hot-carrier photovoltaics

A hot-carrier photovoltaic device attempts to directly utilise all the energy contained in the hot carriers, i.e., both E_{pot} and E_{kin}. This is possible if the hot carriers are used to extract work before they have time to relax. If this is done, then the size of E_{g} essentially does not matter. If the carrier relaxation losses are minimised then we see in fig. 2.3 that a small E_{g} will be the ideal choice to maximise conversion efficiency.

In 1982, Ross and Nozik [5] presented a seminal paper where they attempted the first full theoretical description of such a device, predicting that it could reach a conversion efficiency of 66%. Expanding on their description 15 years later, Würfel [43] made cal-

culations including impact ionization and solar concentration to suggest that an even higher efficiency of 85% could be reached. Since then, a significant number of theoretical works have been presented during the last 20 years where efficiency estimates range all the way from 1-85% [8]. This struggle in giving a consistent theoretical description of a hot-carrier solar cell hints at the complexity of the system. In fact, so far no fully functional hot-carrier solar cell has been realised at a macro scale, and the proof-of-principle devices that have been demonstrated are nowhere close to the higher predicted efficiencies [8].

There are a number of challenges that need to be overcome if a hot-carrier solar cell is to be realised in practice, the two overarching ones being:

1. Slowing down the hot-carrier relaxation process.
2. Designing energy selective filters capable of extracting work from hot carriers.

A significant amount of experimental work focused on challenge (1) have been done, typically utilising various low-dimensional effects to increase the hot-carrier lifetime, τ_{HC}, by modifying carrier-phonon interactions [8]. An increased τ_{HC} allows for more time to use the E_{kin} of the hot carriers for performing electrical work, before the energy is lost as heat. In a steady state situation, this means the hot-carrier distribution can maintain a higher effective temperature. These concepts are explained in more detail in Ch. (3), but challenge (1) is not specifically addressed in the experimental work of this thesis.

The experimental work in this thesis focuses on addressing challenge (2). In order to utilise the E_{kin} of hot carriers, a device design where only hot carriers of certain energies are transmitted is required [5, 43]. The energy selective structure through which the hot carriers are extracted is referred to as an *energy filter*. The short τ_{HC} means that extraction has to happen over short distances. Just as the first challenge, the second challenge is therefore tackled using low-dimensional structures, containing features on the nanometer-scale [7].

The concept of extracting hot carriers across an energy filter is very similar to the concept of nanoscale thermoelectric heat engines. The only real difference between such a thermoelectric device and a hot-carrier photovoltaic system is the way by which the energy is distributed amongst the carriers, as will be discussed during the next chapter. Many of the conclusions in this thesis are thus applicable to thermoelectric and hot-carrier photovoltaic systems. Indeed, Paper III is a study of a thermoelectric system, with potential implications for hot-carrier extraction.

3. Energetic charge carriers in semiconductors

The goal of this chapter is to give the reader an understanding of how energy is distributed amongst electrons in a solid, and in particular why hot carriers lose their kinetic energy so fast. A carrier distribution can be classified as being either in equilibrium or not in equilibrium. In this work, an equilibrium distribution is defined as one where the carriers can be described as a Fermi-Dirac distribution at a certain temperature. A non-equilibrium distribution of hot carriers is created during optical excitation. It is during the strive of the hot carriers to get back to an equilibrium distribution that their kinetic energy is lost. The mechanisms behind this relaxation process are introduced, as well as methods for slowing it down.

3.1 Equilibrium distribution

What is temperature? At its core, at a microscopic scale, temperature is defined as the energy contained in the movement of particles. One of the seven defining constants of physics, the Boltzman constant k_{B}, gives us a direct relation between the average kinetic energy, E_{kin}, of a free particle and its temperature, T. According to the equipartition theorem [44]

$$E_{\mathrm{kin}} = \frac{D}{2} k_{\mathrm{B}} T, \tag{3.1}$$

where D indicates the number of degrees of freedom. The equipartition theorem tells us that by increasing the temperature of a macroscopic object, one increases E_{kin} of its constituent particles.

In a system containing several electrons, the energy states that an electron can occupy is limited by the so called Pauli exclusion principle [45]. It states that no two electrons

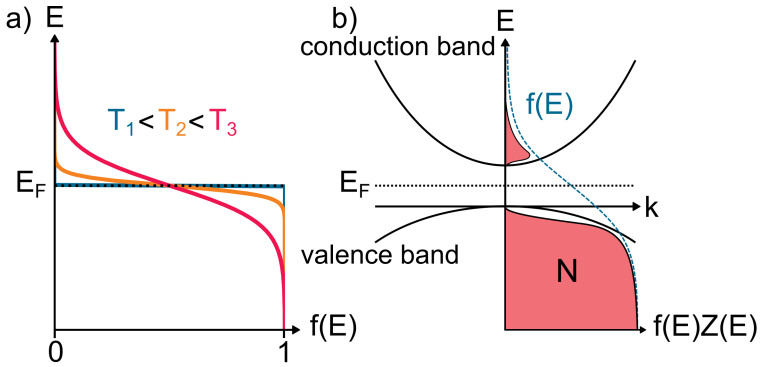

Figure 3.1: a) The Fermi-Dirac distribution, $f(E)$, plotted for three temperatures. b) The density of electrons occupying a solid, N, indicated as red region, will depend both on $f(E)$ and the density of states $Z(E)$.

in a system, with the same spin, can occupy the same energy state. Based on this, and the distribution of kinetic energy amongst electrons via inelastic scattering with each other, one can statistically derive the Fermi-Dirac distribution [46]. The distribution, $f(E)$, tells us the likeliness of finding an electron at a specific energy in a free electron gas

$$f(E) = \frac{1}{e^{(E-E_\mathrm{F})/k_\mathrm{B}T} + 1}. \tag{3.2}$$

The Fermi energy, E_F, is defined as the energy where the probability of a state being occupied by an electron is exactly 50%, i.e. $f(E_\mathrm{F}) = 0.5$.

At $T = 0$, we find the system in its state of lowest possible total energy, represented by the blue line in fig. 3.1(a). Here, all electron states are occupied up until E_F, and all states above are unoccupied. As T increases (orange and red line in fig. 3.1(a)), electrons gain E_kin, and scatter with each other more and more, such that the probability increases for finding an electron at energies above E_F. Since $f(E)$ is symmetric around E_F, each electron found above E_F entails a hole below E_F, with the probability $1 - f(E)$.

The Fermi-Dirac distribution is purely statistical, it determines the probability to find an electron at a certain energy, provided a state exists at that energy for an electron to occupy. To get the total density of electrons, N, the density of available states, $Z(E)$, needs to be factored in as well, so that

$$N = \int f(E)Z(E)dE. \tag{3.3}$$

Because $Z(E)$ is closely related to the band structure, it will differ for the conduction band, Z_CB, and the valence band Z_VB. The density of electrons in the conduction

band, n, and the density of holes in the valence band, p, can then be calculated as

$$n = \int_{\mathrm{E_C}}^{\infty} f(E) Z_{\mathrm{CB}}(E) dE, \tag{3.4}$$

and

$$p = \int_{-\infty}^{\mathrm{E_V}} 1 - f(E) Z_{\mathrm{VB}}(E) dE. \tag{3.5}$$

In fig. 3.1(b), a visualisation of how N may be distributed around the band gap of a semiconductor is shown. At $T = 0$, all electrons will be in the valence band and none in the conduction band, since E_{F} is found inside the band gap. At a finite T (as in the figure), $f(E)$, will range across the band gap, so that there is a finite probability of finding an electron at a state in the conduction band. Even if $f(E)$ is non-zero, $Z(E)$ approaches zero at the band edges and vanishes in the band gap. The resulting N, following eq. (3.3), is indicated as the red colored region .

Note that at any given T, a vast majority of electrons in a Fermi-Dirac distribution are found in an energetic range of a few $k_{\mathrm{B}}T$ around E_{F}. At room temperature, $T \approx 300K$ and $k_{\mathrm{B}}T \approx 30meV$, whereas typical values of E_{g} are on the order of 1 eV. In other words, $f(E) \ll 1$ in the conduction band, and fig. 3.1(b) is strongly exaggerated for visual purpose.

An *equilibrium* distribution will in this work refer to a reservoir in which all electrons can be described by a single Fermi-Dirac distribution at a certain temperature, T_0. A system may still contain several reservoirs all described by different T_0, each considered to be in equilibrium. In contrast, *thermal equilibrium* refers to a system where T_0 is the same in all reservoirs, in other words constant over space and time. This distinction will hopefully become make more sense after the next section, where distributions that cannot be described by eq. (3.2) are introduced.

3.2 Non-equilibrium distribution

A *non-equilibrium distribution* is a distribution which cannot be described by Fermi-Dirac statistics (eq. (3.2)). Such a distribution is for example created during optical excitation of a hot electron, as visualised in fig. 3.2(a). Typically, only a small portion of the electrons in the valence band are excited to hot electrons, while the majority still remains as an equilibrium distribution that can be characterised by temperature T_0. The occupation probability of the hot electrons cannot be described by $f(E, T = T_0)$. However, as they scatter and redistribute their kinetic energy amongst each other, they may form a uniform distribution (blue region in fig.3.2(a)). This distribution

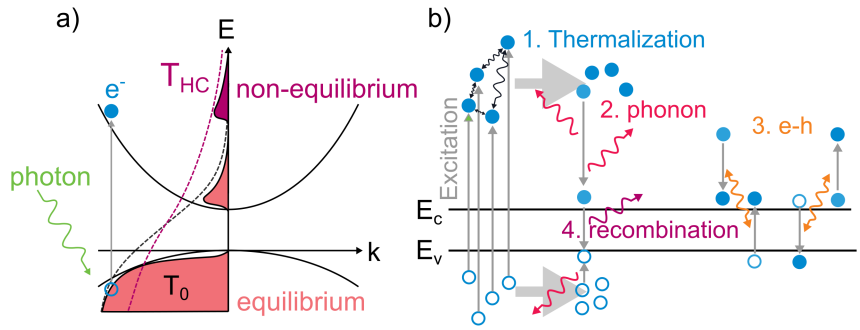

Figure 3.2: a) Optical excitation generates non-equilibrium hot carriers at energies above the Fermi-Dirac distribution. The hot-carrier population can be characterised by an effective temperature $T_{HC} > T_0$. b) Simplified image of the excitation hot-carrier relaxation process, highlighting 1) carrier-carrier scattering (thermalisation) 2) carrier-phonon scattering 3) electron-hole interactions such as impact ionization and Auger recombination 4) radiative recombination.

can often be rather well described as the tail of a Fermi-Dirac distribution given by an effective hot-carrier temperature $T_{\mathrm{HC}} > T_0$ [31, 43]. Note that T_{HC} is not a temperature in a strict sense, only a simplified attempt to describe the non-equilibrium distribution, which in reality is more complex [47].

3.3 Hot-carrier relaxation

After optically excited, the hot-carriers undergo a number of relaxation processes during timescales ranging from picoseconds to nanoseconds [3]. This means that if no further energy is put into the system, the hot carriers at T_{HC} will equilibrate with the electrons at T_0. Fully describing the formation and relaxation of the hot-carrier distribution is an intricate problem beyond the scope of this thesis, but a basic understanding of the processes involved will be helpful in discussing the results. The main processes involved in hot-carrier relaxation are summarised in fig. 3.2(b). Note that these processes need not occur in the order presented here but in reality they happen in parallel at various rates, depending on material system and excitation conditions. Table 3.1 shows rough timescales, τ, during which each process is likely to occur. It also shows the corresponding length, L, that an electron travels during that time based on the thermal drift velocity at room temperature, $(m_{\mathrm{e}}^* v_{\mathrm{th}}^2)/2 = 3k_{\mathrm{B}}T/2$, calculated for $m_{\mathrm{e}}^* = 1$ and $m_{\mathrm{e}}^* = 0.05$ [11].

1. Carrier-carrier scattering (thermalisation).

After excitation, hot carriers more or less immediately start to scatter with each other, redistributing their E_{kin}. Assuming the density of hot carriers is high enough for carrier-carrier scattering takes place, the distribution takes on a shape that can be

Table 3.1: Typical time scale, τ, and length scale, L, during which the various relaxation processes occur.

Process	τ	L, $m_e^* = 1$	L, $m_e^* = 0.05$
Carrier-carrier scattering [48]	$10^{-13} - 10^{-14}$ s	$1 - 10$ nm	$5 \cdot 1 - 10$ nm
Carrier-phonon scattering [3]	10^{-12} s	10^2 nm	$5 \cdot 10^2$ nm
Impact ionization [49]	$10^{-11} - 10^{-12}$ s	$10^2 - 10^3$ nm	$5 \cdot 10^2 - 10^3$ nm
Auger recombination [3]	10^{-10} s	10^4 nm	$5 \cdot 10^4$ nm
Radiative recombination [3]	$\geq 10^{-9}$ s	$\geq 10^5$ nm	$\geq 5 \cdot 10^5$ nm

approximated by Fermi-Dirac statistics at T_{HC}. Typically, T_{HC} will be different for the hot electron and the hot hole distribution, due to their different effective masses (see table 5.1)).

The process by which hot carriers reach a Fermi-Dirac distribution that can be characterised by T_{HC} is in this work refereed to as carrier *thermalisation*. This is not to be confused with the way the word thermalisation is sometimes used in photovoltaics-related literature, where it refers to the whole process of hot-carrier relaxation whereby T_{HC} reaches T_0.

During thermalisation, none of the E_{kin} is lost from the hot carriers, it is only redistributed amongst them.

2. Carrier-phonon scattering.

The main channel via which energy is dissipated from the hot carriers is via carrier-phonon scattering. To understand this process, we need to know that a phonon is a quasiparticle representing the wave/particle nature of elastic vibrations in the atoms of the lattice. A phonon consisting of atoms moving in a coherent wave is referred to as acoustic, while an out-of-phase movement, such that two neighbouring atoms move in opposite directions, is referred to as optical. Optical phonons only exist in solids with two or more atoms per base (such as a III-V compounds), because it's an ionic effect requiring an electrical dipole moment [50].

Carrier-phonon scattering is an inelastic event where the carrier scatters with the lattice and thereby sets off a vibration. The carrier loses some of its E_{kin} in generating a phonon. Via a series of carrier-phonon scattering events, the hot carrier releases most of its E_{kin}, and the distribution approaches the equilibrium distribution at T_0.

After generation, the dynamics of phonons may still have an impact on the distribution and relaxation of hot carriers. In polar materials, such as the III-V semiconductors studied in this work, carrier-phonon scattering mainly generate optical phonons [49] . These (higher-energy) optical phonons typically decay into multiple (lower-energy) acoustic phonons [51, 52]. A large build-up of acoustic phonons may result

in a phonon bottleneck effect that inhibits optical phonon relaxation [53–55]. This can in turn affect the carrier-phonon scattering rate, and lead to a modified T_{HC}. It is in principle also possible for acoustic phonons to be up-converted to higher energy optical phonons [56], and for optical phonons to be reabsorbed by carriers [57].

While overall, carrier-phonon scattering is a channel of loss for hot carriers, the complex dynamics describing the process will have a large impact on at which rates it happens. There are various ways in which these can be modified in low-dimensional structures [8], as discussed in more detail for nanowires in section (5.2). Acoustic phonons are responsible for heat conduction in a lattice. The relation between acoustic phonon scattering, thermal conductivity, and hot-carrier relaxation will also be explored further for nanowires in section (5.2).

3. Electron-hole interactions.

Electrons and holes form separate distributions that may be described by separate T_{HC}. Still, there is direct interaction between these two distributions in the form of processes such as impact ionization, Auger recombination, and various electron-hole scattering effects. Impact ionization is a process by which one energetic charge carrier loses parts of its energy in order to excite an additional electron-hole pair. Auger recombination (basically the reverse process) is the recombination of an electron hole pair, where the energy released becomes kinetic energy for another carrier [58].

4. Radiative recombination.

An electron in the conduction band can at any point relax to the valence band if there is a hole with a similar k. When an electron-hole pair is recombined, a photon is typically emitted with the same energy as the difference between the electron and hole. This is referred to as radiative recombination. It mostly involves carriers close to the band edge, with a low E_{kin} and similar k. As can be seen in table (3.1), radiative recombination is a relatively slow process [3].

3.4 Maintaining a hot-carrier population

The fast relaxation of hot carriers poses a serious challenge if the goal is to utilise their E_{kin}. Experimental efforts towards slowing down hot-carrier relaxation started during the 80's and 90's. Numerous works were published containing time-resolved studies of the hot-carrier relaxation process in quantum well systems, based mainly on GaAs/AlGaAs heterostructures [59–69]. These studies demonstrated how hot-carrier distributions in the quantum well could be decoupled from the equilibrium distribution at T_0 and described by T_{HC}. Observations of slower rates of relaxation, i.e.

increased lifetime τ_{HC}, were attributed to hampering in the phonon relaxation rate (i.e. phonon bottlenecks) and reduced carrier-phonon interactions. These effects can be expected in low-dimensional structures, partially due to phonon and electron confinement effects modifying their density of states [70]. More recently, similar observations have been made in a number of more exotic III-V quantum well systems [71–77]. Increased τ_{HC} have also been predicted and observed in several bulk materials, such as InGaN [78], due to their phonon and electron band structures [78–83]. While these studies are important, it should be noted that most of these studies are done at excitation powers significantly larger than that of the sun, and under excitation with very short pulses (down to femtoseconds). These are conditions that will not occur in a normal solar cell under operation. So far, significantly slowing down the hot-carrier relaxation under reasonable operational conditions seems to remain a challenge.

Any photovoltaic device operating under continuous illumination is said to be in a steady state situation, where there's a continuous flow of energy into and out of the device at various rates. The overarching rates in a hot-carrier photovoltaic system are summarised in fig. 3.3. Energy from the irradiation source enters the system at the rate Γ_{light}, which depends on the source of excitation and the absorption process. The distribution of excited hot carriers lose energy at rate Γ_{relax}, which is a sum of all the various rates for relaxation and recombination. As the hot carriers perform work, energy is extracted at rate Γ_{work}. The balance between these rates will determine the T_{HC} of the hot-carrier distribution that can be maintained in the system. A higher T_{HC} generally indicates more efficient thermalisation and a lower Γ_{relax}, so that the E_{kin} is only redistributed amongst hot carriers, but not lost. A lower T_{HC} on the other hand indicates a higher Γ_{relax}, i.e., E_{kin} is lost via carrier-phonon scattering and other loss mechanisms.

Experimental demonstrations where a hot-carrier population is maintained at T_{HC} significantly larger than T_0 in a steady state situation exist [19, 71, 84]. Perhaps most notably are the results of Tedeschi et al. [19],presenting T_{HC} more than a 100 K above T_0 in semiconducting nanowires. They observe an increase in T_{HC} with shrinking diameter of the nanowire, further discussed in section (5.2.2).

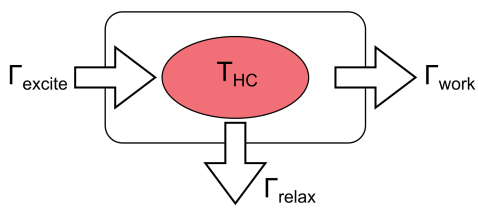

Figure 3.3: Overview of the rates of energy flowing in and out of a hot-carrier population.

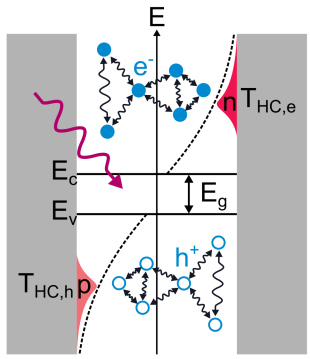

Figure 3.4: Conceptual schematic of a device were hot carriers are excited within an enclosed absorption region.

Intriguingly, recent theoretical work describing a hot-carrier photovoltaic device under steady state operation suggests that both a higher power, and efficiency, can be reached when the work is extracted from a non-thermalised, non-equilibrium distribution [47]. That is, a non-equilibrium which cannot be described by an effective temperature T_{HC}. In the study, the energy transfer between the sun, electrons, phonons, and work extraction is described by separate rates, and it is found that the system performs better when energy is extracted both from thermalised carriers, as well as carriers that have interacted with phonons. A conclusion that can be drawn from this when looking at experimental data is to not stare blindly at the T_{HC}. As stated before, T_{HC} is indeed not a real temperature. It is a simplification that allows us to approximately describe a hot-carrier distribution which in reality is more complex.

Conceptually, representing the distribution with T_{HC} is a very useful tool when explaining the operations of a hot-carrier photovoltaic device, and will thus continue to be used throughout this work to simplify discussion. Representing the hot-carrier population as a thermalised distribution also highlights the point that extracting work from a non-equilibrium distribution is in fact very similar to doing it from an equilibrium distribution. Which is what is done in a thermoelectric device, as detailed in section (4.1.2).

In a hot-carrier photovoltaic device, it is important to trap the hot-carrier population within a small absorption region, as pictured in fig. 3.4. Based on the previous paragraphs several reasons for this can be identified: the distance hot carriers diffuse before relaxing is under ideal cases $100 - 1000$ nm (see table (3.1)), focusing sunlight to a small region will increase the excitation power so that a higher density of hot carriers can be excited, and confinement effects in combination with increased hot-carrier density can contribute to increased τ_{HC} [85, 86]. This means that in the absorption region, hot electron and hole temperatures, $T_{\mathrm{HC,e}}$ and $T_{\mathrm{HC,h}}$ respectively,

may be maintained above T_0.

Assuming a system as the one in fig. 3.4 where hot carriers effectively thermalise at a high T_{HC}, the next challenge is how to extract work from the hot-carrier distribution. This is where the work of this thesis enters the picture. Power can be generated if hot carriers are extracted from the absorption region via energy selective filters. The design of these filters will determine the rate Γ_{work}, as well as the power that can be produced by the device at what efficiency. Going back to fig. 3.3, Γ_{work} will also have a second-hand effect on the T_{HC} that can be maintained in the absorption region. This thesis investigates how to design and experimentally realise such energy filters using nanowires. The next chapter explores and compares various types of energy filters.

4. Charge-carrier extraction for power generation

Given a distribution of charge carriers that contain energy in the form of equilibrium or non-equilibrium, how can the energy be used to generate electrical power? This chapter introduces two conventional methods for generating power from: a) An equilibrium distribution using the thermoelectric effect, extraxting the kinetic energy, E_{kin}, contained in a temperature gradient. b) A non-equilibrium distribution using the photovoltaic effect, extracting potential energy, E_{pot}, from optically excited electron-hole pairs. A hot-carrier photovoltaic device needs to extract energy of both types, E_{pot} and E_{kin}, and borrows concepts from both fields. In particular, there already exists a lot of valuable knowledge about using energy selective filters to realise nanometer-scale thermoelectric devices.

4.1 Current generation

In order to generate an electrical current and produce power from energy contained in charge carriers, a mechanism that causes a net flow of electrons and holes in opposite directions is required. Here, three approaches are introduced: the photovoltaic, the thermoelectric, and the hot-carrier photovoltaic device.

4.1.1 Conventional photovoltaics

In a conventional photovoltaic device, optically excited electron-hole pairs are separated via built-in electric fields in the semiconductor, so called pn-junctions, in order to generate an electrical current. As will be made clear, this approach only allows for making use of the potential energy, E_{pot}, that carriers gain by excitation across the band gap, but none of the kinetic energy, E_{kin}, contained in hot carriers.

Optical excitation at position $\vec{r}$ leads to a local increase in the density of electrons in the conduction band, $n(\vec{r})$, and holes in the valence band, $p(\vec{r})$, as seen in fig. 4.1(a). Note that unless the intensity of excitation is extremely high, only a small fraction of the total available number of carriers will be excited. It is thus safe to say that the overall (equilibrium) Fermi-Dirac distribution, at temperature T_0, remains unchanged and constant throughout the semiconductor. Until recombined, the excited carrier distributions, $n(\vec{r})$ and $p(\vec{r})$, are non-equilibrium distributions that cannot be described by T_0.

Anywhere there exists a gradient in carrier concentration, $\nabla n(\vec{r})$ and $\nabla p(\vec{r})$, carriers in a region with higher concentration diffuse to regions with lower concentration. The ensuing diffusion current for electrons, $\vec{J}_{\text{n, diff}}$, and holes, $\vec{J}_{\text{p, diff}}$ is described as

$$\vec{J}_{\text{n,diff}} = qD_{\text{n}}\nabla n(\vec{r}), \tag{4.1}$$

and

$$\vec{J}_{\text{p,diff}} = -qD_{\text{p}}\nabla p(\vec{r}). \tag{4.2}$$

The diffusion coefficient of electrons (holes), D_{n} (D_{p}), is defined generally as

$$D_{\text{n,p}} = \mu_{\text{n,p}}\frac{k_{\text{B}}T}{q}, \tag{4.3}$$

where $\mu_{\text{n, p}}$ stands for electron, and hole mobility respectively [87].

Because of the opposing signs of electrons and holes, the two diffusion currents will typically work against each other, so that the total current $\vec{J}_{\text{total}} = \vec{J}_{\text{n,diff}} + \vec{J}_{\text{p,diff}} = 0$. A difference between $\nabla n(\vec{r})$ and $\nabla p(\vec{r})$ can thus lead to a non-zero $\vec{J}_{\text{total}}$.

In the conventional photovoltaic device, a pn-junction containing a "built-in" electric field, $\vec{E}$, sweeps electrons and holes in opposite directions. In this way, the side of the pn-junction where electrons are swept will have a high injection of $\nabla n(\vec{r})$, and thus $\vec{J}_{\text{n, diff}} > \vec{J}_{\text{p, diff}}$. On the other side of the junction the situation is opposite, $\vec{J}_{\text{n, diff}} < \vec{J}_{\text{p, diff}}$, so that both sides generate a non-zero $\vec{J}_{\text{total}}$ in the same direction.

Fig. 4.1(b) shows a pn-junction photovoltaic device operating under *short-circuit* conditions. That is, connected by a circuit with negligible resistance, $R = 0$. In this configuration, all separated electron-hole pairs will contribute to the short-circuit current, I_{SC}. If the circuit is instead connected in series with an infinite resistance, as in fig. 4.1(c), it is referred to as *open-circuit* conditions. Under such conditions, no current will flow. As carriers are separated, a difference in chemical potential, μ_{L} and μ_{R}, builds up on the two sides. The difference in chemical potential results in a voltage $eV = \mu_{\text{R}} - \mu_{\text{L}}$. The voltage build up will continue until it reaches the open-circuit

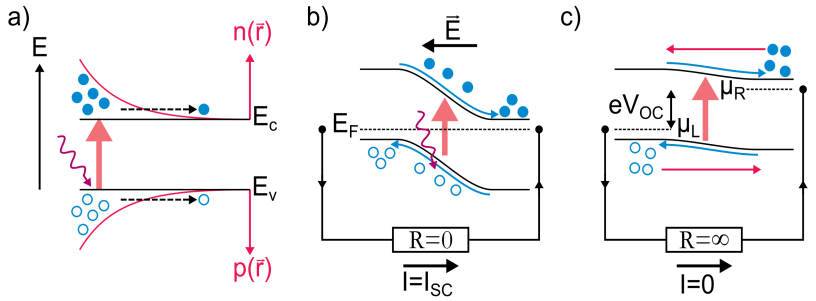

Figure 4.1: a) Optical excitation of electron-hole pairs and ensuing diffusion as a result of b) gradient in carrier concentration but constant temperature. c) The electric field of a pn-junction is used to separate excited electron-hole pairs, increasing $n(\vec{r})$ on one side and $p(\vec{r})$ on the other, resulting in a short-circuit current, I_{SC}, across a circuit with resistance $R = 0$. At open-circuit conditions (series connection with infinite resistance), the separation of charge carriers results in the build up of open-circuit voltage V_{OC}.

voltage, V_{oc}. At this point, the difference in μ_L and μ_R causes a back-flow of carriers (red arrow in fig. 4.1(b)) that exactly cancel out the flow caused by excitation.

The largest amount of energy that can be extracted from the device is determined by $\mu_R - \mu_L$. However, in order for the device to produce power, $P = IV$, it must be connected in series to a finite resistance, $0 < R < \infty$, where $eV < E_g$ will always be the case. Since $E_g = E_{pot}$, this means that any of the E_{kin} possessed by a hot carrier cannot contribute to producing power. A solar cell based on a pn-junction is in other words only able to harvest the E_{pot} component of a photo-excited carrier.

Two parameters of importance for the performance of a photovoltaic device is the conversion efficiency, η_{PV}, and the fill factor, FF, defined as

$$\eta_{PV} = P/P_{in}, \tag{4.4}$$

and

$$FF = \frac{P_{max}}{I_{SC}V_{OC}}. \tag{4.5}$$

Here, P_{in} is the incident power from the source of illumination, P the power produced by the device, and P_{max} the maximum power the device can produce. Eq. (4.5) ranges between 0 and 1, where the ideal case of $FF = 1$ would yield $P_{max} = I_{SC}V_{OC}$. A good solar cell on the market today typically reaches $FF \approx 0.8$ [88].

4.1.2 Thermoelectric

In contrast to a photovoltaic device, a thermoelectric device relies on E_{kin} as the resource available for power generation. The thermoelectric device produces power by

connecting two equilibrium distributions at different temperatures, a "hot" reservoir at temperature T_{H}, and one "cold" reservoir at T_{C} (see fig. 4.2(a)).

The difference in the Fermi-Dirac distributions at the hot, $f_{\mathrm{H}}(E)$, and cold, $f_{\mathrm{c}}(E)$, sides will result in a variation in the spectral carrier density. At energies above E_{F} this causes a diffusion towards the cold side, and at energies below E_{F} a diffusion towards the hot side. At all points, the distributions remain in equilibrium, according to the definition in section (3.1), since no injection of electrons or holes is taking place. This means that unless additional energy selectivity is introduced, $n(\vec{r})$ and $p(\vec{r})$ are constant throughout the system, in contrast to the photovoltaic system in fig. 4.1.

In order to generate a thermoelectric current, some mechanism that promotes electron transport in one direction over the other is required. In any semiconductor there will naturally be a variation in the electronic states available, due to variations in the density of states. This introduces an energy dependence in the carrier transport such that there is always a built-in preferred direction for thermoelectric transport. The preference in directionality and magnitude of thermoelectric current can be described by the Seebeck coefficient

$$S = -\frac{\Delta V}{\Delta T} = -\frac{V_1 - V_2}{T_1 - T_2}. \tag{4.6}$$

Where V is voltage and sub-scripts 1 and 2 refer to two different reservoirs at different temperatures. The total current, J, in such a system is then given by

$$J = \sigma V \underbrace{-\sigma S \nabla T}_{J_{\mathrm{th}}}, \tag{4.7}$$

where σ is the electrical conductivity and J_{th} the thermoelectric current.

Eq. (4.7) is said to describe the *linear response* transport region, where current depends linearly on the ΔV and ΔT. The transport is in a linear response regime as long as any change in the carrier distribution is small over distances on the order of the electron mean-free-path [89, 90]. That is, as long as ΔV and ΔT are small in comparison to T.

Almost all bulk systems operate in linear response since the electron mean free path is typically on the order of 100 nm. Here, the thermoelectric performance of a system is quantised by linear response parameteres σ, S, and thermal conductivity k, which can only be tuned by choice of material. This puts limitations on what values that can be attained [91, 92].

In contrast, a system under *nonlinear* response refers to one in which the current takes

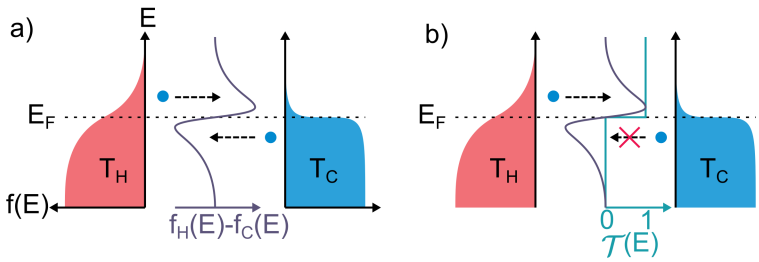

Figure 4.2: a) Connecting a hot and cold electron reservoir, electrons will diffuse between the reservoirs anywhere there is a difference in Fermi-Dirac distributions. c) A current can be generated by the introduction of an energy selective filter described by its transmission, $\mathcal{T}(E)$.

on any form of higher order dependencies on V and ΔT, such that

$$I = \underbrace{\alpha I + \beta \Delta T}_{\text{linear response}} + \gamma V^2 + \delta \Delta T^2 + \epsilon V \Delta T + \zeta V^3 + \kappa \Delta T^3 + \ldots \tag{4.8}$$

where α,β,... are constants containing physical parameters describing the particular system.

During the 90's, it was realised that using low dimensional structures, such as quantum wells and nanowires, one can enter transport regions of nonlinear response. Here, large variations in V and ΔT can be observed on distances shorter than the electron mean-free-path [23, 93, 94]. In particular, such systems can be realised by introducing variations in chemical composition that result in energy filters with highly energy selective transmission at the nanometer scale [95–98].

The nature of the energy selective filters are best characterised by their transmission function, $\mathcal{T}(E)$, a value between 0 and 1 that describes the probability of transmission for a carrier at a certain energy. Fig. 4.2(b) shows a simple example where $\mathcal{T}(E) = 0$ below E_F, and $\mathcal{T}(E) = 1$ above E_F. The introduction of this $\mathcal{T}(E)$ blocks the thermoelectric transport in one direction, resulting in a net flow of electrons from hot to cold.

When the shape of $\mathcal{T}(E)$ determines the current, transport is typically in the nonlinear regime. The current between two reservoirs, separated by $\mathcal{T}(E)$, is often times easier described by the Landauer-Büttiker scattering framework [99] where

$$I = \frac{e}{2\pi\hbar} \int \mathcal{T}(E)[f_\mathrm{H}(E) - f_\mathrm{C}(E)]dE. \tag{4.9}$$

This equation highlights the importance of choice of $\mathcal{T}(E)$ in a nanoscale thermoelectric device. Both the factor $\mathcal{T}(E)$ and $f_\mathrm{H}(E) - f_\mathrm{C}$ may contain nonlinear dependencies, as discussed further in section (4.2).

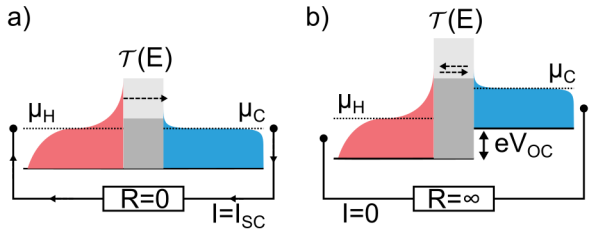

Figure 4.3: a) A thermoelectric short-circuit current is generated between a hot and a cold reservoirs separated by an energy filter with transmission function $\mathcal{T}(E)$. b) Under open-circuit conditions a voltage V_{OC} is built up until no net current flows between the two reservoirs.

Fig. 4.3 shows a thermoelectric device with an energy selective filter, characterised by a transmission function $\mathcal{T}(E)$, operating in series with a resistance. The short-circuit current, fig. 4.3(a), is simply the net flow of carriers from the hot to cold reservoir. With a finite resistance, 4.3(b), a voltage builds up and the difference in μ_H and μ_C results in a modification of $f_H(E) - f_C(E)$, such that a flow in the opposite direction of I_{SC} is generated (see eq. (4.7)). At open-circuit conditions, the flow of carriers from both sides exactly cancel out, such that $I = 0$. Compared to the photovoltaic system introduced in section (4.1.1), in such a thermoelectric system it is ΔT and $\mathcal{T}(E)$ that sets the fundamental limit to V_{OC}, as opposed to E_g.

The overall efficiency of energy conversion in a thermoelectric system is defined as the ratio between the produced power and the heat flow going out of the hot reservoir, J_h,

$$\eta_{TE} = \frac{P}{J_h}. \tag{4.10}$$

The maximum achievable efficiency for a heat engine is limited above by the Carnot efficiency [91]

$$\eta_C = 1 - \frac{T_C}{T_H}, \tag{4.11}$$

such that $\eta_{TE} \leq \eta_C$. Note that η_C approaches 1 as we go toward a situation where $T_H >> T_C$. Further, when a thermoelectric system is operated at the point where it produces maximum power (typically where a power-producing device is operated), the maximum efficiency that can be extracted is described by the Curzon-Ahlborn efficiency [100]

$$\eta_{CA} = 1 - \sqrt{T_C/T_H}. \tag{4.12}$$

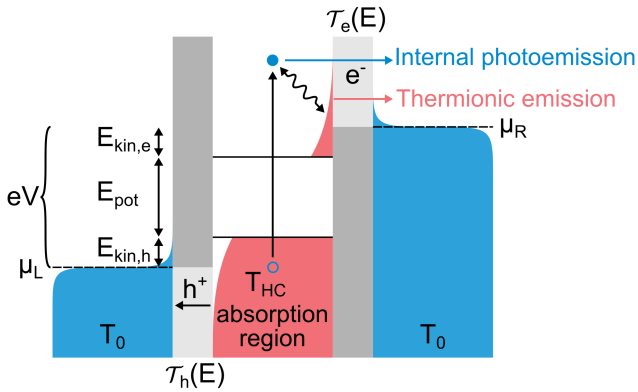

Figure 4.4: Hot carriers are generated inside the absorption region, electrons (holes) are extracted to the right (left) via energy filters $\mathcal{T}_e(E)$ ($\mathcal{T}_h(E)$). For simplicity, it is here assumed that hot electrons and hot holes both thermalise at the same T_{HC}.

4.1.3 The hot-carrier photovoltaic device

The hot-carrier photovoltaic device needs to generate power using both E_{pot} and E_{kin}. In this sense it combines concepts both from the conventional photovoltaic and thermoelectric device. The need for high control in synthesis of nano-structures explains why barely no experimental work existed on hot carriers before the 21st century [31]. During the last 20 years, with the maturity of nanofabrication techniques, a number of experimental demonstrations of hot-carrier extraction have been reported via energy filters in the form of resonant tunneling structures [101–107], quantum wells [108–111], and colloidal particles [112]. This section will introduce the ideal vision for how a hot-carrier solar cell could be designed, an approach which by today hasn't been fully demonstrated in experiment.

A hot-carrier population is ideally confined within a small region, as discussed in section (3.4) (see fig. 3.4). The absorption region depicted in fig. 4.4 can be considered a hot reservoir with an effective temperature hot-carrier temperature T_{HC}. On either side of the absorption region are equilibrium distributions, at temperature T_0, so that a temperature difference $\Delta T = T_{HC} - T_0$ exist in both directions. For simplicity, it is here assumed that T_{HC} is the same for hot electrons and holes.

In order to generate a current, energy filters that selectively extract carriers from the hot to the cold regions are required [7, 8, 43]. In fig. 4.4 this is depicted as light grey regions, indicating a transmission function that is tailored to extract either hot electrons, $\mathcal{T}_e(E)$, or hot holes, $\mathcal{T}_h(E)$. The voltage, and therefore the energy, that can be extracted from such a device is given as $eV = \mu_R - \mu_L = E_{pot} + E_{kin,e} + E_{kin,h}$. Compared to a photovoltaic device, the energy extracted is no longer bounded above by E_g. Compared to a thermoelectric device, additional energy is gained from

the E_{pot} that results from excitation of electron-hole pairs across the band gap [113]. Because the hot-carrier distribution is not an equilibrium distribution, it is possible to experimentally achieve $\Delta T > 100$ K [19, 71, 72, 84]. Note that realising such a high ΔT over a distance on the order of nanometers is very challenging to achieve in a traditional thermoelectric device.

Carrier extraction from the absorption region can be described as either *internal photo-emission* or *thermionic emission*, illustrated in fig. 4.4. The former, also known as ballistic transport, refers to hot carriers extracted before they have thermalised and redistributed any of their E_{kin}. Such extraction is typically only possible within approximately 100 fs, or over distances shorter than 100 nm (see table (3.1)). Thermionic emission is the extraction of hot carriers that have had time to thermalise with other hot carriers and form a distribution at T_{HC}.

A power generating device operating on the principle of internal photo-emission has no advantages in terms of efficiency compared to conventional photovoltaics, since all of the E_{kin} will be lost after the carrier has been extracted and relaxes. If extracted via thermionic emission, the E_{kin} of hot carriers can instead contribute to maintaining a high T_{HC} so that a higher η_{TE} can be achieved. For this reason, it is generally expected that a hot-carrier photovoltaic device should be operated under conditions where carriers are extracted via thermionic emission [43].

There is no standardised way for describing the efficiency of a hot-carrier photovoltaic device. Looking at a complete device, it is evaluated in terms of η_{PV}, but for describing several processes within the device it can prove useful to evaluate its performance also in terms of η_{TE}.

4.2 Energy filters

The shape of $\mathcal{T}(E)$ in the energy filters will have a huge role in both the conversion efficiency and power that can be generated in a hot-carrier photovoltaic device. In the ideal device, the energy filter allows for a significant rate of electron extraction, Γ_{work}, against a large voltage $eV > E_{\text{g}}$, while at the same time avoiding detrimental effects on T_{HC} due to the rate of extraction, Γ_{work}. So far, few theoretical studies exist on the role of $\mathcal{T}(E)$ when extracting carriers from a non-equilibrium (hot-carrier) distribution [47]. However, since the concept is very similar to that of extracting carriers from a hot to a cold reservoir at equilibrium, a lot can be learnt by looking at the literature for thermoelectric heat engines [90, 114–116].

For thermoelectric heat engines, the choice of energy filter always comes at a trade-off between the power it can produce, and at which efficiency. Increasing one typically

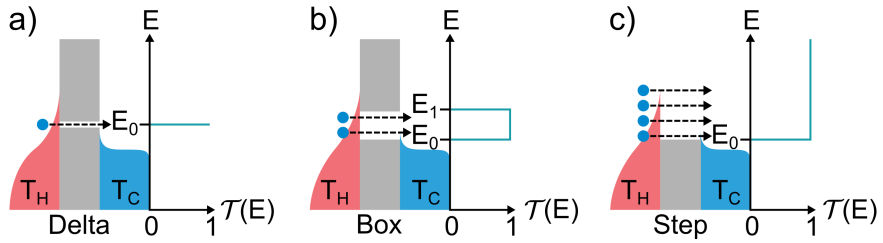

Figure 4.5: A hot and cold reservoir separated by a transmission function, $\mathcal{T}(E)$, with a) delta-shape, b) box-shape, and c) step-shaped.

decreases the other. Three types of energy filters are now discussed, with various pros and cons when it comes to this trade-off. They are categorised after the shape of their transmission function $\mathcal{T}(E)$; delta-,box-, or step-shaped. Due to the symmetry of the system in fig. 4.4, the discussion is simplified by focusing only on the extraction of hot electrons, while any conclusions remain equally true for the extraction of hot holes.

4.2.1 Delta-shape

The type of transmission depicted in fig. 4.5(a) only transmits electrons at one specific energy, E_0,

$$\mathcal{T}(E) = \begin{cases} 1, & E = E_0 \\ 0, & \text{otherwise.} \end{cases} \tag{4.13}$$

The delta-shaped transmission allows for reversible transport between the two reservoirs without the generation of any entropy, a requirement to reach η_C [10, 115]. In practice, a perfect delta function cannot be achieved in experiment. However, a Lorentzian function where transmission is allowed within a full width at half maximum, $\Delta\epsilon$, centered around E_0, can be realised using resonant tunneling structures on quantum dots [90, 117]. For $\Delta\epsilon \ll k_B T_{HC}$ (typically below 1 meV), it is in principle possible to reach η_{TE} near η_C when extracting electrons between two reservoirs [114, 118]. Reaching η_C will require carefully placing E_0 at a specific value where $f_H(E) = f_C(E)$, a value that will depend both on the chemical potential and temperature of the two baths [115]. At such a point, transport between the two reservoirs can be reversible at no cost of entropy, and thus the temperature of the two reservoirs is preserved. It is in principle also possible to reach η_C in a system with two cold reservoirs, and two energy filters, as depicted in fig. 4.4 [119]. Experimentally, devices with resonant tunneling structures have been realised that reach η_{TE} up to 70% of η_C [120].

A delta- or Lorentzian-shaped $\mathcal{T}(E)$ is the type of transmission most often used when

describing the ideal hot-carrier photovoltaic system [5, 43, 48, 121]. Because it effectively blocks internal photo-emission, so that only thermalised carriers are extracted, and because it minimises entropy losses, it allows for theoretical predictions of η_{PV} up to 85% [43]. Experimental demonstrations of hot-carrier extraction via resonant tunneling structures have been realised, but so far at low efficiencies [101, 103, 105, 106].

In an energy conversion device the factor that one typically wants to maximise is however first most the output power, ideally still at a decent efficiency. A device operating at the point of η_{C} in fact produces no power, as it is a reversible process that generates no entropy [115]. In the field of thermoelectrics it has been recognised for quite some time that the delta-shaped transmission function results in a very low power output [122, 123]. Simply put because a narrow transmission only permits the transport of a small amount of electrons, resulting in a low Γ_{work}. Considering hot-carrier photovoltaics, more recent work have started to acknowledge that what one needs to maximise is really the efficiency at the point of maximal power production, $\eta_{\mathrm{PV}}^{\mathrm{max\ P}}$, rather than η_{PV} [8, 47].

It should also be noted that the tuning of energy levels inside a resonant tunneling device is a process that already in lab environments is a time-consuming and difficult process for a single device. A large voltage bias will also seriously distort and degrade $\mathcal{T}(E)$ [124]. Scaling up the approach of using delta shaped transmission for significant power production is, if at all possible, no small challenge.

4.2.2 Box-shape

The box-shaped transmission function, fig. 4.5(b), transmits all electrons in a window between energies E_0 and E_1,

$$\mathcal{T}(E) = \begin{cases} 1, & E_0 < E < E_1 \\ 0, & \text{otherwise.} \end{cases} \tag{4.14}$$

Here, the window $E_1 - E_0$ can be up to several 100 meV wide [47, 123, 125–127], much larger than the with of the Lorentzian transmission of resonant tunneling devices that is typically on the order of 1 meV [114, 118]. Out of the types of $\mathcal{T}(E)$ described in this chapter, this shape has been theoretically predicted to yield the highest $\eta_{\mathrm{TE}}^{\mathrm{max\ P}}$ [123, 127]. This is possible since the wider transport window allows for a larger power output than the delta-shaped. The wider the box, power output increases, while the efficiency decreases (as entropy generation increases). The width thus allows for tuning the trade-off between power and efficiency to find the ideal point of operation [123]. Recent theoretical work has also reported that a box-shaped $\mathcal{T}(E)$ maximises η_{PV} in a hot-carrier photovoltaic device where carriers are extracted by thermionic emission (after thermalisation) [47].

While it may be the best approach in theory, realising a box-shaped $\mathcal{T}(E)$ in practice is challenging and has to the authors knowledge not been experimentally accomplished. Theoretical work suggests it could be realised by connecting a series of quantum dots in a chain-like structure [128–130], as well as in graphene nanoribbons functionalised by heavy adatoms and nanopores [126].

4.2.3 Step-shape

The third type of energy filter, fig. 4.5(c), transmits all electrons above a certain threshold, E_0,

$$\mathcal{T}(E) = \begin{cases} 1, & E > E_0 \\ 0, & E < E_0. \end{cases} \tag{4.15}$$

The step-shaped $\mathcal{T}(E)$ offers the highest power output because it allows for the largest Γ_{work} [47, 122]. It comes at a cost of efficiency, since entropy increases, and thus energy is lost, when electrons are transmitted at energies far above E_0. This is especially true in a hot-carrier photovoltaic device, where a big portion of hot carriers may be extracted via internal photoemission. The reduction in efficiency compared to a box-shaped transmission saturates when $E_1 - E_0 \approx 1$ eV, and theory suggests an efficiency $\eta_{\text{PV}} \sim 50\%$ could still be achieved [131]. The trade-off between P and η_{TE} is however significantly better than that of a delta-shaped transmission. One theoretical paper predicts that the efficiency at maximum power conditions can reach $\eta_{\text{TE}}^{\text{max P}} = 0.36\eta_{\text{C}}$ in a 1D step-shaped $\mathcal{T}(E)$, compared to $\eta_{\text{TE}}^{\text{max P}} = 0.17\eta_{\text{C}}$ for delta-like transmission [122].

The step-shaped $\mathcal{T}(E)$ might be the most realistic approach to realise a hot-carrier photovoltaic device [8]. It offers the highest power output of the types presented here, a decent trade-off between power and efficiency, and is by far the easiest structure to realise in an experimental device. Proof-of-principle devices have been realised using nanowires where hot carriers are extracted over epitaxially defined, 1D-like, rectangular-shaped, potential barriers [21, 22]. This type of system is further investigated in Papers I and II.

4.2.4 Nonlinearities in energy filters

Which are the physical sources of nonlinearities that can arise in a system with two reservoirs separated by an energy filter? The Landauer-Büttiker scattering framework eq.(4.9) highlights that nonlinear dependencies can be observed both in the transmission function $\mathcal{T}(E, V)$, and the range of particles that participate in transport

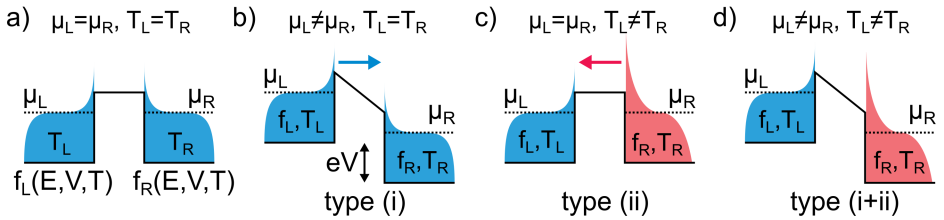

Figure 4.6: Two electron reservoirs separated by a rectangular potential barrier. a) without any bias, b) with voltage bias, c) with thermal bias, and d) with thermal and voltage bias

$f_{\mathrm{H}}(E, T_{\mathrm{H}}, V) - f_{\mathrm{C}}(E, T_{\mathrm{C}}, V)$. When changes in voltage and temperature are considered, the transmission is a function of energy and voltage, while the Fermi-Dirac distribution is a function of energy, voltage (V shifts the chemical potential), and temperature. Nonlinear effects can thus be separated as having two different origins, illustrated for a rectangular potential barrier (step-shaped $\mathcal{T}(E)$) separating a left (L) and right (R) reservoir in fig. 4.6:

(i) Voltage induced changes.
An electrical bias will change $\mathcal{T}(E, V)$ as it changes the shape of the potential barrier, see fig. 4.6(b). It will also change the range of particles that participate in transport, since $\mu_{\mathrm{L}} \neq \mu_{\mathrm{R}} \rightarrow f_{\mathrm{L}} \neq f_{\mathrm{R}}$.

(ii) Temperature induced changes.
A thermal bias will alter the range of particles that participate in transport, fig. 4.6(c), since $T_{\mathrm{L}} \neq T_{\mathrm{R}} \rightarrow f_{\mathrm{L}} \neq f_{\mathrm{R}}$.

A thermoelectric device producing power will operate in a regime where both V and ΔT are non-zero (fig. 4.6(d)), such that nonlinearities of both origin (i) and (ii) can exist. Of relevance for the work in this thesis is whether operating in this nonlinear region can allow for tuning parameters that are typically linear.

The fill factor FF, eq. (4.5), is an important parameter to tune in conventional photovoltaic devices. It can be visualised, as shown in fig. 4.7, as the ratio of the area of a box spanned by P_{max}, divided by the area spanned by I_{SC} and V_{OC}. In other words, for a given I_{SC} and V_{OC}, the shape of the current-voltage curve is what determines P_{max}. A thermoelectric device typically operates in a linear response region, where FF is always 0.25 [132]. For this reason the fill factor is usually not mentioned in the context of thermoelectrics. In a thermoelectric device where transport is dominated by the shape of an energy filter this need no longer be the case. Two cases are indicated in fig. 4.7: a more "concave" shape of the curve, resulting in $FF < 0.25$ and a decreased P_{max}, and a more "convex" shape, resulting in $FF > 0.25$ and thereby P_{max}.

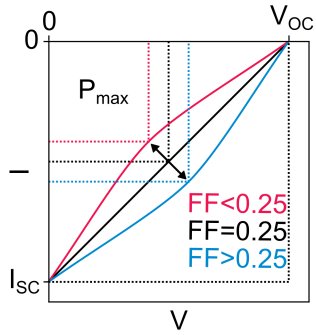

Figure 4.7: Current-voltage curves with three different fill factors. At linear response $FF = 0.25$ (black line), while a nonlinear curve can yield a smaller (red) or larger (blue) FF.

Paper III experimentally demonstrates a system containing nonlinearities of both type (i) and (ii), where FF can be tuned in both directions by using an asymmetric energy filter. This is further discussed in section (6.2).

4.3 Hot-carrier diffusion length

An important aspect of designing a hot-carrier photovolatic device is how far away from the point of excitation a hot carrier can diffuse and still have sufficient energy to surpass an energy filter, here defined as the effective hot-carrier diffusion length L^*_{HC}. When designing, e.g., the width of the absorption region in a hot-carrier photovoltaic device, L^*_{HC} will need to be considered. For a first estimate of the length scales to be expected for L^*_{HC}, expected diffusion lengths based on thermal drift velocity can be found in table (3.1). The distance before significant carrier relaxation takes place is seen to be around the order of $100 - 1000$ nm.

To be more precise, L^*_{HC}, in a device will depend on the interaction between a multitude of parameters such as the initial distribution of excited hot carriers, various scattering rates and transport properties of the material, as well as the type and shape of energy filter used for extraction. Instead of trying to theoretically predict these, a simple model for experimentally determine L^*_{HC} for a particular system is applied in Papers I and II. All the hot-carrier relaxation rates are assumed to be exponential decays, and the model only considers one dimension (along the nanowire axis). The probability, $P(z)$, of finding a hot carrier at a distance, z, from it's point of excitation is expected to decrease exponentially such that

$$P(z) \sim e^{-z/L^*_{\mathrm{HC}}}. \tag{4.16}$$

In Papers I and II this proportionality is used to make experimental estimates of L^*_{HC}, see also section (6.1).

The following chapter will look into why and how semiconducting nanowires can be used to realise devices that use energy filters to extract work from both equilibrium and non-equilibrium carriers.

5. Nanowire hot-carrier photovoltaic devices

Semiconducting III-V nanowires are elongated objects with a high length-to-diameter aspect ratio, and a diameter on the order of a hundred nanometers or smaller. Due to their geometry, and the ability to incorporate heterostructures within them with high precision and control, they allow for the tailoring of electronic, thermal, and optical properties [9, 12–14, 133]. Nanowires are being considered for a wide range of applications such as transistors [134], light emitting diodes [135], solar cells [133], quantum computing [136, 137], and thermoelectrics [120, 138].

Previous chapters introduced the two main challenges that need to be addressed in order to realise a hot-carrier photovoltaic device: (i) maintaining a steady state hot-carrier population at an elevated effective temperature $T_{HC} > T_0$, and (ii) extracting a selection of these hot carriers via energy selective filters in order to produce power. This chapter introduces nanowires as a platform with the potential to address both of these challenges.

5.1 Nanowire growth

The nanowires in this thesis are grown epitaxially via a technique generally referred to as vapor-liquid-solid (VLS) [139]. Droplets of Au, so called seed particles, are used to catalyse the growth of gaseous group III and V elements onto a solid substrate. The seed particles can be defined, e.g., by lithography, or deposited as aerosol particles. The size of particles will determine the nanowire diameter.

During growth, the substrate containing the seed particles is placed inside a vacuum chamber. Various precursors containing group III or V materials are injected in the chamber. As the substrate is heated, precursor molecules undergo pyrolysis at the

Au interface and get absorbed by the droplet. Once the droplets are saturated, they facilitate crystal growth at the liquid-solid interface directly underneath them. In this manner, nanowires are grown one atomic layer at a time. For more details see, e.g., Ref. [140, 141].

Nanowires are particularly useful to the work in this thesis because their growth enables the realisation of energy filters tailored to extract hot carriers. The material composition of the nanowire can be changed abruptly by turning on and off the flow of various precursor gasses [13]. At the same time, the small diameter of the nanowire reduces the strain on the atomic lattice, which allows for the combination of III-V compounds with a large mismatch in lattice spacing [12]. Since all the materials differ in band gap and relative band-offsets, heterostructures in the nanowire can be designed to match a desired potential landscape. In this way, energy filters with various types of transmission functions can be engineered.

The specific technique used to synthesise the nanowires used in this thesis is chemical beam epitaxy (CBE) [142]. CBE is performed in an ultrahigh vacuum environment, allowing the flow of gaseous particles to be directed in a beam [143]. The nanowires used in Papers I-III are grown from aerosol gold particles with a diameter of 40-50 nm, on InAs (111)B substrates. They consist of mainly InAs with some heterostructures of InP and $InAs_{1-x}P_x$, all in wurtzite (WZ) crystalline structure except for some stacking faults [144].

5.2 Alterations of phonon and hot-carrier dynamics

Simply due to the geometrical shape of nanowires, one can expect changes in the dynamics of both phonons and charge carriers, affecting parameters such as the hot-carrier relaxation time τ_{HC} [20, 145], effective temperature T_{HC} [18, 19], and thermal conductivity k [146, 147]. These changes can be traced in general to two physical origins: (i) Increased boundary scattering when the diameter, d, is on the order of the particle mean free path, and (ii) quantum confinement effects when d approaches the wavelength of the particles. This section provides a short review of what is currently known on this topic, while a more comprehensive review can be found in Paper IV.

5.2.1 One-dimensional nanowires (really thin)

When the length in any dimension of a solid approaches the wavelength of an electron or phonon, particles travelling in that dimension will experience quantum confinement and be severely limited in the energy state they can occupy [6]. For electrons

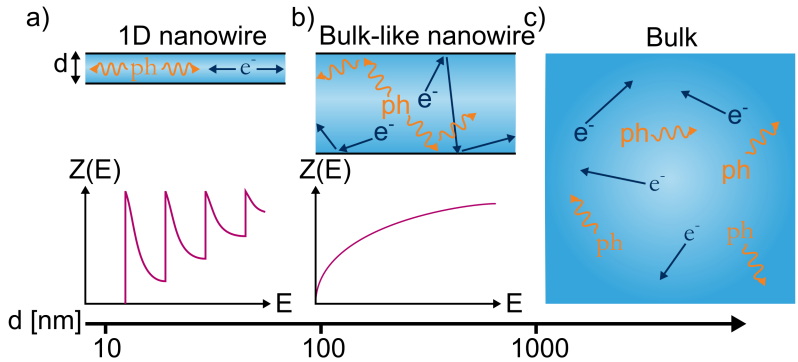

Figure 5.1: a) When the diameter, d, is around 10 nm, a nanowire can be considered to have a 1D $Z(E)$. Electron and phonon (ph) transport is directed along the nanowire axis. b) As d approaches 100 nm, $Z(E)$ takes on the 3D shape, but the dynamics of phonons and carriers may still be influenced by surface scattering effects due to the high ratio of surface area to volume. c) In a true bulk material surface scattering is a minor effect.

and holes, quantum confinement becomes notable when the confined dimension approaches the exciton Bohr radius, on the order of $1 - 10$ nm in most III-V semiconductors [148–150], for example 30 nm in InAs [151]. Phonon confinement effects become notable when the diameter approaches the phonon coherence length, on the order of 10 nm for acoustic modes [70, 152].

In a nanowire with sufficiently small d, particles experience quantum confinement along the radial direction, and thus only move freely in the axial direction. Such a nanowire is referred to as one-dimensional (1D). It has a density of states, $Z(E)$, with a high dependence on energy, see fig. 5.1(a). Particle transport is directed mainly along the axial direction in a 1D structure, where there is no confinement and thus more available states [122]. This directionality of momentum is highly desirable in a hot-carrier device. If a hot carrier has momentum in several directions, only the fraction of kinetic energy directed along the desired transport direction can be converted to power.

Phonon confinement in thin nanowires can have significant impact on hot-carrier relaxation rates [152–154], reduced rates of phonon-carrier scattering [155], promote phonon bottleneck effects [156], and suppress heat conductivity [157].

The diameter of the nanowires experimentally investigated in this work is $d \sim 50$ nm, and cannot be strictly classified as 1D. There is however no sharp boundary where a system goes from none to full quantum confinement, rather it is a gradual transition. Potentially, the momentum of generated hot-carrier may still experience some preference in directionality along the nanowire axis when $d \sim 50$ nm.

5.2.2 Bulk-like nanowires (not quite as thin)

Nanowires depicted in fig. 5.1(b) are here referred to as bulk-like. They have a d large enough ($\sim$ 100 nm) that $Z(E)$ is best described as three-dimensional (3D) but still smaller than the mean free paths of carriers or phonons (see typical length scales in table (3.1)). There is gathering evidence indicating that the increased surface scattering of phonons in such nanowires may have significant impact on the overall dynamics of hot carriers [11], as compared to a true bulk system (fig.5.1(c)).

The effects on phonon scattering in bulk-like nanowires can be observed by studying the thermal conductivity, k, since heat transport in a solid is carried mainly by acoustic phonons. There is a well established correlation of k decreasing with d, described both theoretically [146, 158–160], and observed experimentally [147, 161–169]. Many of these studies link the decrease in k with an increase in phonon boundary-scattering as d shrinks. In a similar manner, a decrease in k is also observed in nanowires when modifying boundary scattering in other ways than decreasing d, such as the introduction of super-lattice heterostructures [168], and surface roughness [166].

Increased phonon boundary-scattering may in turn affect the hot-carrier relaxation process. This is supported by experimental observations of T_{HC} increasing both with decreasing d [19], and increasing density of super-lattice structures [18]. As these observations are on nanowires with $d \sim 100$ nm, quantum confinement alone is not sufficient to explain the link. It is possible that the boundary-scattering modifies the phonon relaxation process, and consequently the hot-carrier distribution, possibly through the formation of an acoustic phonon bottleneck [18, 19]. It is also possible that the effect can be connected to a decrease in the carrier-phonon coupling strength (i.e., scattering rate), which has been observed to scale with decreasing d in ZnO [170] and ZnTe [171] nanowires.

While further work is required to fully explain the link, it appears possible to increase T_{HC} compared to bulk systems by using the nanowire geometry. This can in turn allow for a higher photovoltaic energy conversion efficiency, η_{PV}, assuming proper energy filters can be designed and realised.

5.3 Optical absorption in nanowires

As depicted in fig. 3.4, optical absorption in a hot-carrier photovoltaic device should ideally be focused into a small absorption region.

There are several ways in which the optical absorption in nanowires can be spatially modified . Because the dimensions of nanowires are on the same range as the wave-

lengths of optical light, strong resonant electromagnetic modes with intensity maxima at various positions may form in the nanowire [15–17, 172]. The location of these maxima depend on, for example, nanowire geometry, material (refractive index), and the energy (wavelength) of irradiation [173]. This effect has been used experimentally in order to control the location of generation of a hot-carrier population in single-nanowire devices similar to the ones studied in this thesis [15]. Additionally, in vertical arrays of nanowires, d and the spacing between nanowires have been used to strongly enhance light absorption in certain regions along the axial direction [174, 175].

Another method that can be used to focus optical absorption to a small region within the nanowire is to implement metallic plasmonic elements. A tiny metallic structure with a spatial gap on the order of $10 - 100$ nm couples into waves of certain wavelengths, and greatly enhances the optical field in the region around the gap [176]. Such a method has in previous work been used to generate, and study, the extraction of hot carriers within InAs nanowires [22].

5.4 Device realisation

The experiments in this thesis require the fabrication of electronic devices where current and voltage in a single nanowire can be measured under exposure to various stimulation such as electrical bias, thermal bias, and optical illumination. This section offers an overview of (i) the internal structure of the nanowires, the materials used and the resulting barriers in conduction and valence band that form energy filters, and (ii) the design and nanofabrication steps taken to fabricate devices around these nanowires.

5.4.1 Choice of material

The absorber material in a hot-carrier photovoltaic device should have a low E_g to minimise sub-band gap losses. In addition, a low k may help maintain higher temperature gradients, and, as reviewed in section (5.2.2), may be linked with increased T_{HC} in nanowires. Amongst the most common III-V materials, presented in table (5.1), InSb has both the smallest E_g and k, followed by InAs.

Unfortunately, forming good Ohmic contacts to InSb is rather challenging. This is because the Fermi level at the InSb surface typically is pinned in the valence band, resulting in the formation of Schottky barriers for electrons at metal-semiconductor interfaces [177, 178]. InSb nanowire devices have however been successfully demonstrated in a handful of cases [179, 180]. As the work in this thesis is of a more funda-

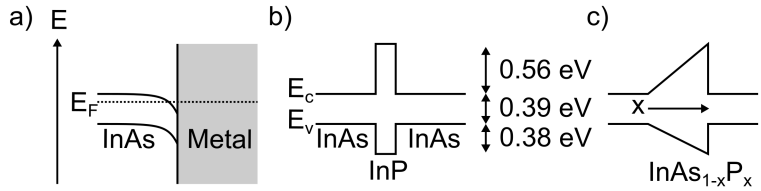

Figure 5.2: Simplified band structure, showing the valence (conduction) band edge, E_v (E_c), for three structures. a) An InAs-metal interface, where the InAs-band bends downward due to the Fermi level pinning at the surface, resulting in an Ohmic contact for electrons. b) An InAs-InP heterostructure forms a rectangular potential barrier in E_v and E_c. c) A ramp-shaped barrier formed by gradually changing the composition.

mental nature, we restrain from using InSb in order to avoid the additional complexities in device fabrication. This does not exclude the possibility that InSb could be considered in future devices once more fundamental challenges have been addressed.

The absorber material used in this thesis has instead been InAs, which still has among the smallest E_g and k. An additional advantage working with InAs is that it naturally forms Ohmic contacts at metal-semiconductor interfaces. This is because the Fermi level at InAs surfaces is pinned in the conduction band (fig. 5.2 (a)) [182]. Electrons travel unhindered across the contact, while holes face a Schottky barrier which may hinder them from being extracted [183]. As long as transport is dominated by electrons, this will not be a noticeable effect, but it may have an impact when generating additional electron-hole pairs, as observed for InAs nanowires without heterostructures in the SI's of Papers I and II.

Energy filters in this work are realised by introducing short InP segments in the InAs nanowire, where the conduction (valence) band offset compared to InAs is 0.56 (0.38) eV [184]. In this way, as in Papers I and II, a rectangular potential barrier can be formed both in the conduction and valence band, as shown in fig. 5.2(b). Paper III studies a ramp-shaped barrier realised by gradually changing the composition from InAs to $InAs_{1-x}P_x$, and then abruptly back to InAs, as in fig. 5.2(c).

Table 5.1: Band gap, E_g, thermal conductivity, k, and ratio between hole, m_h^*, and electron, m_e^*, effective mass for some of the most common III-V semiconductors [181]. The values for m_h^* used here are from the heavy hole band, as this is the band with the largest density of states around the band edge.

Material	GaP	GaAs	GaSb	InP	InAs	InSb	Si
E_g [eV]	2.26	1.42	0.73	1.34	0.35	0.17	1.12
k [$\mathrm{Wcm^{-1}\,^{\circ}C^{-1}}$]	1.1	0.55	0.32	0.68	0.27	0.18	1.3
m_h^*/m_e^*	2.6	6.7	5.7	12.6	17.8	28.6	2.3

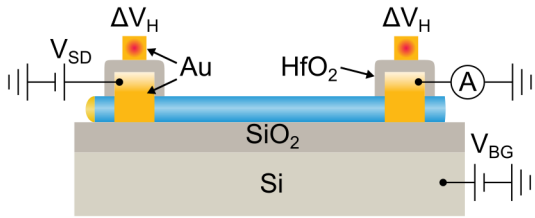

Figure 5.3: Overview of device design. A single nanowire is deposited on top of an electrically insulated Si substrate under which a backgate voltage V_{BG} can be applied. Metalic contacts to the nanowire allow for the application of a voltage bias, V_{SD}. In Paper III metal leads, so called top heaters, are deposited on top of the source-drain contacts, electrically insulated by HfO_2. The application of a voltage, ΔV_H, to the top heaters leads to Joule heating.

5.4.2 Design and processing

Fig. 5.3 shows the general design of the single-nanowire devices used in the experiments of Papers I-III. Individual nanowires are horizontally deposited on electrically insulated Si substrates that allow for the application of a global back gate voltage, V_{BG}. Metallic leads are contacted to the nanowire to facilitate voltage biasing. In the case of Paper III, additional electrically insulated metal leads are fabricated on top of the contacts to apply a thermal bias, ΔV_H. This section provides a summary of the fabrication techniques used. They are not unique and more details can be found for example in Ref. [185] and [186].

5.4.2.1 Substrates

Single nanowires are mechanically transferred onto the substrate from a growth-chip containing numerous nanowires as grown. The substrate consist of a heavily p-doped Si wafer, with a 117 nm thick layer of thermally grown SiO_2 on top for electrical insulation between nanowire and substrate.

The substrate contains pre-defined gold patterns with a number of fields where the nanowire may be deposited for contacting (fig. 5.4(a,b)). Each such field contains a number of designated larger metallic leads, as well as a coordinate grid on top of which the nanowire is deposited. Two designs are used for the substrate. The 4-lead designs are sufficient for devices where only source and drain contact to the nanowire is necessary, as in Papers I and II. The more complex devices in Paper III include contacts for applying a thermal bias, and are fabricated using the 12-lead design.

After depositing a nanowire in one of the fields, the nanowire is imaged by scanning electron microscope in order to determine its location and orientation on the coordinate grid (inset fig. 5.4(c,d)). This information is needed to high accuracy, as it is

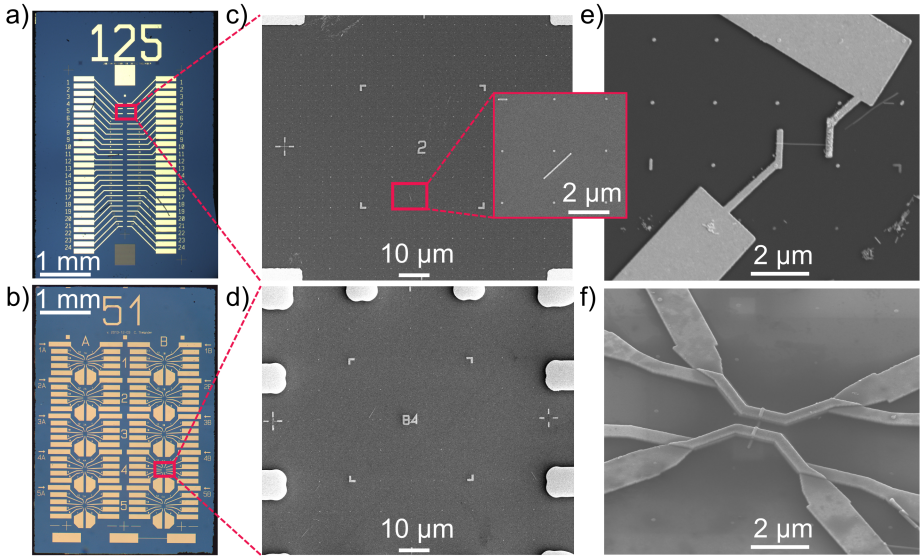

Figure 5.4: a,b) Optical and c-f) scanning electron microscope images of substrate and device. Top row shows the 4-lead per write filed design used to contact nanowires in Papers I and II. Bottom row shows the 12-lead per write field design used to contact wires for Paper III including top heaters.

used to design the lithography-pattern for the device.

5.4.2.2 Contacting

Contacting the nanowire to the predefined leads in each field is done using electron beam lithography in the following steps:

1) Liquid polymer PMMA (type 950 A5) is deposited on top of the substrate by spin coating at 5000 RPM for 60 seconds, and subsequently baked at 180 °C for 3 minutes. This results in a roughly 300 nm thick layer of hardened polymer covering the substrate.

2) For each field with a nanowire, the corresponding design pattern is written in the resist by electron beam lithography. PMMA is a positive resist, meaning when it is exposed to an electron beam the polymer chains break, making them more soluble.

3) The exposed resist is removed by submerging the sample in solvent solution consisting of methyl isobutyl ketone (MIBK) and isopropanol (IPA) in a concentration MIBK:IPA = 1:3 for 40 seconds.

4) To ensure all resist is removed from the exposed regions, the sample is ashed by an oxygen plasma at 5 mbar for 30 seconds. The ashing step is not a selective process and

it removes resist across the whole sample, wherefore one has to be careful in not doing it for too long or else the exposed pattern will vanish. By performing this step with the sample shielded under a small Faraday cage, the ashing rate is slowed so that only a couple of nanometers of resist is removed.

5) When contacts to the nanowire are made, a step of etching and surface passivation is included in order to remove native oxides and contaminants from the InAs surface. This step is necessary to ensure good, Ohmic contact at the metal-semiconductor interface. The passivation technique used here is by submerging the sample in an ammonium polysulfide, $(NH_4)_2S_x$, water solution. This is a well-proven technique for the passivation of InAs nanowires [186].

6) Metal is evaporated on top of the sample in a high-vacuum environment. Au is the contact metal of choice, but it does not adhere to InAs very well, and for this reason a thin layer of Ni is first deposited. Typically a 25 nm layer of Ni is deposited followed by a 75 nm layer of Au, for a total contact thickness of 100 nm.

7) After metal is deposited on the whole sample, all the resist in the non-exposed regions, along with any metal on top of it, are washed away by submerging the sample in acetone at 50 °C for approximately 20 minutes. This leaves only the metal in the lithographically defined regions (steps 2 and 3).

8) A final step of ashing for 60s is performed in order to remove any resist residue from the surface. An example of a complete device can be seen in fig. 5.4(d).

In Paper III, some additional steps are required in order to fabricate top heaters. These are fabricated on top of, but electrically insulated from, the electrical contacts. The following additional steps are taken, further detailed in Ref. [187]:

9) An insulating hafnium oxide,HfO_2, layer is deposited by atomic layer deposition over the entire sample surface. The deposition is done with Tetrakis (dimethylamino) hafnium(IV) (TDMAH), for 80 cycles at 100 °C, resulting in a thickness of roughly 8 nm.

10) The entire surface of the chip is now coated in an electrically-insulating oxide layer. It is therefore necessary to open windows in the oxide so that top heaters can be connected to the predefined gold pads. The window is opened by focused ion-beam milling at the predefined metallic leads where the heaters will make electrical contact.

11) Steps 1-8 are repeated but with the design for the top heaters. A complete device with top heaters is shown in fig. 5.4(f).

6. Experiments on carrier extraction in nanowires

This chapter summarises the experimental work done in Papers I-III in two parts.

The first part presents the studies of Papers I and II, spatially resolving hot-carrier extraction in single nanowires by exciting hot carriers via either an electron or optical beam. The nanowires contain a rectangular potential barrier, epitaxially defined, as energy selective filter. Current generation from hot-carrier extraction is observed, and the results provide confirmation and further knowledge about the mechanism of hot-carrier extraction in such systems.

The second part summarises the work in Paper III. It is investigated whether the shape of an energy filter can be used to tune the fill factor and power of a thermoelectric device while operating in a nonlinear transport regime. The thermoelectric response of a ramp-shaped, heterostructure, defined within a nanowire, is observed under temperature gradients in either direction along the nanowire. The experiments are further compared to a transport model based on the Landauer-Büttiker scattering theory. It is also observed that the asymmetric shape of the potential barrier may be used for thermoelectric rectification.

6.1 Spatially resolving hot-carrier extraction in single nanowires

Current generation from optically excited hot-carrier extraction has previously been observed in InAs nanowires with epitaxially defined InP heterostructures under global illumination [15, 21, 22]. The mechanism envisioned to explain the current generation in these devices is depicted in fig. 6.1. The rectangular barriers result in step-shaped (eq. (4.15)) transmission functions, $\mathcal{T}(E)$, for electrons (holes) in the conduction (valence) band. A more detailed image of the bandstructure is found in fig. (5.2).

Because of the high ratio m_h^*/m_e^* in InAs (see table (5.1), a majority of the excess kinetic energy during excitation goes towards the hot electron. Thus electrons are more likely to make it over the barrier, while the less energetic holes are reflected. If excitation of a hot-carrier population can be focused to one side of the barrier, a current may be generated from the extraction of hot electrons.

Limpert et al. [21] exposed such nanowires to global illumination, and directed the absorption to one side of the barrier by utilising naturally occurring wave mode maxima within the nanowire. During these measurements an open-circuit voltage, V_{OC}, in excess of the Shockley-Queisser limit for InAs was observed. Such an observation is a strong indication of hot-carrier extraction, since it is not possible in conventional single pn-junction solar cells, as discussed in section (4.1.1).

Chen et al. [22] instead locally enhanced the absorption on one side of the barrier by employing lithographically designed metallic segments in the vicinity of the barrier, so called plasmonic antennas [188]. These observations further supported the hot-carrier extraction interpretation by demonstrating the presence of both thermionic transmission and internal photoemission in the device. When illuminated by energies larger than ~ 1 eV (the distance from InAs valence band to InP conduction band), a linear dependence between photocurrent and intensity was observed, as expected for internal photoemission. For excitation energies below ~ 1 eV the measured current was at least one order of magnitude smaller and the dependence on intensity was polynomial, as expected for thermionic emission.

The fact that these studies globally illuminate the nanowires means that it cannot be determined with certainty where in the device current generation is taking place. It is possible the current originates from hot-carrier extraction at other locations in the device than the heterostructure defined in the nanowire. For example, photocurrent generation has previously been observed to originate around the semiconductor-metal contact interface in devices with single nanowires of GaAs [189], Si [190], and VO_2 [191]. Those observations were explained as photothermoelectric (heating of the metal contact), or a as result of band bending at the contact interface, i.e. Schottky contacts. Resolving current generation in the nanowire as a function of excitation location could determine the role of the InP segment in current generation.

Knowledge on the relation between the location of excitation and power produced in a hot-carrier photovoltaic device would provide input for future improvement of their design. For example, experimentally determining the effective hot-carrier diffusion lengths, L_{HC}^*, which are difficult to theoretically predict (see section (4.3)). It would be difficult to perform such a study using the above mentioned techniques for focusing of absorption. The fabrication of plasmonic antennas around single nanowires is a time-consuming process that requires careful alignment of the plasmonic elements,

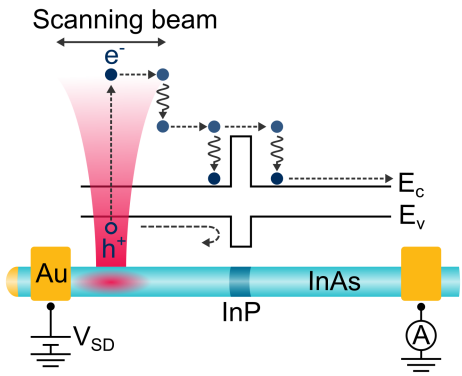

Figure 6.1: Conceptual sketch of the scanning-beam induced current measurement approach used to study single nanowire devices in Papers I and II, indicating composition and band structure of the nanowires used, and the mechanism of charge carrier separation via hot-electron extraction.

resulting in a low yield. The approach of utilising internal absorption hot spots is also hard to control as their location will depend on factors such as the geometry of both nanowire and metallic contacts, as well as the illumination wavelength [15]. A more direct way of studying hot-carrier extraction as a function of excitation location is for these reasons highly desirable.

To address these issues, Papers I and II apply two types of scanning beam induced current methods, as depicted in fig. 6.1, to spatially resolve hot-carrier extraction in similar single nanowire devices. In Paper I a beam of electrons accelerated by a high electric field is used, while Paper II employs a highly focused optical beam. Both papers study nanowires from the same growth, InAs nanowires with a diameter of around 50 nm and a 25 nm long InP heterostructure segment around the center in axial direction, the same type of structure as Ref. [21, 22].

As the source of excitation scans along the sample, the current generated in the device is mapped as a function of excitation location. If the source of excitation is close enough to the barrier, the hot electron is able to diffuse over the barrier before it loses too much energy. As the source moves further away it becomes exponentially less likely for the electron to make it (see section (4.3)).

Effective hot-electron diffusion lengths, L_e^*, are extracted from both studies by adapting a model to the results. The initial spatial distribution of the hot electrons is described by a generation density, $G(z, z_0)$, where the z-coordinate indicates distance along the nanowire axial direction, and z_0 the position of the excitation source. A qualitative expression for the current generated is then given by

$$I(z_0) \sim \left[\int_{\text{left contact}}^{\text{barrier}} G(z, z_0) e^{-z/L_e^*} dz - \int_{\text{barrier}}^{\text{right contact}} G(z, z_0) e^{z/L_e^*} dz \right]. \quad (6.1)$$

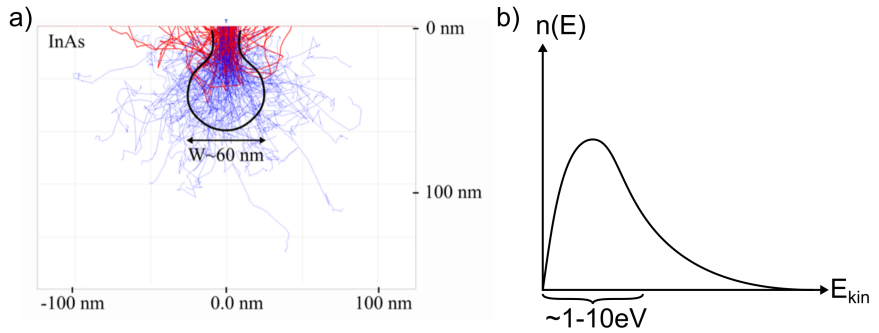

Figure 6.2: a) Monte Carlo simulation of electron path calculated with CASINO software b) Approximate distribution of the deposited energy as a function of carrier density, a majority of the excited electrons are found within a few eV above the band edge [192]. a) adapted from the supplemental material of Paper I.

This model assumes that the transport is dominated by hot electrons, neglecting holes. This is partially justified by the fact that hot electrons are the main carrier type extracted over the barrier. Electrons are also the majority charge carriers because the InAs nanowires are n-type conductors with the chemical potential pinned in the conduction band. Ohmic contacts for the electrons at the metal-semiconductor interface makes sure electrons are easily extracted to the circuit. The results from Papers I and II are now presented individually followed by a comparison of the two.

6.1.1 Electron beam induced current (Paper I)

The diffraction limit puts a theoretical minimum to the width a beam of wavelike particles can be focused as half of its wavelength. This severely limits the resolution that can be achieved using optical illumination, where the wavelenghts are typically $\sim 500-1000$ nm or larger. In Paper I this limitation is circumvented by employing a beam of highly accelerated electrons. The wavelength of the electrons is small enough to not be limiting to the spatial resolution. Electron-beam induced current (EBIC) measurements have for this reason been used rather extensively to study current generation in nanowires, but so far not with a focus on hot carriers [193–198].

In EBIC, a beam of highly energetic electrons is used to excite secondary electron-hole pairs via a cascade of inelastic scattering events [192, 199, 200]. As the energetic electrons hit the sample, they will scatter at numerous occasions with atoms in the lattice, each collision giving away some E_{kin} that can excite an electron-hole pair. Once excited, these carriers can be considered hot carriers similarly as if they were optically excited: they have received an increase in E_{kin}, and are initially not in equilibrium with the lattice temperature. Depending on the acceleration voltage of the electron-beam, a single energetic electron can excite 1000s of such hot carriers [201].

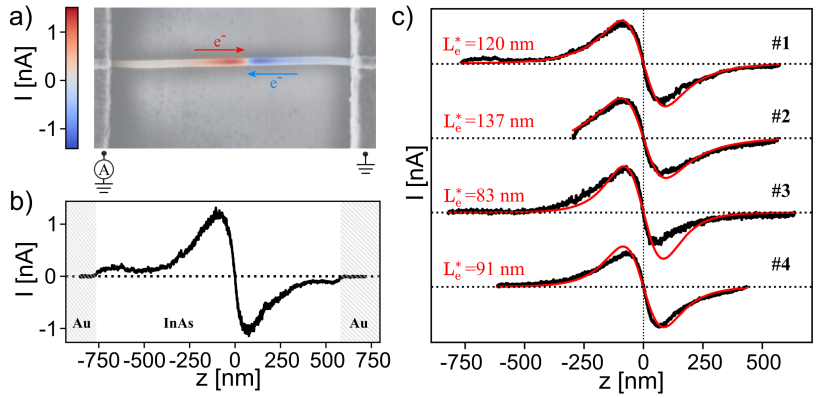

Figure 6.3: a) Overlay of EBIC measurement (red and blue color) on top of a scanning electron microscope image, arrows indicate direction of electron net flow, for scale see (b). b) linecut of EBIC along the nanowire axis. c) adapted model (red line) to EBIC measurements on four samples. Adapted from Paper I.

Since secondary electrons scatter in all directions, the excitation volume may be significantly larger than the initial spot-size of the beam. Fig. 6.2(a) shows how electrons spread through InAs, based on Monte-Carlo calculation (using the CASINO software [202]) for parameters similar to the presented experiment. Even though the excitation volume is larger than the initial spot-size, we see that 95% of all energy is deposited within a diameter of roughly 60 nm, close to the diameter of the nanowires used.

It is assumed that the density of hot electrons along the nanowire axis, z, is spatially distributed as a Gaussian distribution

$$G_e(z, z_0) = e^{-\frac{(z-z_0)^2}{2w^2}}. \tag{6.2}$$

As for the distribution of energy among the secondary electrons, it is generally expected to have a shape similar to fig. 6.2(b). A smooth, polynomial increase in the density of electrons, $n(E)$, the closer one gets to the band edge () [192]. In other words, despite the high energy of the electron beam, the majority of secondary (hot) electrons will still be found within a few eV of the conduction band, a similar range to optically excited hot carriers.

Fig. 6.3(a) shows the measured EBIC. The image is an overlap of a scanning electron microscope image and the EBIC scan, which are done simultaneously. Red (blue) color indicates positive (negative) current through the device, arrows indicate the direction of electron transport. A swap in polarity of the current is seen around the center of the nanowire, where the InP segment is expected to be. We conclude that the potential barrier is located at this point, defined as $z = 0$ in fig. 6.3(b). Note also that the current recorded is roughly two orders of magnitude larger than the beam of

primary electrons, assuring that the detected current is indeed from excited secondary electrons.

The sign of the current tells us that the net electron flow is always directed towards the barrier no matter on which side excitation takes place. This is interpreted as more electrons than holes being extracted over the barrier, as depicted in fig. 6.1. Electrons and holes not making it over the barrier will recombine without contributing to generating a current, only when a separation of electrons and holes take place is a current generated.

Further supporting this conclusion is the observation of an exponential decay in current as the excitation source moves further away from the barrier. This is interpreted as the hot electrons being exponentially less likely to be transmitted the further away from the barrier they are excited. A value of $L_e^* = 110$ (± 30) nm is determined by adapting eq. (6.1) to the line-profile of EBIC along the nanowire axial direction, as shown for several measurements in fig. 6.3(c). The relaxation length estimated here appears reasonable as it is within the same range as the estimates in table (3.1). It is naturally expected that L_e^* will vary depending on the excitation conditions. The excitation with an electron beam in Paper I might not represent realistic conditions for a photovoltaic device. The value of L_e^* found in Paper I should thus only be seen as a rough guideline, and it will later (section (6.1.3)) be compared to that extracted from Paper II under optical excitation.

Paper I concludes that the previously observed current generation in these type of nanowires does indeed originate from the separation of charge carriers centered around the InP heterostructure, consistent with the mechanism depicted in fig. 6.1. Exposure of the metallic contacts does not generate any current (fig. 6.3(b)), and no significant current appears to be generated around the semiconductor-metal interface. If the EBIC was a result of some form of potential barrier at the metal-semiconductor interface, we would expect the opposite polarity in current as that observed here, as observed in the supplemental material of Paper I. The possibility of a Schottky barrier being responsible for electron-hole separation can thus be ruled out.

The electron-beam does however not represent realistic excitation conditions for a hot-carrier photovoltaic device. The performance in terms of power production must be evaluated under optical excitation. Under optical excitation, plasmonic effects or other forms of interference could still be present that are not seen during the OBIC. What EBIC gains in spatial resolution, it lacks in spectral resolution. In other words, it lacks in control of the energy of excited hot carriers, making it challenging to perform studies on the energy-dependence of hot-carrier extraction. The results of Paper I will guide the interpretation of Paper II, where spatial resolution is limited.

6.1.2 Optical beam induced current (Paper II)

Optical beam induced current (OBIC) measurements, also known as scanning photocurrent microscopy, is a widely applied technique in studying photothermoelectric effects in micrometer scale devices such as graphene [203–211] and various other 2D materials [212–214]. It has been applied in some extent to study the photoresponse in nanowires from materials such as VO_2 [191], GaAs [189], InAs [215, 216], PbS [183] and GaN [217] but without any internal axial heterostructures. Likely due to the fact that these heterostructures are on much smaller length scales than can be spatially resolved with OBIC.

Paper II applies OBIC to study nanowires from the same growth as Paper I. Because the results are qualitatively similar to the EBIC measurements, the results in Paper II can be well understood even with its limited spatial resolution. In addition, performance parameters of interest for hot-carrier photovoltaic devices such as open-circuit voltage (V_{oc}), short-circuit current (I_{sc}), and power (P), are extracted as a function of excitation location, energy and power.

The experimental setup is relatively simple, cheap, and easy to modify. It is based on a modified atomic force microscopy setup where the device is electrically connected, and mounted on a stage which is moved with piezo-electric engines. A laser diode is focused on the stage by a single optical lens, and the stage moves while the laser is fixed. Results with two different excitation wavelengths are presented, a 785 nm (1.58 eV) laser focused to a spot-size of roughly 500 nm, and a 1310 nm (0.95 eV) focused to roughly 1000 nm spot-size. All measurements are done at room temperature in an open-air environment, resembling the operational conditions of a normal photovoltaic device. Because the optical microscope cannot resolve the nanowire device, previously-taken scanning electron microscopy images are necessary to indicate the device orientation (inset fig. 6.4(a)).

The OBIC results of fig. 6.4(a) closely resemble those seen with EBIC in Paper I, but with a lower spatial resolution. Two regions with current of opposite polarity are seen. The direction of current flow and general shape of the line-profile along the nanowire (fig. 6.4(b)) is the same as observed in Paper I. The mechanism for hot-carrier extraction depicted in fig. 6.1 thus appears to be consistent also under optical excitation. Just as in Paper I, it is assumed that the potential barrier (InP segment) is located at the point where the current swaps polarity (at $z = 0$ in fig. 6.4(b)).

The experimental data are well adapted with eq. (6.1) when $L_e^* = 280(\pm 30)$ nm (fig. 6.4(b)). The value differs somewhat from that observed in Paper I, but is on the same order of magnitude as expected from table (3.1). The values are further compared in section (6.1.3). The optical generation density, $G(z, z_0)$, was here determined by

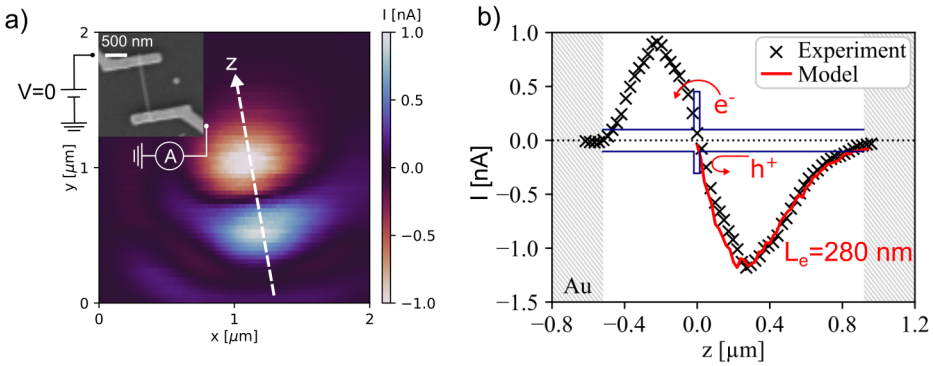

Figure 6.4: a) OBIC scan with λ = 785 nm, scanning electron microscope iamge in inset shows the orientation of device, and white dashed line the expected location of nanowire. b) Linecut of OBIC along white dashed line in (a), along with adapted model (red solid line) from which $L_e^* = 280\ (\pm 30)$ nm is extracted. Band structure and expected directions of electron/hole transport is indicated. Adapted from Paper II.

solving the Maxwell wave equations in a 3D optical model with the finite element method, see supplemental material in Paper II. It is possible that mathematical post-treatment of the data in fig. 6.4 to account for the shape of the optical beam, i.e. deconvolution [218], could further enhance the resolution. Such treatment has not been done. It is however not clear that such treatment would affect the extracted value for L_e^*, which is already smaller than the beam spot.

Current-voltage characterisation (fig. 6.5(a)) with the optical beam fixed at the points of maximum and minimum current in fig. 6.4 demonstrate that the device is indeed capable of power-generation. At the point of maximum current, z_{max}, $I_{SC} = 2.2$ nA, $V_{OC} = 80$ mV, and the maximum power $P_{max} = 58$ pW. This V_{OC} is still below the Schockley-Queisser limit. Worth noting is that the points chosen to gather this data (z_{max} and z_{min}) are the points that give the highest current, not necessarily the points that maximise voltage or power. A more systematic study with current-voltage curves at several points along the nanowire would provide further valuable information here.

An OBIC measurement with near-infrared wavelengths of 1310 nm (0.95 eV) is shown in fig. 6.5(b,c)). The results are qualitatively consistent with the previously reported results, indicating the applicability of the technique across illumination wavelengths. The larger spot-size on the order of 1 µm results in a reduced spatial resolution. The excitation energy is right at the threshold of directly exciting an electron from the valance band to the conduction band and above the barrier. Therefore, a lower portion of electrons are expected to be extracted, and the smaller current response (accompanied by higher sensitivity to noise) is expected. Even at this low current, it is possible to study the dependence of current generation and the irradiance

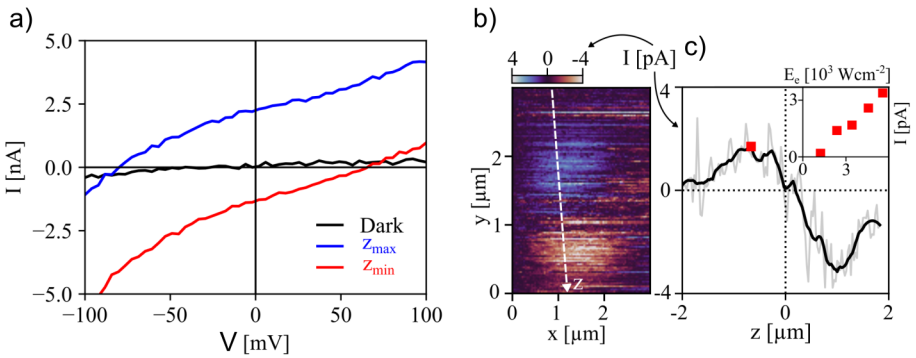

Figure 6.5: a) Current-voltage curves collected with the optical beam fixed at the two points in fig 6.4(a) that yield the maximum and minimum current respectively, as well as with beam turned off. b) OBIC scan of similar device with λ = 1310 nm, and c) corresponding linecut with the maxima as a function of laser power in inset. Adapted from Paper II.

of the excitation source (inset fig. 6.5(c)).

The results of Paper II demonstrates the devices ability to produce power from hot-carrier extraction at various points of excitation. They are consistent with previously proposed mechanisms. Guided by EBIC measurements, OBIC allows for the systematic study of performance parameters such as power production and hot-carrier diffusion lengths as a function of excitation energy, irradiance and location. Additionally, OBIC is a very accessible tool that can be assembled in basically any lab environment and sued with a relatively high throughput so that different types of devices can be studied and compared. It can also be combined with various scanning probe measurements such as scanning gate and atomic force microscopy, as recently demonstrated on nanowires from the same growth as in Papers I and II in Ref. [219].

6.1.3 Comparison of EBIC and OBIC

The EBIC measurements of Paper I are here compared with those of OBIC collected at 785 nm illumination in Paper II, see fig. 6.6. While qualitatively similar, there are several quantitative points to compare between the results of Papers I and II.

The L_e^* extracted with OBIC (280 nm) is roughly three times higher than that of EBIC (110 nm), highlighting the large role the nature of the excitation will have on the dynamics of hot carriers. Since the samples are close to identical, the hot-carrier distribution is likely the largest difference between the two cases. This goes to show that in the end, a hot-carrier photovoltaic system may need to be optimised for certain excitation conditions. The extracted values for L_e^* does however provide a valuable ball-park number around a few 100 nm that should be consider when further

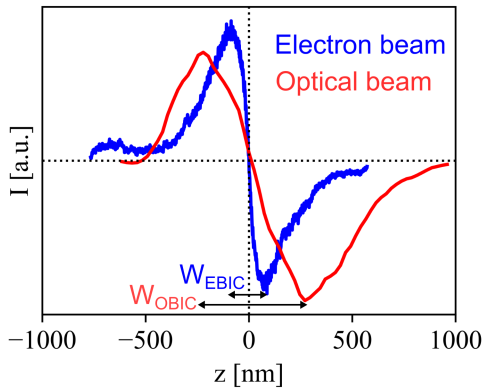

Figure 6.6: Comparison of EBIC data from fig. 6.3(b) and OBIC data from fig. 6.4(b). Adapted from Papers I and II.

developing the design of hot-carrier photovoltaic devices.

The difference in spatial resolution between the two methods is clearly seen by comparing the separation, W, between the maxima and minima. For the OBIC measurement $W_{\mathrm{OBIC}} \sim 500$ nm, while for the EBIC $W_{\mathrm{EBIC}} \sim 100$ nm. Both values are similar to the experimental spot-sizes used in the corresponding experiments. This tell us that the extreme points in current production occur roughly when the beam is entirely on one side of, but as close as possible to, the barrier. When the beam is e.g., right above the barrier, at $z = 0$, no current is generated since just as many hot carriers are generated on either side of the barrier.

An intriguing result is that the currents recorded in both experiments are of very similar magnitude, roughly 1 nA. We have not yet been able to determine whether this is a coincidence or if there is a physical explanation. In the OBIC measurements with 1310 nm, a significantly smaller current on the order of a few pA is recorded. One possible explanation for this could be that the number of free electrons available in the nanowire is small enough that there is a point where they are all excited. That would lead to a saturation in current as further increase of irradiance past that point would not result in generation of more electron-hole pairs.

Combined, the EBIC and OBIC techniques provides both high spatial and spectral resolution. Both types of measurements can be done at a relatively high throughput on the same device. The methods presented here could thus be used to experimentally, systematically, assess and compare the performance of hot-carrier extraction through various energy-filtering designs.

6.2 Thermoelectric, nonlinear transport in an asymmetric barrier (Paper III)

The high temperature and voltage differences over short distances in a hot-carrier photovoltaic device, as well as a nanoscale thermoelectric device, means their nonlinear transport properties must be considered. Operating thermoelectric devices in a nonlinear regime can lead to novel functionalities such as thermoelectric rectification, suggested in theory [220–222] but rarely realised in practice [24]. Conventional solar cells are already operated in a nonlinear regime, a fact that allows for the tuning of parameters such as the FF in order to maximise power production [223]. Under linear response, as in the conventional thermoelectric, the fill factor is always 0.25 by definition (see section (4.2.4)).

In Paper III, the thermoelectric transport in a nonlinear transport regime of an asymmetric barrier is studied with two questions in mind: (i) Could such a structure allow for thermoelectric rectification? (ii) Can the shape of the barrier be used in order to alter the shape of the current-voltage curve in order to improve the fill factor, and thereby power?

The high degree of control in nanowire growth has enabled the synthesis of a rather unique, epitaxially defined, ramp-shaped potential barrier (fig. 6.7(a)). The composition is gradually changed from InAs to $InAs_{0.35}P_{0.65}$ and then abrubtly back to InAs. The ramp-shaped potential has a length of $L = 92$ (± 7) nm and a height $U_{\text{top}} = 340$ (± 4) meV.

A temperature gradient, ΔT, can be induced in either direction along the nanowire via top-heaters [187] positioned at each end of the nanowire (fig. 6.7(a)). The top heaters are placed on top of, but electrically insulated from, the metal contacts on both the gradient (G) and steep (S) side of the barrier. By applying a voltage, ΔV_H, across a top-heater, a current is driven that will generate Joule heat. This heat is thermally conducted via the metallic contacts to the nanowire. Current-voltage characterisation of the device is done by applying a voltage, V_{SD}, via the source-drain contacts. A scanning electron microscope image of a completed device is shown in fig. 6.7(b).

The results are theoretically interpreted using the Landauer-Büttiker scattering theory (eq. (4.9)). To find the transmission probability, $\mathcal{T}(E)$, the Schrödinger equation (eq. (2.2)) is fully solved for a ramp-shaped potential barrier. The expression is rather lengthy and can be found in the supplemental material of Paper III, it is however similar to the Fowler-Nordheim expression [224].

The current-voltage curves collected under various thermal bias configurations can be seen in fig. 6.8(a). Black solid lines shows adaptation of model to the experimental

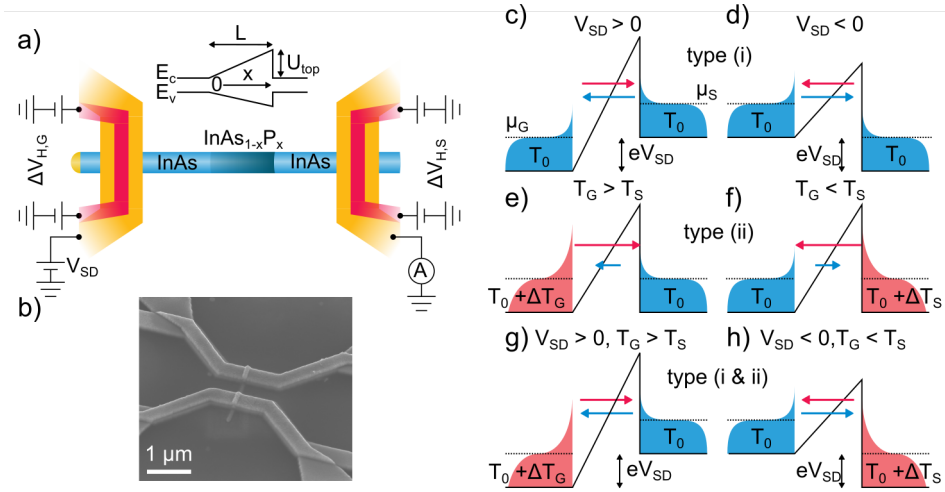

Figure 6.7: a) Device layout with band structure of the nanowire. b) Scanning electron microscope image of the device. c-h) Modification of conduction band and Fermi distributions under (c,d) electrical bias, (e,f) thermal bias, and (g,h) electrical and thermal biases. The length of arrows indicate relative size of electron transport. Adapted from Paper III.

results , a good fit is only found when transport is occurring in a tunneling regime where $\mu_0 \ll U_{top}$. The fit gives a relation between ΔV_H and ΔT as shown in the inset of fig. 6.8(a).

When $\Delta T = 0$, the current depends nonlinearly on V_{SD} as soon as V_{SD} is larger than a few meV, as expected from the type (i) nonlinearity depicted in fig. 6.7(c,d). The difference in $\mathcal{T}(E)$ in fig. 6.7(c) and fig. 6.7(d) results in an asymmetric shape of the current-voltage curve with regards to the sign of V_{SD}. Increase of $\Delta V_{H,G}$ ($\Delta V_{H,S}$) results in the curves shifting downward (upward), as an increasing additional thermal current is generated.

Nonlinear response originating from thermal bias, type (ii) in fig. 6.7(e,f), can be isolated and observed by studying the dependence between I_{SC} and ΔT in fig. 6.8(b). This nonlinearity originates from the change in the energy range of electrons that participate in transport. In other words, the difference in Fermi-Dirac distributions on the two sides, combined with the strong energy dependence in $\mathcal{T}(E)$. Because $\mathcal{T}(E)$ remains unchanged, there is no asymmetry in I_{SC} with regards to which side of the barrier is heated. The fact that I_{SC} is symmetric is an important confirmation that the two top heaters result in the same ΔT for a certain applied ΔV_{H}.

When the device is operated in a power producing regime, nonlinear effects of both type (i) and (ii) (see fig. 6.7(g,h)) can be expected. An asymmetry in maximum output power is seen, fig. 6.8(d), when comparing heating on the gradient and steep side. Heating on the steep side is seen to result in a close to two-fold increase in

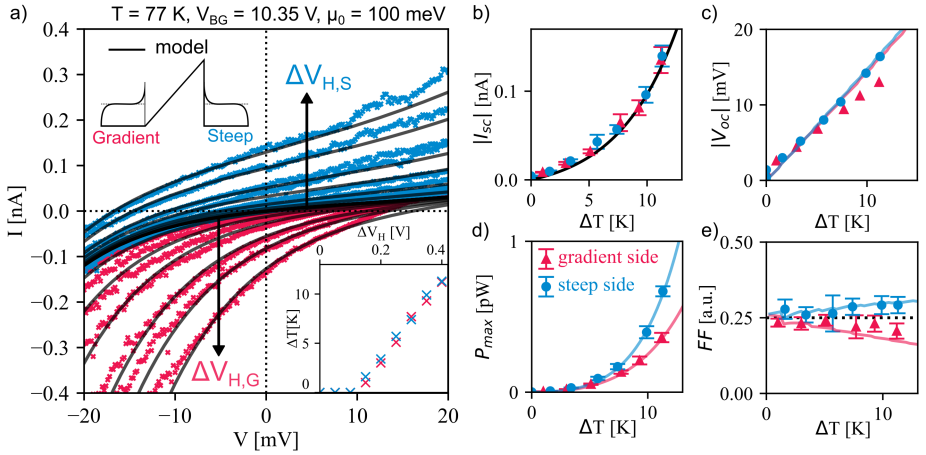

Figure 6.8: a) Current-voltage curves collected under various thermal voltages (red and blue data points), black lines indicate adaption of model, inset shows the adapted temperature gradient against heating voltage. b-e) short-circuit current, open circuit voltage, maximum power, and fill-factor, respectively, as functions of the temperature gradient. Points indicate experiment and solid lines model. Adapted from Paper III.

P_{max} compared to the other side. The only possible source of this asymmetry is the asymmetric change in $\mathcal{T}(E, V_{SD})$ with respect to the sign of V_{SD}. This demonstrates that an asymmetrically shaped barrier could be used to realise a thermoelectric rectifier.

The perhaps most noteworthy result is that the shape of the current-voltage curves, characterised by FF, is modified asymmetrically in the two heating configurations (fig. 6.8(e)). Starting at the linear response value of $FF = 0.25$, the value steadily increases (decreases) with ΔT when heating on the steep (gradient) side. This tells us that the $\mathcal{T}(E)$ of a barrier with the shape of fig. 6.7(f) results in a $FF > 0.25$ and corresponding increase in P_{max}, while a shape as fig. 6.7(e) results in a $FF < 0.25$. In the nonlinear regime investigated here, the shape of the barrier can thus be used to tune the FF of a thermoelectric system and increase it beyond the linear response limit.

Since non-linear current response is seen both under the application of electrical and thermal biases, it is surprising that the V_{OC} appears to have a linear response (fig. 6.8(c)). We are unable to pinpoint an explanation for this. It could be that it only appears linear within the temperature range probed here, or that the response is linear by coincidence at this specific point. In this linear response regime, an experimental Seebeck coefficient of 1.5 mV/K is extracted. Without the introduction of a heterostructure, n-type InAs typically has values on the order of $S = 0.1$ mV/K [225, 226].

The findings of Paper III represent a new path towards optimising the power pro-

duction in thermoelectric devices, and possibly hot-carrier photovoltaic devices. It also introduces a system where the thermoelectric current is clearly stronger in one direction than the other, similar to a thermoelectric rectifier. The triangular shape used here is only the most simple example of an asymmetric shape, and many others could be imagined. The combination of experiment and modelling in this paper can be expanded to guide the design of energy filters for carrier extraction and power production.

7. Outlook

Proof-of-principle hot-carrier photovoltaic devices have been realised in single nanowires [21, 22, 227, 228]. The main question moving forward is how they can be designed in order to increase the performance in terms of output power and efficiency. Several concrete steps are now identified towards experimentally identifying the type of heterostructure that can be realised in practice and yield the highest efficiency at maximum power production.

Paper III identifies asymmetry of the heterostructure as a new parameter that could potentially be used to tune the fill factor and power production, as long as the transport occurs in a nonlinear regime. It remains to be investigated whether this is also the case when transport occurs above the barrier. Other types of asymmetric shapes than the ramp-like one used here could be investigated. The theoretical work in Paper III could be expanded to identify candidate shapes worth experimentally investigating, both symmetric and asymmetric.

Theoretically, the box-shaped transmission type has been predicted to offer the highest efficiency at maximum power production [123]. An intriguing challenge is to experimentally realise an energy filter with such a transmission function. It has been predicted that this should be possible with a series of quantum dots [123]. Epitaxially defined quantum dots [229], superlattices [230], and multiple quantum wells [231] of high quality are regularly realised in the axial growth direction of nanowires. The realisation of serial quantum dots in a nanowire, in order to tailor a box-like transmission function, seems like a feasible challenge.

A hot-carrier solar cell should ideally have two energy filters, one for hot electrons and holes respectively, as depicted in fig. 7.1(a). In this way, hot carriers are prevented from diffusing in the wrong direction and a higher η_{PV} compared to the single barrier devices used in Papers I-III should be possible. Confinement effects between the two barriers might also lead to secondary positive effects such as the increased density of hot carriers resulting in higher effective hot-carrier temperatures. To the author's

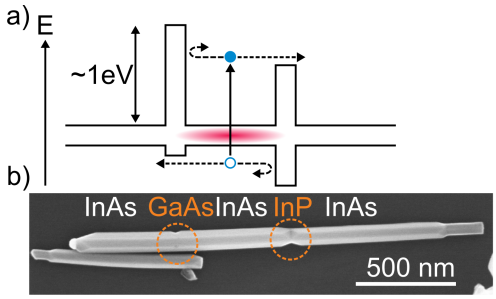

Figure 7.1: a) Band structure and b) scanning electron microscope image of a nanowire with an InAs/InP/GaAs "double-barrier" heterostructure. The barriers introduce carrier- and energy selectivity, extracting hot holes and electrons in opposite directions after optical excitation.

knowledge, a hot-carrier photovoltaic device has not yet been demonstrated with two energy filters specifically dedicated to extraction of hot electrons and holes respectively, presenting an intriguing challenge. Work is in fact ongoing towards realising such a structure inside InAs nanowires, using InP and GaAs heterostructures to realise two different rectangular potential barriers (see fig. 7.1(b)). Hot electrons typically get the majority of the excess kinetic energy during optical excitation in III-V materials. Therefore, the most important task of the hot-hole filter is its carrier-selectivity (transmitting only holes) rather than energy-selectivity. Whether or not such a structure leads to an improvement in performance compared to previously studied single barrier devices is information that would guide further efforts to evaluate the potential of hot-carrier photovoltaic devices.

If a promising hot-carrier photovoltaic system should ever be realised within a single nanowire, the next step will be to scale up the system. Parallelisation of a very large number of nanowires will be required to produce a notable power. Growth of nanowires in organised, vertical, arrays for realising conventional solar cells is already today an active field, with devices reaching conversion efficiencies up to 17,8% [133, 232]. Creating a hot-carrier solar cell from such a system would entail the challenge of focusing the optical absorption to the dedicated absorption region in the nanowire. For this purpose one could envision the use of plasmonic elements [22], or the naturally non-homogeneous absorption of light in nanowire arrays [174, 175].

Moving forward, I envision the use of the nanowire system as a platform for experimentally realise and compare the performance of various designs to hot-carrier photovoltaic devices. The flexibility and control in nanowire synthesis allows for the realisation of many types of energy filter designs, with potential added benefits from modifications in hot-carrier dynamics such as higher hot-carrier temperatures. The evaluation of the various device designs will require experimental techniques that provide spatial control of hot-carrier excitation, and that can be applied with relatively

high throughput under realistic operational conditions. The electron- and optical-beam induced current measurements applied in Papers I and II can here prove a useful experimental combination in evaluating and comparing various energy filter structures. Together they may allow for the comparison of optoelectronic performance parameters such as fill factor, power, and efficiency as functions of excitation energy, intensity, and location. Regardless of whether nanowires will be an integrated part of a future hot-carrier solar cell or not, they can play a vital role in addressing challenges that need to be tackled along the way.

References

[1] D. JC MacKay. *Sustainable Energy – Without the Hot Air*. UIT Cambridge, 2008. ISBN 978-0-9544529-3-3.

[2] WhistlingBird. Silicon solar cell, 2014. URL `https://link.aps.org/doi/10.1103/PhysRev.148.845`.

[3] A. Othonos. Probing ultrafast carrier and phonon dynamics in semiconductors. *Journal of Applied Physics*, 83(4):1789–1830, 1998.

[4] L. H. Shaffer. Wavelength-dependent (selective) processes for the utilization of solar energy. *Solar Energy*, 2(3):21–26, 1958.

[5] R. T. Ross and A. J. Nozik. Efficiency of hot-carrier solar energy converters. *Journal of Applied Physics*, 53(5):3813–3818, 1982.

[6] J. H. Davies. *The Physics of Low-dimensional Semiconductors: An Introduction*. Cambridge University Press, Cambridge, 1997. ISBN 978-0-521-48148-9.

[7] M. A. Green. Prospects for photovoltaic efficiency enhancement using low-dimensional structures. *Nanotechnology*, 11(4):401–405, 2000.

[8] D. König, Y. Yao, B. Puthen-Veettil, and S. C. Smith. Non-equilibrium dynamics, materials and structures for hot carrier solar cells: a detailed review. *Semiconductor Science and Technology*, 35(7):073002, 2020.

[9] L. Samuelson, M. T. Björk, K. Deppert, M. Larsson, B. J. Ohlsson, N. Panev, A. I. Persson, N. Sköld, C. Thelander, and L. R. Wallenberg. Semiconductor nanowires for novel one-dimensional devices. *Physica E: Low-dimensional Systems and Nanostructures*, 21(2):560–567, 2004.

[10] M. F. O'Dwyer, T. E. Humphrey, and H. Linke. Concept study for a high-efficiency nanowire based thermoelectric. *Nanotechnology*, 17(11):S338–S343, 2006.

[11] J. Fast, U. Aeberhard, S. P. Bremner, and H. Linke. Hot-carrier optoelectronic devices based on semiconductor nanowires. *Applied Physics Reviews*, 8 (2):021309, 2021.

[12] M. T. Björk, B. J. Ohlsson, T. Sass, A. I. Persson, C. Thelander, M. H. Magnusson, K. Deppert, L. R. Wallenberg, and L. Samuelson. One-dimensional heterostructures in semiconductor nanowhiskers. *Applied Physics Letters*, 80(6): 1058–1060, 2002.

[13] P. Caroff, M. E. Messing, B. M. Borg, K. A. Dick, K. Deppert, and L.-E. Wernersson. InSb heterostructure nanowires: MOVPE growth under extreme lattice mismatch. *Nanotechnology*, 20(49):495606, 2009.

[14] M. Law, J. Goldberger, and P. Yang. Semiconductor nanowires and nanotubes. *Annual Review of Materials Research*, 34(1):83–122, 2004.

[15] S. Limpert, A. M. Burke, I.-J. Chen, N. Anttu, S. Lehmann, S. Fahlvik, S. Bremner, G. Conibeer, C. Thelander, M.-E. Pistol, and H. Linke. Bipolar Photothermoelectric Effect Across Energy Filters in Single Nanowires. *Nano Letters*, 17(7):4055–4060, 2017.

[16] L. Cao, J. S. White, J.-S. Park, J. A. Schuller, B. M. Clemens, and M. L. Brongersma. Engineering light absorption in semiconductor nanowire devices. *Nature Materials*, 8(8):643–647, 2009.

[17] M. L. Brongersma, Y. Cui, and S. Fan. Light management for photovoltaics using high-index nanostructures. *Nature Materials*, 13(5):451–460, 2014.

[18] C. K. Yong, J. Wong-Leung, H. J. Joyce, J. Lloyd-Hughes, Q. Gao, H. H. Tan, C. Jagadish, M. B. Johnston, and L. M. Herz. Direct Observation of Charge-Carrier Heating at WZ–ZB InP Nanowire Heterojunctions. *Nano Letters*, 13 (9):4280–4287, 2013.

[19] D. Tedeschi, M. De Luca, H. A. Fonseka, Q. Gao, F. Mura, H. H. Tan, S. Rubini, F. Martelli, C. Jagadish, M. Capizzi, and A. Polimeni. Long-Lived Hot Carriers in III–V Nanowires. *Nano Letters*, 16(5):3085–3093, 2016.

[20] I. A. Shojaei, S. Linser, G. Jnawali, N. Wickramasuriya, H. E. Jackson, L. M. Smith, F. Kargar, A. A. Balandin, X. Yuan, H. H. Caroff, P.and Tan, and C. Jagadish. Strong Hot Carrier Effects in Single Nanowire Heterostructures. *Nano Letters*, 19(8):5062–5069, 2019.

[21] S. Limpert, A. M. Burke, I.-J. Chen, N. Anttu, S. Lehmann, S. Fahlvik, S. Bremner, C. Conibeer, G.and Thelander, M.-E. Pistol, and H. Linke. Single-nanowire, low-bandgap hot carrier solar cells with tunable open-circuit voltage. *Nanotechnology*, 28(43):434001, 2017.

[22] I.-J. Chen, S. Limpert, W. Metaferia, C. Thelander, L. Samuelson, F. Capasso, A. M. Burke, and H. Linke. Hot-Carrier Extraction in Nanowire-Nanoantenna Photovoltaic Devices. *Nano Letters*, 20(6):4064–4072, 2020.

[23] L. D. Hicks and M. S. Dresselhaus. Effect of quantum-well structures on the thermoelectric figure of merit. *Physical Review B*, 47(19):12727–12731, 1993.

[24] R. Scheibner, M. König, D. Reuter, A. D. Wieck, C. Gould, H. Buhmann, and L. W. Molenkamp. Quantum dot as thermal rectifier. *New Journal of Physics*, 10(8):083016, 2008.

[25] E. Schrödinger. Quantisierung als Eigenwertproblem. *Annalen der Physik*, 385 (13):437–490, 1926.

[26] F. Bloch. Über die Quantenmechanik der Elektronen in Kristallgittern. *Zeitschrift für Physik*, 52(7):555–600, 1929.

[27] Quantum ESPRESSO (v. 5.3.0). URL `https://www.quantum-espresso.org/`.

[28] P. Hadley. Bandstructure of indium arsenide inas, matlab script. URL `http://lampx.tugraz.at/~hadley/ss1/bands/bandstructures/InAs/inas_bands.html`.

[29] W. Shockley and H. J. Queisser. Detailed Balance Limit of Efficiency of p-n Junction Solar Cells. *Journal of Applied Physics*, 32(3):510–519, 1961.

[30] L. C. Hirst and N. J. Ekins-Daukes. Fundamental losses in solar cells. *Progress in Photovoltaics: Research and Applications*, 19(3):286–293, 2011.

[31] M. A. Green. Third generation photovoltaics: Ultra-high conversion efficiency at low cost. *Progress in Photovoltaics: Research and Applications*, 9(2):123–135, 2001.

[32] A. De Vos. Detailed balance limit of the efficiency of tandem solar cells. *Journal of Physics D: Applied Physics*, 13(5):839, 1980.

[33] M. A. Green, E. D. Dunlop, J. Hohl-Ebinger, M. Yoshita, N. Kopidakis, and X. Hao. Solar cell efficiency tables (version 56). *Progress in Photovoltaics: Research and Applications*, 28(7):629–638, 2020.

[34] J. F. Geisz, R. M. France, K. L. Schulte, M. A. Steiner, A. G. Norman, H. L. Guthrey, M. R. Young, T. Song, and T. Moriarty. Six-junction III–V solar cells with 47.1 conversion efficiency under 143 Suns concentration. *Nature Energy*, 5 (4):326–335, 2020.

[35] K A. Horowitz, T W. Remo, B Smith, and A J. Ptak. A Techno-Economic Analysis and Cost Reduction Roadmap for III-V Solar Cells. Technical Report NREL/TP-6A20-72103, National Renewable Energy Lab. (NREL), Golden, CO (United States), 2018.

[36] W. Yoon, Z. Song, C. Chen, D. Scheiman, and Y. Yan. 21.1 Efficient Space Perovskite/Si Four-Terminal Tandem Solar Cells. In *2020 47th IEEE Photovoltaic Specialists Conference (PVSC)*, pages 1552–1556, 2020.

[37] F. C. Krebs, J. Fyenbo, and M. Jørgensen. Product integration of compact roll-to-roll processed polymer solar cell modules: methods and manufacture using flexographic printing, slot-die coating and rotary screen printing. *Journal of Materials Chemistry*, 20(41):8994–9001, 2010.

[38] R. D. Schaller and V. I. Klimov. High Efficiency Carrier Multiplication in PbSe Nanocrystals: Implications for Solar Energy Conversion. *Physical Review Letters*, 92(18):186601, 2004.

[39] R. D. Schaller, M. Sykora, J. M. Pietryga, and V. I. Klimov. Seven Excitons at a Cost of One: Redefining the Limits for Conversion Efficiency of Photons into Charge Carriers. *Nano Letters*, 6(3):424–429, 2006.

[40] M. C. Beard, K. P. Knutsen, P. Yu, J. M. Luther, Q. Song, W. K. Metzger, R. J. Ellingson, and A. J. Nozik. Multiple Exciton Generation in Colloidal Silicon Nanocrystals. *Nano Letters*, 7(8):2506–2512, 2007.

[41] N. Siemons and A. Serafini. Multiple Exciton Generation in Nanostructures for Advanced Photovoltaic Cells. *Journal of Nanotechnology*, 2018:1–12, 2018.

[42] M. C. Beard, J. M. Luther, O. E. Semonin, and A. J. Nozik. Third Generation Photovoltaics based on Multiple Exciton Generation in Quantum Confined Semiconductors. *Accounts of Chemical Research*, 46(6):1252–1260, 2013.

[43] P. Würfel. Solar energy conversion with hot electrons from impact ionisation. *Solar Energy Materials and Solar Cells*, 46(1):43–52, 1997.

[44] L. Boltzmann. Über die Natur der Gasmoleküle (On the nature of gas molecules). *Wiener Berichte*, 74:553–560, 1876.

[45] W. Pauli. Über den Zusammenhang des Abschlusses der Elektronengruppen im Atom mit der Komplexstruktur der Spektren. *Zeitschrift für Physik*, 31(1): 765–783, 1925.

[46] A. Fermi, E.and Zannoni. On the Quantization of the Monoatomic Ideal Gas, 1999.

[47] L. Tesser, R. S. Whitney, and J. Splettstoesser. Thermodynamic performance of hot-carrier solar cells: A quantum transport model, 2022.

[48] D. König, K. Casalenuovo, Y. Takeda, G. Conibeer, J.F. Guillemoles, R. Patterson, L.M. Huang, and M.A. Green. Hot carrier solar cells: Principles, materials and design. *Physica E: Low-dimensional Systems and Nanostructures*, 42 (10):2862–2866, 2010.

[49] B. K. Ridley. *Quantum Processes in Semiconductors*. Oxford University Press, 2013. ISBN 978-0-19-176062-4.

[50] C. Kittel. *Introduction to solid state physics*. Wiley, Hoboken, NJ, 8th ed edition, 2005. ISBN 978-0-471-41526-8.

[51] P. G. Klemens. Anharmonic Decay of Optical Phonons. *Physical Review*, 148 (2):845–848, 1966.

[52] B. K. Ridley. The LO phonon lifetime in GaN. *Journal of Physics: Condensed Matter*, 8(37):L511–L513, 1996.

[53] B. Hejda and K. Kra´l. Hot-electron cooling and second-generation phonons in polar semiconductors. *Physical Review B*, 47(23):15554–15561, 1993.

[54] R. Baltramiejūnas and A. Žukauskas. Manifestation of Hot Phonons in the Luminescence Spectra of Highly Photoexcited AIIBVI Crystals. *physica status solidi (b)*, 149(1):337–346, 1988.

[55] V. Klimov, P. Haring Bolivar, and H. Kurz. Hot-phonon effects in femtosecond luminescence spectra of electron-hole plasmas in CdS. *Physical Review B*, 52(7): 4728–4731, 1995.

[56] J. Yang, X. Wen, H. Xia, R. Sheng, Q. Ma, J. Kim, P. Tapping, T. Harada, T. W. Kee, F. Huang, Y.-B. Cheng, M. Green, A. Ho-Baillie, S. Huang, S. Shrestha, R. Peter., and G. Conibeer. Acoustic-optical phonon up-conversion and hot-phonon bottleneck in lead-halide perovskites. *Nature Communications*, 8(1): 14120, 2017.

[57] J. Shah, A. Pinczuk, A. C. Gossard, and W. Wiegmann. Energy-Loss Rates for Hot Electrons and Holes in GaAs Quantum Wells. *Physical Review Letters*, 54 (18):2045–2048, 1985.

[58] S. M. Sze, Y. Li, and K. K Ng. *Physics of semiconductor devices*. John wiley & sons, 2006. ISBN 978-0-470-06832-8.

[59] Z. Y. Xu and C. L. Tang. Picosecond relaxation of hot carriers in highly photoexcited bulk GaAs and GaAs-AlGaAs multiple quantum wells. *Applied Physics Letters*, 44(7):692–694, 1984.

[60] J. F. Ryan, R. A. Taylor, A. J. Turberfield, Angela Maciel, J. M. Worlock, A. C. Gossard, and W. Wiegmann. Time-Resolved Photoluminescence of Two-Dimensional Hot Carriers in GaAs-AlGaAs Heterostructures. *Physical Review Letters*, 53(19):1841–1844, 1984.

[61] P. Lugli and S. M. Goodnick. Nonequilibrium longitudinal-optical phonon effects in GaAs-AlGaAs quantum wells. *Physical Review Letters*, 59(6):716–719, 1987.

[62] D. C. Edelstein, C. L. Tang, and A. J. Nozik. Picosecond relaxation of hot-carrier distributions in GaAs/GaAsP strained-layer superlattices. *Applied Physics Letters*, 51(1):48–50, 1987.

[63] K. Leo, W. W. Rühle, and K. Ploog. Hot-carrier energy-loss rates in GaAs/AlxGa1-xAs quantum wells. *Physical Review B*, 38(3):1947–1957, 1988.

[64] D. J. Westland, J. F. Ryan, M. D. Scott, J. I. Davies, and J. R. Riffat. Hot carrier energy loss rates in GaInAs/InP quantum wells. *Solid-State Electronics*, 31(3):431–434, 1988.

[65] A. J. Nozik, C. A. Parsons, D. J. Dunlavy, B. M. Keyes, and R. K. Ahrenkiel. Dependence of hot carrier luminescence on barrier thickness in GaAs/AlGaAs superlattices and multiple quantum wells. *Solid State Communications*, 75(4): 297–301, 1990.

[66] W. S. Pelouch, R. J. Ellingson, P. E. Powers, C. L. Tang, D. M. Szmyd, and A. J. Nozik. Comparison of hot-carrier relaxation in quantum wells and bulk GaAs at high carrier densities. *Physical Review B*, 45(3):1450–1453, 1992.

[67] C. A. Parsons, B. R. Thacker, D. M. Szmyd, M. W. Peterson, W. E. McMahon, and A. J. Nozik. Characterization and photocurrent spectroscopy of single quantum wells. *The Journal of Chemical Physics*, 93(11):7706–7715, 1990.

[68] Y. Rosenwaks, M. C. Hanna, D. H. Levi, D. M. Szmyd, R. K. Ahrenkiel, and A. J. Nozik. Hot-carrier cooling in GaAs: Quantum wells versus bulk. *Physical Review B*, 48(19):14675–14678, 1993.

[69] M. Sugawara, K. Mukai, and Y. M. Nakata. Self-assembled InGaAs quantum dots and quantum-dot lasers. In *Quantum Optoelectronics, paper QMC4*. Optica Publishing Group, 1999.

[70] M. A. Stroscio and M. Dutta. *Phonons in Nanostructures*. Cambridge University Press, 2001. ISBN 978-1-139-43032-6.

[71] A. Le Bris, L. Lombez, S. Laribi, G. Boissier, P. Christol, and J.-F. Guillemoles. Thermalisation rate study of GaSb-based heterostructures by continuous wave photoluminescence and their potential as hot carrier solar cell absorbers. *Energy & Environmental Science*, 5(3):6225–6232, 2012.

[72] L. C. Hirst, H. Fujii, Y. Wang, M. Sugiyama, and N. J. Ekins-Daukes. Hot Carriers in Quantum Wells for Photovoltaic Efficiency Enhancement. *IEEE Journal of Photovoltaics*, 4(1):244–252, 2014.

[73] L. C. Hirst, M. K. Yakes, C. G. Bailey, J. G. Tischler, M. P. Lumb, M. González, M. F. Führer, N. J. Ekins-Daukes, and R. J. Walters. Enhanced Hot-Carrier Effects in InAlAs/InGaAs Quantum Wells. *IEEE Journal of Photovoltaics*, 4(6): 1526–1531, 2014.

[74] T. Smyth, M. Dvorak, M. J. Y. Tayebjee, V. B. Yasarapudi, H. Xia, Y. Feng, Y. Wang, B. Puthen-Veettil, S. Huang, S. Shrestha, S. P. Bremner, T. W. Schmidt, M. Sugiyama, and G. J. Conibeer. Hot Carrier Cooling in In0.17Ga0.83As/GaAs0.80P0.20 Multiple Quantum Wells: The Effect of Barrier Thickness. *IEEE Journal of Photovoltaics*, 6(1):166–171, 2016.

[75] H. Esmaielpour, V. R. Whiteside, J. Tang, S. Vijeyaragunathan, T. D. Mishima, S. Cairns, M. B. Santos, B. Wang, and I. R. Sellers. Suppression of phonon-mediated hot carrier relaxation in type-II InAs/AlAsxSb1 – x quantum wells: a practical route to hot carrier solar cells. *Progress in Photovoltaics: Research and Applications*, 24(5):591–599, 2016.

[76] G. Conibeer, Y. Zhang, S. P. Bremner, and S. Shrestha. Towards an understanding of hot carrier cooling mechanisms in multiple quantum wells. *Japanese Journal of Applied Physics*, 56(9):091201, 2017.

[77] H. Esmaielpour, V. R. Whiteside, H. P. Piyathilaka, S. Vijeyaragunathan, B. Wang, E. Adcock-Smith, K. P. Roberts, T. D. Mishima, M. B. Santos, Alan D. Bristow, and I. R. Sellers. Enhanced hot electron lifetimes in quantum wells with inhibited phonon coupling. *Scientific Reports*, 8(1):12473, 2018.

[78] Y. Zhang, M. J. Y. Tayebjee, S. Smyth, M. Dvořák, X. Wen, H. Xia, M. Heilmann, Y. Liao, Z. Zhang, T. Williamson, J. Williams, S. Bremner, S. Shrestha, S. Huang, T. W. Schmidt, and G. J. Conibeer. Extended hot carrier lifetimes observed in bulk In0.265±0.02Ga0.735N under high-density photoexcitation. *Applied Physics Letters*, 108(13):131904, 2016.

[79] Y. Yao and D. König. Comparison of bulk material candidates for hot carrier absorber. *Solar Energy Materials and Solar Cells*, 140:422–427, 2015.

[80] P. Aliberti, Y. Feng, Y. Takeda, S. K. Shrestha, M. A. Green, and G. Conibeer. Investigation of theoretical efficiency limit of hot carriers solar cells with a bulk indium nitride absorber. *Journal of Applied Physics*, 108(9):094507, 2010.

[81] Y. Yao, D. König, and M. Green. Investigation of boron antimonide as hot carrier absorber material. *Solar Energy Materials and Solar Cells*, 111:123–126, 2013.

[82] L. Lindsay, D. A. Broido, and T. L. Reinecke. Ab initio thermal transport in compound semiconductors. *Physical Review B*, 87(16):165201, 2013.

[83] R. Clady, M. J. Y. Tayebjee, P. Aliberti, D. König, N. J. Ekins-Daukes, G. J. Conibeer, T. W. Schmidt, and M. A. Green. Interplay between the hot phonon effect and intervalley scattering on the cooling rate of hot carriers in GaAs and InP. *Progress in Photovoltaics: Research and Applications*, 20(1):82–92, 2012.

[84] W. Dai, W. Liu, J. Yang, A. Xu, C.and Alabastri, C. Liu, P. Nordlander, Z. Guan, and H. Xu. Giant photothermoelectric effect in silicon nanoribbon photodetectors. *Light: Science & Applications*, 9(1):120, 2020.

[85] A. P. Kirk and M. V. Fischetti. Fundamental limitations of hot-carrier solar cells. *Physical Review B*, 86(16):165206, 2012.

[86] J. Shah. *Hot Carriers in Semiconductor Nanostructures: Physics and Applications*. Elsevier, 2012. ISBN 978-0-08-092570-7.

[87] B. G. Streetman and S. Banerhee. *Solid state electronic devices*, volume 10. Pearson/Prentice Hall Upper Saddle River, 2006.

[88] L.-X. Wang, Z.-Q. Zhou, T.-N. Zhang, X. Chen, and M. Lu. High Fill Factors of Si Solar Cells Achieved by Using an Inverse Connection Between MOS and PN Junctions. *Nanoscale Research Letters*, 11, 2016.

[89] G. Benenti, G. Casati, K. Saito, and R. S. Whitney. Fundamental aspects of steady-state conversion of heat to work at the nanoscale. *Physics Reports*, 694: 1–124, 2017.

[90] M. Josefsson. *Quantum-Dot Heat Engines*. Phd thesis, Lund University, 2020.

[91] F. J. DiSalvo. Thermoelectric Cooling and Power Generation. *Science*, 285 (5428):703–706, 1999.

[92] J. P. Heremans, M. S. Dresselhaus, L. E. Bell, and D. T. Morelli. When thermoelectrics reached the nanoscale. *Nature Nanotechnology*, 8(7):471–473, 2013.

[93] L. D. Hicks and M. S. Dresselhaus. Thermoelectric figure of merit of a one-dimensional conductor. *Physical Review B*, 47(24):16631–16634, 1993.

[94] J. P. Heremans, C. M. Thrush, D. T. Morelli, and M.-C. Wu. Thermoelectric Power of Bismuth Nanocomposites. *Physical Review Letters*, 88(21):216801, 2002.

[95] S. Kolenda, P. Machon, D. Beckmann, and W. Belzig. Nonlinear thermoelectric effects in high-field superconductor-ferromagnet tunnel junctions. *Beilstein Journal of Nanotechnology*, 7(1):1579–1585, 2016.

[96] R. López and D. Sánchez. Nonlinear heat transport in mesoscopic conductors: Rectification, Peltier effect, and Wiedemann-Franz law. *Physical Review B*, 88 (4):045129, 2013.

[97] M. Leijnse, M. R. Wegewijs, and K. Flensberg. Nonlinear thermoelectric properties of molecular junctions with vibrational coupling. *Physical Review B*, 82 (4):045412, 2010.

[98] R. Wang, H. Liao, C.-Y. Song, G.-H. Tang, and N.-X. Yang. Linear and nonlinear thermoelectric transport in a quantum spin Hall insulators coupled with a nanomagnet. *Scientific Reports*, 12(1):12048, 2022.

[99] M. Büttiker. Four-Terminal Phase-Coherent Conductance. *Physical Review Letters*, 57(14):1761–1764, 1986.

[100] F. L. Curzon and B. Ahlborn. Efficiency of a Carnot engine at maximum power output. *American Journal of Physics*, 43(1):22–24, 1975.

[101] J. A. R. Dimmock, S. Day, M. Kauer, K. Smith, and J. Heffernan. Demonstration of a hot-carrier photovoltaic cell. *Progress in Photovoltaics: Research and Applications*, 22(2):151–160, 2014.

[102] J. A. R. Dimmock, M. Kauer, K. Smith, H. Liu, P. N. Stavrinou, and N. J. Ekins-Daukes. Optoelectronic characterization of carrier extraction in a hot carrier photovoltaic cell structure. *Journal of Optics*, 18(7):074003, 2016.

[103] G. J. Conibeer, C. W. Jiang, D. König, S. Shrestha, T. Walsh, and M. A. Green. Selective energy contacts for hot carrier solar cells. *Thin Solid Films*, 516(20): 6968–6973, 2008.

[104] G. Conibeer, M. Green, R. Corkish, Y. Cho, E.-C. Cho, C.-W. Jiang, T. Fangsuwannarak, E. Pink, Y. Huang, T. Puzzer, T. Trupke, B. Richards, A. Shalav, and K.-l. Lin. Silicon nanostructures for third generation photovoltaic solar cells. *Thin Solid Films*, 511-512:654–662, 2006.

[105] S. K. Shrestha, P. Aliberti, and G. J. Conibeer. Energy selective contacts for hot carrier solar cells. *Solar Energy Materials and Solar Cells*, 94(9):1546–1550, 2010.

[106] D. König, D. Hiller, M. Zacharias, S. Michard, and C. Flynn. Static hot carrier populations as a function of optical excitation energy detected through energy selective contacts by optically assisted IV. *Progress in Photovoltaics: Research and Applications*, 22(10):1070–1079, 2014.

[107] C.-W. Jiang, M. A. Green, E.-C. Cho, and G. Conibeer. Resonant tunneling through defects in an insulator: Modeling and solar cell applications. *Journal of Applied Physics*, 96(9):5006–5012, 2004.

[108] I. Konovalov, V. Emelianov, and R. Linke. Hot carrier solar cell with semi infinite energy filtering. *Solar Energy*, 111:1–9, 2015.

[109] L. C. Hirst, R. J. Walters, M. F. Führer, and N. J. Ekins-Daukes. Experimental demonstration of hot-carrier photo-current in an InGaAs quantum well solar cell. *Applied Physics Letters*, 104(23):231115, 2014.

[110] Y. Harada, N. Iwata, S. Asahi, and T. Kita. Hot-carrier generation and extraction in InAs/GaAs quantum dot superlattice solar cells. *Semiconductor Science and Technology*, 34(9):094003, 2019.

[111] D.-T. Nguyen, L. Lombez, F. Gibelli, S. Boyer-Richard, A. L. Corre, O. Durand, and J.-F. Guillemoles. Quantitative experimental assessment of hot carrier-enhanced solar cells at room temperature. *Nature Energy*, 3(3):236, 2018.

[112] W. A. Tisdale, K. J. Williams, B. A. Timp, D. J. Norris, E. S. Aydil, and X.-Y. Zhu. Hot-Electron Transfer from Semiconductor Nanocrystals. *Science*, 328 (5985):1543–1547, 2010.

[113] I. Konovalov and V. Emelianov. Hot carrier solar cell as thermoelectric device. *Energy Science & Engineering*, 5(3):113–122, 2017.

[114] G. D. Mahan and J. O. Sofo. The best thermoelectric. *Proceedings of the National Academy of Sciences*, 93(15):7436–7439, 1996.

[115] T. E. Humphrey, R. Newbury, R. P. Taylor, and H. Linke. Reversible Quantum Brownian Heat Engines for Electrons. *Physical Review Letters*, 89(11):116801, 2002.

[116] P. Murphy, S. Mukerjee, and J. Moore. Optimal thermoelectric figure of merit of a molecular junction. *Physical Review B*, 78(16):161406, 2008.

[117] A. Svilans. *Thermoelectric experiments on nanowire-based quantum dots*. Phd thesis, Lund University, 2018.

[118] T. E. Humphrey and H. Linke. Reversible Thermoelectric Nanomaterials. *Physical Review Letters*, 94(9):096601, 2005.

[119] S Limpert, S Bremner, and H Linke. Reversible electron–hole separation in a hot carrier solar cell. *New Journal of Physics*, 17(9):095004, 2015.

[120] M. Josefsson, A. Svilans, A. M. Burke, E. A. Hoffmann, S. Fahlvik, C. Thelander, M. Leijnse, and H. Linke. A quantum-dot heat engine operating close to the thermodynamic efficiency limits. *Nature Nanotechnology*, 13(10):920–924, 2018.

[121] G Conibeer, N. J. Ekins-Daukes, J.-F. Guillemoles, D. König, E.-C. Cho, C.-W. Jiang, S. Shrestha, and M. Green. Progress on hot carrier cells. *Solar Energy Materials and Solar Cells*, 93(6):713–719, 2009.

[122] N. Nakpathomkun, H. Q. Xu, and H. Linke. Thermoelectric efficiency at maximum power in low-dimensional systems. *Physical Review B*, 82(23):235428, 2010.

[123] R. S. Whitney. Most Efficient Quantum Thermoelectric at Finite Power Output. *Physical Review Letters*, 112(13):130601, 2014.

[124] A. Julian, Z. Jehl, N. Miyashita, Y. Okada, and J. F. Guillemoles. Insights on energy selective contacts for thermal energy harvesting using double resonant tunneling contacts and numerical modeling. *Superlattices and Microstructures*, 100:749–756, 2016.

[125] S. Hershfield, K. A. Muttalib, and B. J. Nartowt. Nonlinear thermoelectric transport: A class of nanodevices for high efficiency and large power output. *Physical Review B*, 88(8):085426, 2013.

[126] P.-H. Chang, M. Saeed Bahramy, N. Nagaosa, and B. K. Nikolić. Giant Thermoelectric Effect in Graphene-Based Topological Insulators with Heavy Adatoms and Nanopores. *Nano Letters*, 14(7):3779–3784, 2014.

[127] R. S. Whitney. Finding the quantum thermoelectric with maximal efficiency and minimal entropy production at given power output. *Physical Review B*, 91 (11):115425, 2015.

[128] H. Karbaschi, J. Lovén, K. Courteaut, A. Wacker, and M. Leijnse. Nonlinear thermoelectric efficiency of superlattice-structured nanowires. *Physical Review B*, 94(11):115414, 2016.

[129] C. H. Schiegg, M. Dzierzawa, and U. Eckern. Implementation of transmission functions for an optimized three-terminal quantum dot heat engine. *Journal of Physics: Condensed Matter*, 29(8):085303, 2017.

[130] P. Priyadarshi, A. Sharma, S. Mukherjee, and B. Muralidharan. Superlattice design for optimal thermoelectric generator performance. *Journal of Physics D: Applied Physics*, 51(18):185301, 2018.

[131] A. Le Bris and J.-F. Guillemoles. Hot carrier solar cells: Achievable efficiency accounting for heat losses in the absorber and through contacts. *Applied Physics Letters*, 97(11):113506, 2010.

[132] G. Min. New formulation of the theory of thermoelectric generators operating under constant heat flux. *Energy & Environmental Science*, 15(1):356–367, 2022.

[133] G. Otnes and M. T. Borgström. Towards high efficiency nanowire solar cells. *Nano Today*, 12:31–45, 2017.

[134] Y. Huang, X. Duan, Y. Cui, L. J. Lauhon, K.-H. Kim, and C. M. Lieber. Logic Gates and Computation from Assembled Nanowire Building Blocks. *Science*, 294(5545):1313–1317, 2001.

[135] Y. Duan, Y. Zhu, K. Li, Q. Wang, P. Wang, H. Yu, Z. Yan, and X. Zhao. Cu2O–Au nanowire field-effect phototransistor for hot carrier transfer enhanced photodetection. *Nanotechnology*, 30(24):245202, 2019.

[136] V. Mourik, K. Zuo, S. M. Frolov, S. R. Plissard, E. P. A. M. Bakkers, and L. P. Kouwenhoven. Signatures of Majorana Fermions in Hybrid Superconductor-Semiconductor Nanowire Devices. *Science*, 336(6084):1003–1007, 2012.

[137] S. M. Albrecht, A. P. Higginbotham, M. Madsen, F. Kuemmeth, T. S. Jespersen, J. Nygård, P. Krogstrup, and C. M. Marcus. Exponential protection of zero modes in Majorana islands. *Nature*, 531(7593):206–209, 2016.

[138] A.I. Boukai, Y. Bunimovich, J. Tahir-Kheli, J.-K. Yu, W.A. Goddard III, and J.R. Heath. Silicon nanowires as efficient thermoelectric materials. *Nature*, 451 (7175):168–171, 2008.

[139] R. S. Wagner and W. C. Ellis. Vapor-liquid-solid mechanism of single crystal growth. *Applied Physics Letters*, 4(5):89–90, 1964.

[140] T. D. Steiner. *Semiconductor Nanostructures for Optoelectronic Applications*. Artech House, 2004. ISBN 978-1-58053-752-0.

[141] L. Hrachowina. *Growth and Characterization of Tandem-Junction Photovoltaic Nanowires*. Phd thesis, Lund University, 2022.

[142] W. T. Tsang. Chemical beam epitaxy of InP and GaAs. *Applied Physics Letters*, 45(11):1234–1236, 1984.

[143] W. T. Tsang. Chemical beam epitaxy of Ga0.47In0.53As/InP quantum wells and heterostructure devices. *Journal of Crystal Growth*, 81(1):261–269, 1987.

[144] C. Thelander, K. A. Dick, M. T. Borgström, L. E. Fröberg, P. Caroff, H. A. Nilsson, and L. Samuelson. The electrical and structural properties of n-type InAs nanowires grown from metal–organic precursors. *Nanotechnology*, 21(20): 205703, 2010.

[145] L. Wittenbecher, E. Viñas Boström, J. Vogelsang, S. Lehman, K. A. Dick, C. Verdozzi, D. Zigmantas, and A. Mikkelsen. Unraveling the Ultrafast Hot Electron Dynamics in Semiconductor Nanowires. *ACS Nano*, 15(1):1133–1144, 2021.

[146] J. Zou and A. Balandin. Phonon heat conduction in a semiconductor nanowire. *Journal of Applied Physics*, 89(5):2932–2938, 2001.

[147] D. Li, Y. Wu, P. Kim, L. Shi, P. Yang, and A. Majumdar. Thermal conductivity of individual silicon nanowires. *Applied Physics Letters*, 83(14):2934–2936, 2003.

[148] P. Mushonga, M. O. Onani, A. M. Madiehe, and M. Meyer. Indium Phosphide-Based Semiconductor Nanocrystals and Their Applications. *Journal of Nanomaterials*, 2012:1–11, 2012.

[149] S. Ramanathan, S. Patibandla, S. Bandyopadhyay, J. Anderson, and J. D. Edwards. Fluorescence spectroscopy of electrochemically self-assembled ZnSe and Mn:ZnSe nanowires. *Nanotechnology*, 19(19):195601, 2008.

[150] H.-J. Byun, J. C. Lee, and H. Yang. Solvothermal synthesis of InP quantum dots and their enhanced luminescent efficiency by post-synthetic treatments. *Journal of Colloid and Interface Science*, 355(1):35–41, 2011.

[151] T. Puangmali, M. Califano, and P. Harrison. Monotonic Evolution of the Optical Properties in the Transition from Three- to Quasi-Two-Dimensional Quantum Confinement in InAs Nanorods. *The Journal of Physical Chemistry C*, 114(15):6901–6908, 2010.

[152] K. W. Kim, M. A. Stroscio, A. Bhatt, R. Mickevicius, and V. V. Mitin. Electron-optical-phonon scattering rates in a rectangular semiconductor quantum wire. *Journal of Applied Physics*, 70(1):319–327, 1991.

[153] V. B. Campos and S. Das Sarma. Hot-electron relaxation in semiconductor quantum wires: Bulk-LO-phonon emission. *Physical Review B*, 45(7):3898–3901, 1992.

[154] S. Das Sarma, V. B. Campos, M. A. Stroscio, and K. W. Kim. Confined phonon modes and hot-electron energy relaxation in semiconductor microstructures. *Semiconductor Science and Technology*, 7(3B):B60, 1992.

[155] J. P. Leburton. Size effects on polar optical phonon scattering of 1-D and 2-D electron gas in synthetic semiconductors. *Journal of Applied Physics*, 56(10): 2850–2855, 1984.

[156] B. K. Ridley. Hot electrons in low-dimensional structures. *Reports on Progress in Physics*, 54(2):169–256, 1991.

[157] X. Lü. Lattice thermal conductivity of Si nanowires: Effect of modified phonon density of states. *Journal of Applied Physics*, 104(5):054314, 2008.

[158] N. Mingo, L. Yang, D. Li, and A. Majumdar. Predicting the Thermal Conductivity of Si and Ge Nanowires. *Nano Letters*, 3(12):1713–1716, 2003.

[159] N. Mingo. Calculation of Si nanowire thermal conductivity using complete phonon dispersion relations. *Physical Review B*, 68(11):113308, 2003.

[160] X. Lü, J. H. Chu, and W. Z. Shen. Modification of the lattice thermal conductivity in semiconductor rectangular nanowires. *Journal of Applied Physics*, 93(2):1219–1229, 2002.

[161] A. I. Hochbaum, R. Chen, R. D. Delgado, W. Liang, E. C. Garnett, M. Najarian, A. Majumdar, and P. Yang. Enhanced thermoelectric performance of rough silicon nanowires. *Nature*, 451(7175):163–167, 2008.

[162] R. Chen, A. I. Hochbaum, P. Murphy, J. Moore, P. Yang, and A. Majumdar. Thermal Conductance of Thin Silicon Nanowires. *Physical Review Letters*, 101 (10):105501, 2008.

[163] M. Y. Swinkels, M. R. van Delft, D. S. Oliveira, A. Cavalli, I. Zardo, R. W. van der Heijden, and E. P. A. M. Bakkers. Diameter dependence of the thermal conductivity of InAs nanowires. *Nanotechnology*, 26(38):385401, 2015.

[164] F. Zhou, A. L. Moore, J. Bolinsson, A. Persson, L. Fröberg, M. T. Pettes, H. Kong, L. Rabenberg, P. Caroff, D. A. Stewart, N. Mingo, K. A. Dick, L. Samuelson, H. Linke, and L. Shi. Thermal conductivity of indium arsenide nanowires with wurtzite and zinc blende phases. *Physical Review B*, 83(20): 205416, 2011.

[165] P. Ren, X. Zhu, J. Han, J. Xu, L. Ma, H. Li, X. Zhuang, H. Zhou, Q. Zhang, M. Xia, and A. Pan. Synthesis and Diameter-dependent Thermal Conductivity of InAs Nanowires. *Nano-Micro Letters*, 6(4):301–306, 2014.

[166] C. T. Bui, R. Xie, M. Zheng, Q.n Zhang, C. H. Sow, B. Li, and J. T. L. Thong. Diameter-Dependent Thermal Transport in Individual ZnO Nanowires and its Correlation with Surface Coating and Defects. *Small*, 8(5):738–745, 2012.

[167] M. C. Wingert, Z. C. Y. Chen, E. Dechaumphai, J. Moon, J.-H. Kim, J. Xiang, and R. Chen. Thermal Conductivity of Ge and Ge–Si Core–Shell Nanowires in the Phonon Confinement Regime. *Nano Letters*, 11(12):5507–5513, 2011.

[168] D. Li, Y. Wu, R. Fan, P. Yang, and A. Majumdar. Thermal conductivity of Si/SiGe superlattice nanowires. *Applied Physics Letters*, 83(15):3186–3188, 2003.

[169] A. Jurgilaitis, H. Enquist, B. P. Andreasson, A. I. H. Persson, B. M. Borg, P. Caroff, K. A. Dick, M. Harb, H. Linke, R. Nüske, L.-E. Wernersson, and J. Larsson. Time-Resolved X-ray Diffraction Investigation of the Modified Phonon Dispersion in InSb Nanowires. *Nano Letters*, 14(2):541–546, 2014.

[170] R. P. Wang, G. Xu, and P. Jin. Size dependence of electron-phonon coupling in ZnO nanowires. *Physical Review B*, 69(11):113303, 2004.

[171] Q. Zhang, J. Zhang, M. I. B. Utama, B. Peng, M. de la Mata, J. Arbiol, and Q. Xiong. Exciton-phonon coupling in individual ZnTe nanorods studied by resonant Raman spectroscopy. *Physical Review B*, 85(8):085418, 2012.

[172] P. Krogstrup, H. I. Jørgensen, M. Heiss, O. Demichel, J. V. Holm, M. Aagesen, J. Nygard, and A. Fontcuberta i Morral. Single-nanowire solar cells beyond the Shockley–Queisser limit. *Nature Photonics*, 7(4):306–310, 2013.

[173] N. Anttu. Absorption of light in a single vertical nanowire and a nanowire array. *Nanotechnology*, 30(10):104004, 2019.

[174] J. Kupec, R. L. Stoop, and B. Witzigmann. Light absorption and emission in nanowire array solar cells. *Optics Express*, 18(26):27589–27605, 2010.

[175] J. Wallentin, N. Anttu, D. Asoli, M. Huffman, I. Aberg, M. H. Magnusson, G. Siefer, P. Fuss-Kailuweit, F. Dimroth, B. Witzigmann, H. Q. Xu,

L. Samuelson, K. Deppert, and M. T. Borgstrom. InP Nanowire Array Solar Cells Achieving 13.8 Efficiency by Exceeding the Ray Optics Limit. *Science*, 339(6123):1057–1060, 2013.

[176] P. R. Narangari, S. K. Karuturi, Y. Wu, J. Wong-Leung, K. Vora, M. Lysevych, Y. Wan, H. H. Tan, C. Jagadish, and S. Mokkapati. Ultrathin Ta2O5 electron-selective contacts for high efficiency InP solar cells. *Nanoscale*, 11(15):7497–7505, 2019.

[177] J. Wagner, A.-L. Alvarez, J. Schmitz, J. D. Ralston, and P. Koidl. Surface Fermi level pinning in epitaxial InSb studied by electric-field-induced Raman scattering. *Applied Physics Letters*, 63(3):349–351, 1993.

[178] P. D. C. King, T. D. Veal, M. J. Lowe, and C. F. McConville. Surface electronic properties of clean and S-terminated InSb(001) and (111)B. *Journal of Applied Physics*, 104(8):083709, 2008.

[179] S. Nadj-Perge, V. S. Pribiag, J. W. G. van den Berg, K. Zuo, S. R. Plissard, E. P. A. M. Bakkers, S. M. Frolov, and L. P. Kouwenhoven. Spectroscopy of Spin-Orbit Quantum Bits in Indium Antimonide Nanowires. *Physical Review Letters*, 108(16):166801, 2012.

[180] V. S. Pribiag, S. Nadj-Perge, S. M. Frolov, J. W. G. van den Berg, I. van Weperen, S. R. Plissard, E. P. a. M. Bakkers, and L. P. Kouwenhoven. Electrical control of single hole spins in nanowire quantum dots. *Nature Nanotechnology*, 8(3):170–174, 2013.

[181] Ioffe Physico-Technical Institute. Electronic archive: New Semiconductor Materials. Characteristics and Properties. URL `http://www.ioffe.ru/SVA/`.

[182] S. Bhargava, H.-R. Blank, V. Narayanamurti, and H. Kroemer. Fermi-level pinning position at the Au–InAs interface determined using ballistic electron emission microscopy. *Applied Physics Letters*, 70(6):759–761, 1997.

[183] R. Graham, C. Miller, E. Oh, and D. Yu. Electric Field Dependent Photocurrent Decay Length in Single Lead Sulfide Nanowire Field Effect Transistors. *Nano Letters*, 11(2):717–722, 2011.

[184] C. Hajlaoui, L. Pedesseau, F. Raouafi, F. Ben Cheikh Larbi, J. Even, and J.-M. Jancu. First-principles calculations of band offsets and polarization effects at InAs/InP interfaces. *Journal of Physics D: Applied Physics*, 48(35):355105, 2015.

[185] C. Thelander, M. T. Björk, M. W. Larsson, A. E. Hansen, L. R. Wallenberg, and L. Samuelson. Electron transport in InAs nanowires and heterostructure nanowire devices. *Solid State Communications*, 131(9):573–579, 2004.

[186] D. B. Suyatin, C. Thelander, M. T. Björk, I. Maximov, and L. Samuelson. Sulfur passivation for ohmic contact formation to InAs nanowires. *Nanotechnology*, 18(10):105307, 2007.

[187] J. G. Gluschke, S. Fahlvik Svensson, C. Thelander, and H. Linke. Fully tunable, non-invasive thermal biasing of gated nanostructures suitable for low-temperature studies. *Nanotechnology*, 25(38):385704, 2014.

[188] V. Giannini, A. I. Fernández-Domínguez, S. C. Heck, and S. A. Maier. Plasmonic Nanoantennas: Fundamentals and Their Use in Controlling the Radiative Properties of Nanoemitters. *Chemical Reviews*, 111(6):3888–3912, 2011.

[189] L. Prechtel, M. Padilla, N. Erhard, H. Karl, G. Abstreiter, A. Fontcuberta I Morral, and A. W. Holleitner. Time-Resolved Photoinduced Thermoelectric and Transport Currents in GaAs Nanowires. *Nano Letters*, 12(5):2337–2341, 2012.

[190] Y. Ahn, J. Dunning, and J. Park. Scanning Photocurrent Imaging and Electronic Band Studies in Silicon Nanowire Field Effect Transistors. *Nano Letters*, 5(7):1367–1370, 2005.

[191] B. Varghese, R. Tamang, E. S. Tok, S. G. Mhaisalkar, and C. H. Sow. Photothermoelectric Effects in Localized Photocurrent of Individual VO2 Nanowires. *The Journal of Physical Chemistry C*, 114(35):15149–15156, 2010.

[192] B. L. Henke, J. Liesegang, and S. D. Smith. Soft-x-ray-induced secondary-electron emission from semiconductors and insulators: Models and measurements. *Physical Review B*, 19(6):3004–3021, 1979.

[193] G. Otnes, E. Barrigón, C. Sundvall, M. Svensson, K. E.and Heurlin, G. Siefer, L. Samuelson, I. Åberg, and M. T. Borgström. Understanding InP Nanowire Array Solar Cell Performance by Nanoprobe-Enabled Single Nanowire Measurements. *Nano Letters*, 18(5):3038–3046, 2018.

[194] Q. Gao, Z. Li, L. Li, K. Vora, Z. Li, A. Alabadla, F. Wang, Y. Guo, K. Peng, Y. C. Wenas, S.a Mokkapati, F. Karouta, H. H. Tan, C. Jagadish, and L. Fu. Axial p-n junction design and characterization for InP nanowire array solar cells. *Progress in Photovoltaics: Research and Applications*, 27(3):237–244, 2019.

[195] E. Barrigón, Y. Zhang, L. Hrachowina, G. Otnes, and M. T. Borgström. Unravelling processing issues of nanowire-based solar cell arrays by use of electron beam induced current measurements. *Nano Energy*, 71:104575, 2020.

[196] J. Wallentin, P. Wickert, M. Ek, A. Gustafsson, L. Reine Wallenberg, M. H. Magnusson, L. Samuelson, K. Deppert, and M. T. Borgström. Degenerate p-doping of InP nanowires for large area tunnel diodes. *Applied Physics Letters*, 99(25):253105, 2011.

[197] J. E. Allen, E. R. Hemesath, D. E. Perea, J. L. Lensch-Falk, Z. Y. Li, F. Yin, M. H. Gass, P. Wang, A. L. Bleloch, R. E. Palmer, and L. J. Lauhon. High-resolution detection of Au catalyst atoms in Si nanowires. *Nature Nanotechnology*, 3(3):168–173, 2008.

[198] C. Y. Chen, A. Shik, A. Pitanti, A. Tredicucci, D. Ercolani, L. Sorba, F. Beltram, and H. E. Ruda. Electron beam induced current in InSb-InAs nanowire type-III heterostructures. *Applied Physics Letters*, 101(6):063116, 2012.

[199] R. Shimizu and D. Ze-Jun. Monte Carlo modelling of electron-solid interactions. *Reports on Progress in Physics*, 55(4):487–531, 1992.

[200] J. Cazaux. From the physics of secondary electron emission to image contrasts in scanning electron microscopy†. *Journal of Electron Microscopy*, 61(5):261–284, 2012.

[201] H. J. Leamy. Charge collection scanning electron microscopy. *Journal of Applied Physics*, 53(6):R51–R80, 1982.

[202] P. Hovington, D. Drouin, and R. Gauvin. CASINO: A new monte carlo code in C language for electron beam interaction —part I: Description of the program. *Scanning*, 19(1):1–14, 1997.

[203] J. Park, Y. H. Ahn, and C. Ruiz-Vargas. Imaging of Photocurrent Generation and Collection in Single-Layer Graphene. *Nano Letters*, 9(5):1742–1746, 2009.

[204] X. Xu, N. M. Gabor, J. S. Alden, A. M. van der Zande, and P. L. McEuen. Photo-Thermoelectric Effect at a Graphene Interface Junction. *Nano Letters*, 10(2):562–566, 2010.

[205] M. C. Lemme, F. H. L. Koppens, A. L. Falk, M. S. Rudner, H. Park, L. S. Levitov, and C. M. Marcus. Gate-Activated Photoresponse in a Graphene p–n Junction. *Nano Letters*, 11(10):4134–4137, 2011.

[206] N. M. Gabor, J. C. W. Song, Q. Ma, N. L. Nair, T. Taychatanapat, K. Watanabe, T. Taniguchi, L. S. Levitov, and P. Jarillo-Herrero. Hot Carrier–Assisted Intrinsic Photoresponse in Graphene. *Science*, 334(6056):648–652, 2011.

[207] D. Sun, G. Aivazian, A. M. Jones, J. S. Ross, W. Yao, D. Cobden, and X. Xu. Ultrafast hot-carrier-dominated photocurrent in graphene. *Nature Nanotechnology*, 7(2):114–118, 2012.

[208] C. Liu, N. M. Dissanayake, S. Lee, K. Lee, and Z. Zhong. Evidence for Extraction of Photoexcited Hot Carriers from Graphene. *ACS Nano*, 6(8):7172–7176, 2012.

[209] P. K. Herring, A. L. Hsu, N. M. Gabor, Y. C. Shin, J. Kong, T. Palacios, and P. Jarillo-Herrero. Photoresponse of an Electrically Tunable Ambipolar Graphene Infrared Thermocouple. *Nano Letters*, 14(2):901–907, 2014.

[210] T. J. Echtermeyer, P. S. Nene, M. Trushin, R. V. Gorbachev, A. L. Eiden, S. Milana, Z. Sun, J. Schliemann, E. Lidorikis, K. S. Novoselov, and A. C. Ferrari. Photothermoelectric and Photoelectric Contributions to Light Detection in Metal–Graphene–Metal Photodetectors. *Nano Letters*, 14(7):3733–3742, 2014.

[211] K. J. Tielrooij, M. Massicotte, L. Piatkowski, A. Woessner, Q. Ma, P. Jarillo-Herrero, N. F. van Hulst, and F. H. L. Koppens. Hot-carrier photocurrent effects at graphene–metal interfaces. *Journal of Physics: Condensed Matter*, 27 (16):164207, 2015.

[212] M. Buscema, M. Barkelid, V. Zwiller, H. S. J. van der Zant, G. A. Steele, and A. Castellanos-Gomez. Large and Tunable Photothermoelectric Effect in Single-Layer MoS2. *Nano Letters*, 13(2):358–363, 2013.

[213] Y. Zhang, H. Li, L. Wang, H. Wang, X. Xie, S.-L. Zhang, R. Liu, and Z.-J.n Qiu. Photothermoelectric and photovoltaic effects both present in MoS2. *Scientific Reports*, 5(1):7938, 2015.

[214] J. Groenendijk, M. Buscema, G. A. Steele, S. Michaelis de Vasconcellos, R. Bratschitsch, H. S. J. van der Zant, and A. Castellanos-Gomez. Photovoltaic and Photothermoelectric Effect in a Double-Gated WSe2 Device. *Nano Letters*, 14(10):5846–5852, 2014.

[215] N. Erhard, P. Seifert, L. Prechtel, S. Hertenberger, H. Karl, G. Abstreiter, G. Koblmüller, and A. W. Holleitner. Ultrafast photocurrents and THz generation in single InAs-nanowires. *Annalen der Physik*, 525(1-2):180–188, 2013.

[216] Y. Yang, X. Peng, H.-S. Kim, T. Kim, S. Jeon, H. Kyu Kang, W. Choi, J. Song, Y.-J. Doh, and D. Yu. Hot Carrier Trapping Induced Negative Photoconductance in InAs Nanowires toward Novel Nonvolatile Memory. *Nano Letters*, 15 (9):5875–5882, 2015.

[217] F. Léonard, E. Song, Q. Li, B. Swartzentruber, J. A. Martinez, and G. T. Wang. Simultaneous Thermoelectric and Optoelectronic Characterization of Individual Nanowires. *Nano Letters*, 15(12):8129–8135, 2015.

[218] N. Wiener. *Extrapolation, interpolation, and smoothing of stationary time series: with engineering applications*, volume 113. Cambridge, MA: MIT press, 21 edition, 1949.

[219] Y.-P. Liu. *Surfaces and interfaces of low dimensional III-V semiconductor devices*. Phd thesis, Lund University, 2022.

[220] D. M.-T. Kuo and Y.-C. Chang. Thermoelectric and thermal rectification properties of quantum dot junctions. *Physical Review B*, 81(20):205321, 2010.

[221] G. T. Craven, D. He, and A. Nitzan. Electron-Transfer-Induced Thermal and Thermoelectric Rectification. *Physical Review Letters*, 121(24):247704, 2018.

[222] K. Prakash, P. Thakur, S. Bansal, S. Garg, P. Jain, K. Sharma, N. Gupta, S. R. Kasjoo, S. Kumar, and A. K. Singh. Thermoelectric rectification in a graphene-based triangular ballistic rectifier (G-TBR). *Journal of Computational Electronics*, 20(6):2308–2316, 2021.

[223] J. A. Nelson. *The Physics Of Solar Cells*. World Scientific Publishing Company, 2003. ISBN 978-1-84816-823-7.

[224] R. H. Fowler and L. Nordheim. Electron emission in intense electric fields. *Proceedings of the Royal Society of London. Series A, Containing Papers of a Mathematical and Physical Character*, 119.781:173–181, 1928.

[225] P. F.-J. Mensch. *Thermoelectric Characterization of InAs Nanowires*. PhD thesis, ETH Zürich, 2015.

[226] D. L. Rode. Electron Transport in InSb, InAs, and InP. *Physical Review B*, 3 (10):3287–3299, 1971.

[227] J. Fast, Y-P. Liu, Y. Chen, L. Samuelson, A. M. Burke, H. Linke, and A. Mikkelsen. Optical-Beam-Induced Current in InAs/InP Nanowires for Hot-Carrier Photovoltaics. *ACS Applied Energy Materials*, 5(6):7728–7734, 2022.

[228] J. Fast, E. Barrigon, M. Kumar, Y. Chen, L. Samuelson, M. Borgström, A. Gustafsson, S. Limpert, A. M. Burke, and H. Linke. Hot-carrier separation in heterostructure nanowires observed by electron-beam induced current. *Nanotechnology*, 31(39):394004, 2020.

[229] M. T. Björk, C. Thelander, A. E. Hansen, L. E. Jensen, M. W. Larsson, L. R. Wallenberg, and L. Samuelson. Few-Electron Quantum Dots in Nanowires. *Nano Letters*, 4(9):1621–1625, 2004.

[230] M. S. Gudiksen, L. J. Lauhon, J. Wang, D. C. Smith, and C. M. Lieber. Growth of nanowire superlattice structures for nanoscale photonics and electronics. *Nature*, 415(6872):617–620, 2002.

[231] W.i. Park, G.-C. Yi, M.y. Kim, and S.j. Pennycook. Quantum Confinement Observed in ZnO/ZnMgO Nanorod Heterostructures. *Advanced Materials*, 15 (6):526–529, 2003.

[232] D. van Dam, N. J. J. van Hoof, Y. Cui, P. J. van Veldhoven, E. P. Bakkers, J. Gómez Rivas, and J. E. M. Haverkort. High-Efficiency Nanowire Solar Cells with Omnidirectionally Enhanced Absorption Due to Self-Aligned Indium–Tin–Oxide Mie Scatterers. *ACS Nano*, 10(12):11414–11419, 2016.

Scientific publications

DON'T PANIC

Printed by Media-Tryck, Lund 2023 NORDIC SWAN ECOLABEL 3041 0903

Division of Solid State Physics
Department of Physics
Faculty of Engineering

ISBN 978-91-8039-500-7